

**THE DYNAMIC MECHANICAL
CHARACTERIZATION OF A BIO-INSPIRED
SANDWICH STRUCTURE**

**A Thesis Submitted to
the Graduate School of Engineering and Sciences of
İzmir Institute of Technology
in Partial Fulfillment of the Requirements for the Degree of**

MASTER OF SCIENCE

in Mechanical Engineering

**by
Ayda RAMYAR**

December 2019

İZMİR

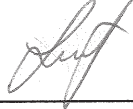
We approve the thesis of Ayda RAMYAR

Examining Committee Members:



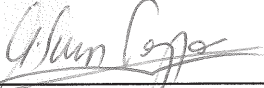
Prof. Dr. Alper TAŞDEMİRÇİ

Department of Mechanical Engineering, İzmir Institute of Technology



Assoc. Prof. Dr. Hatice Seçil ARTEM

Department of Mechanical Engineering, İzmir Institute of Technology



Prof. Dr. Meltem Evren TOYGAR

Department of Mechanical Engineering, Dokuz Eylül University

20 December 2019



Prof. Dr. Alper TAŞDEMİRÇİ

Supervisor, Department of
Mechanical Engineering,
İzmir Institute of Technology



Prof. Dr. Mustafa GÜDEN

Co-Supervisor, Department of
Mechanical Engineering,
İzmir Institute of Technology



Prof. Dr. Sedat AKKURT

Head of the Department of
Mechanical Engineering



Prof. Dr. Mehtap EANES

Dean of the Graduate School of
Engineering and Sciences

ACKNOWLEDGMENTS

I would like to express my gratefulness to my supervisor Prof. Dr. Alper TAŞDEMİRÇİ for his inspiration, guidance, advice and encouragement during my thesis study. In the light of his expertise and support, I have been able to complete my studies. I also would like to thank my co-advisor Prof. Dr. Mustafa GÜDEN for sharing his theoretical knowledge during the study, which contributed a lot to the improvement of this study.

I am also grateful to my family who deserve special mention for their support and encouragement.

Special thanks to Mesut BAYHAN and Semih Berk SEVEN for their invaluable assistance during the experimental work and Dynamic Testing and Modeling Laboratory Team for their support.

Furthermore, I would like to thank my respected colleagues at Bosch Thermoteknik Research & Development Department for their support and understanding.

Last but not least, I would like to thank my dear boyfriend Uğur CEYLAN for his encouragement.

ABSTRACT

THE DYNAMIC MECHANICAL CHARACTERIZATION OF A BIO-INSPIRED SANDWICH STRUCTURE

In this study, the sandwich structure consisting of novel-3D-printed-polymeric base core was examined in terms of crashworthiness. The designed core structure for energy absorption purpose is inspired by the geometry of the human fingerprint. The fingerprint geometry is a spiral-shaped, asymmetrical and complex structure; therefore, the manufacturing of the geometry is difficult by conventional manufacturing methods. Fused Deposition Modeling (FDM) which is one of the additive manufacturing (AM) methods was used for fingerprint core preparation by layer by layer production technique with low-density material. After the material characterization of 3D printed thermoplastic specimens, optimum geometric parameters of fingerprint were determined via experimental and numerical studies by changing the height and thickness. The fingerprint performed better crushing performance compared to other conventional geometries. Quasi-static and dynamic crushing experiments were conducted, and the results were verified with models by non-linear finite element code LS-DYNA. The results showed that the energy absorption capacity and peak crushing force of fingerprint geometry increases with strain rate increment. However, the deformation behavior of the structure under dynamic loads changes and the material becomes more brittle. This is caused by the change in deformation mechanism due to AM and material itself. It was found that the 3-D printed core structure is suitable to be employed at low-to-medium strain rates due to its multi-stage deformation behavior. It was observed that the bio-inspired sandwich structure consisting of 4 fingerprint-core can absorb 10% more impact energy than fourfold individual 3-D printed core geometry, which indicates the promising potential of the novel sandwich structure for crashworthiness applications.

ÖZET

BİYO BENZETİM TABANLI SANDVIÇ YAPININ DİNAMİK MEKANİK KARAKTERİZASYONU

Bu çalışmada, 3 boyutlu (3D) yazıcıda üretilmiş özgün çekirdek yapısı içeren sandviç yapının enerji emme niteliği incelenmiştir. Sandviç yapılarda çekirdek, enerji emilimini üstlendiği için yenilikçi çekirdek tasarımı oldukça önem taşımaktadır. Çalışmada enerji emme performansını iyileştirme amacıyla kullanılan çekirdek yapısı insan parmak izinden esinlenerek tasarlanmıştır. İnsan parmak izi geometrik olarak spiral, asimetrik ve kompleks bir yapıya sahip olduğu için bu geometrinin üretimi geleneksel üretim metotları ile zor ve zaman alıcıdır. Eklemeli üretim metotları geniş üretim olanakları sunmaktadır. Bu çalışmada eklemeli üretim metotlarından biri olan FDM, parmak izi çekirdek yapısının katmanlı üretim tekniği ile üretilmesinde kullanılmıştır. 3D ile üretilmiş termoplastik numunelerinin malzeme karakterizasyonu yapıldıktan sonra parmak izinin optimum geometrik parametreleri, yükseklik ve kalınlık değerleri değiştirilerek deneysel ve nümerik çalışmalarla belirlenmiştir. Ayrıca parmak izi geometrisinin, geleneksel yapılara göre daha iyi enerji emme performansı gösterdiği saptanmıştır. Statik ve dinamik ezilme deneylerinden elde edilen sonuçlar, LS-DYNA sonlu elemanlar analiz programında modellenerek sonuçlar doğrulanmıştır. Bu sonuçlar, parmak izi geometrisinin enerji emme kapasitesinin ve ilk pik kuvvet değerinin deformasyon hızının artmasıyla birlikte arttığını göstermiştir. Buna karşılık, yapının dinamik yükler altındaki deformasyon davranışının değiştiği ve daha kırılğan hale geldiği gözlemlenmiştir. Bunun nedeninin seçilen üretim yöntemi ve bu yöntemde kullanılan malzeme olduğu gözlemlenmiştir. Deformasyon hızına bağlı değişen deformasyon karakteristiği incelendiğinde yapının düşük-orta deformasyon hızlarında daha iyi çalışabileceği saptanmıştır. Dörtlü parmak izi geometrisinden oluşan çekirdek yapı ihtiva eden sandviç yapının, parmak izinin tekli ezilme davranışının 4 katından %10 daha fazla enerji emme özelliğine sahip olduğu gözlemlenmiştir.

TABLE OF CONTENTS

LIST OF FIGURES	viii
LIST OF TABLES	xiv
CHAPTER 1 INTRODUCTION.....	1
1.1. Background and Energy Absorption Fundamentals	1
1.2. Literature Review	4
1.2.1. Biomimicry	4
1.2.2. Sandwich Structures.....	12
1.2.3. Additive Manufacturing.....	18
1.2.3.1. Fused Deposition Modeling (FDM)	20
1.3. Thesis Objective	22
CHAPTER 2 MATERIALS AND METHODS	23
2.1. Design and Production of Specimens by FDM	23
2.1.1. Determining Process Variables.....	23
2.1.2. Manufactured Parts by FDM.....	26
2.2. Material Characterization and Crushing Tests.....	30
2.2.1. Quasi-Static Testing.....	30
2.2.1.1. Tension Test.....	31
2.2.1.2. Compression Test	32
2.2.2. Dynamic Testing.....	33
2.2.2.1. Drop-Weight Impact Test	34
2.2.2.2. SHTB and SHPB Tests.....	35
CHAPTER 3 MODELLING	41
3.1. Material Model Development.....	42
3.2. Modeling of Experimental Tests.....	46

CHAPTER 4 RESULTS AND DISCUSSION	52
4.1. 3D Printed ABS Material Characterization Results	52
4.2. Fingerprint Core Crushing Behavior Results.....	63
4.3. Fingerprint Core Numerical Model Validations.....	84
4.4. Sandwich Structure Crushing Behavior Results.....	91
CHAPTER 5 CONCLUSION	96
REFERENCES	99

LIST OF FIGURES

<u>Figure</u>	<u>Page</u>
Figure 1.1. Schematic diagram of design cycle of an energy absorbing structure. (Source: Baroutaji et al., 2017)	4
Figure 1.2. Schematic representation of biomimetic basics.	5
Figure 1.3. The strength a) and stiffness, b) values of natural materials with respect to density (Source: Wegst and Ashby, 2004).....	6
Figure 1.4. a) Beak structure of Tukan birds (Source: Seki et al., 2010), b) Skeletal structure of marine sponge and the buildings inspired by this structure (Source: Meyers et al., 2008), c) Stenocara insect species living in the dessert and producing their own water (Source: Parker and Lawrence, 2001), d) Burdock burrs showing adhesion ability to different surfaces, e) Gecko’s foot and toe tips (Source: Sitti and Fearing, 2003), f) Structure of abalone shellfish (Source: W. Yang et al., 2011), g) Humpack-whale fin and bio-inspired wind turbine blade (Source: https://whalepowercorp.wordpress.com).	8
Figure 1.5. a) Fingerprint types (Source: https://www.touchngoid.com/8-common-fingerprint-patterns/), b) Fingerprint formation at the 11th week of the fetus in the womb (Source: Champod et al., 2004), c) Fluorescence image of aluminum foil with eccrine fingerprint after dipping into N-1- Cys-coated CdTe QDs solution for 5 seconds (Source: Li et al., 2017)....	10
Figure 1.6. a) Empty nested-4 tubes with FE model (Source: Usta and Türkmen, 2019), b) Multi stage nested two-square tube (Source: Tran et al., 2019), c) Multi-tubular 6101 Al alloy structures under quasi-static compression (Source: Nia and Chahardoli, 2016a), d) Deformation of multi-tubular structures under quasi-static compression with FE model (Source: Nia and Chahardoli, 2016b).....	11
Figure 1.7. Types of fingerprints similar to nested structures: a) Whorl, b) Loop. (Source: http://www.forensicsciencesimplified.org/prints/principles)	11
Figure 1.8. Conventional sandwich structures (Source: Bitzer, 1997)	13

<u>Figure</u>	<u>Page</u>
Figure 1.9. Schematic of bio-inspired sandwich structure consisting of honeycomb core and CFRP panels, test setup and FE Model for impact test and test results in terms of load and SEA (Source: Yinghan Wu et al., 2017)	14
Figure 1.10. Elytra beetle, its microstructure and bending test results. (Source: Yuanqi Wu et al., 2017).....	14
Figure 1.11. Bio-inspired sandwich structures; a) Tortoise shell and insect wing sandwich structure (Source: Yinghan Wu et al., 2017), b) Sinusoidal array core geometry sandwich structure inspired by Mantis shrimp (Source: X. Yang et al., 2017), c) Conceptual design sandwich structure consisting of Kagome core geometry (Source: Ullah et al., 2014), d) Pomelo, coconut shell and macadamia nut structure (Source: Seidel et al., 2010).	15
Figure 1.12. a) Head structure of woodpecker, b) Designed sandwich structure consisting of bio-inspired honeycomb core (Source: Sabah et al., 2017)..	17
Figure 1.13. Balanus and Bio-inspired core (Source: Tasdemirci et al., 2018).....	17
Figure 1.14. 3-D objects manufacturing process via AM Technology. (Source: https://aaq.auburn.edu/node/9907/).....	18
Figure 1.15. Fused Deposition Modeling (FDM) working principle (Source: a) https://aaq.auburn.edu/ , b) Kanu, 2016).....	20
Figure 2.1. (a) Built orientations (Source: Chacón et al., 2017), (b) Isometric view of selected building orientation (flat) of ABS tension specimens.	24
Figure 2.2. (a) Infill densities low, high, and solid respectively, (b) uPrint SE default raster angle, (c) Printing illustration of uPrint SE with outer shell and infill density (Source: Kerekes et al., 2019).....	25
Figure 2.3. Basic steps of FDM process for specimen preparation.	26
Figure 2.4. Type I, quasi-static tensile test specimen for ABS characterization, according to ASTM D638-02a (Dimensions are in mm).....	27
Figure 2.5. Custom tensile specimen used in both quasi-static and dynamic tensile tests for ABS characterization (Dimensions are in mm).....	27
Figure 2.6. Type IV, quasi-static tensile test specimen for ABS characterization, according to ASTM D638-02a (Dimensions are in mm).....	28

<u>Figure</u>	<u>Page</u>
Figure 2.7. 3-D printed test specimen used in both quasi-static and dynamic compression tests.	29
Figure 2.8. 3-D printed fingerprint cores with different height and thickness values. ..	29
Figure 2.9. 3-D printed fingerprint core and conventional geometries; cylinder, honeycomb and square, respectively.	30
Figure 2.10. Quasi- static tension test set-up with different load carrying capacity chins.	32
Figure 2.11. Quasi-static compression test set-up.	33
Figure 2.12. Drop-weight test set up with DAS.	35
Figure 2.13. SHTB test set-up for dynamic tensile characterization.	36
Figure 2.14. Schematic representation of SHPB (Source: Bayhan, 2018).	37
Figure 2.15. Schematic representation of SHTB (Source: Young, 2015).	37
Figure 3.1. True Yield stress vs true plastic strain curves for implementing rate sensitivity (Source: LSTC, 2016).....	44
Figure 3.2. Material model input curves for yield stress scaling factors with respect to varying strain rates.	45
Figure 3.3. Schematic representation of FEA steps.	46
Figure 3.4. Sketch, 3D solid drawing and discretized model of fingerprint core.	47
Figure 3.5. Fingerprint crushing test set-up and its model.	48
Figure 3.6. Fingerprint cores with different thickness (1.0 and 1.5 mm) values.	49
Figure 3.7. Fingerprint cores with different height (20, 30 and 40 mm) values.	49
Figure 3.8. Fingerprint and conventional geometries (cylinder, honeycomb and square) having the same areal density, same height and mass.	50
Figure 3.9. The sandwich structure consisted of 4 fingerprint as a core and Al face sheets.	51
Figure 4.1. Quasi-static tensile stress-strain curves of 3-D printed Type I tensile specimens.	53
Figure 4.2. Quasi-static tensile stress-strain curves of 3-D printed Custom tensile specimens.	54
Figure 4.3. Custom Type specimens after quasi-static tensile test.	55
Figure 4.4. Type IV specimens after quasi-static tensile test.	55

<u>Figure</u>	<u>Page</u>
Figure 4.5. Quasi-static tensile stress-strain curves of 3-D printed Type IV tensile specimens.	56
Figure 4.6. Comparison of quasi-static tensile stress-strain curves for different shape tension specimens.	57
Figure 4.7. Dynamic tension stress-strain curve of 3-D printed ABS.	57
Figure 4.8. Deformation history of specimen under dynamic tension loads (SHTB). ..	58
Figure 4.9. Comparison of quasi-static and dynamic tension stress-strain curves of 3-D printed tensile specimens.	59
Figure 4.10. Quasi-static compression stress-strain curves of 3D printed specimen.	60
Figure 4.11. Comparison of quasi-static compression stress-strain curves of 3-D printed compression specimens.	61
Figure 4.12. Dynamic compression stress-strain curve of 3-D printed ABS.	62
Figure 4.13. Deformation history of specimen under dynamic compressive loads (SHPB).	62
Figure 4.14. Comparison of quasi-static and dynamic compression stress-strain curves of 3-D printed compression specimens.	63
Figure 4.15. Quasi-static experimental force vs. displacement curves of fingerprint for varying height and thickness values.	64
Figure 4.16. Comparison of quasi-static crushing behavior of fingerprint cores for varying height and thickness values.	65
Figure 4.17. Quasi-static experimental force & SAE vs. displacement plots of fingerprint cores for varying height and thickness values.	67
Figure 4.18. Quasi-static experimental SAE & Peak force vs. displacement values of fingerprint cores for varying height and thickness values.	68
Figure 4.19. Dynamic numerical force & SAE vs. % displacement curves of fingerprint cores for varying height and thickness values.	69
Figure 4.20. Comparison of dynamic numerical crushing behavior of fingerprint cores for varying height and thickness values.	69
Figure 4.21. Quasi-static experimental force vs. displacement curves of fingerprint and conventional geometries (case:1, for different diameters).	71

<u>Figure</u>	<u>Page</u>
Figure 4.22. Comparison of quasi-static crushing behavior of fingerprint and conventional geometries (cylinder, honeycomb and square) (for different diameters).	72
Figure 4.23. Fully-crushed views of conventional structures (square, cylinder and honeycomb) after the quasi-static compression test.	72
Figure 4.24. Quasi-static experimental SAE & Peak force vs. displacement values of fingerprint and conventional geometries (case:1,for different diameters).....	73
Figure 4.25. Dynamic numerical force & SAE vs. displacement curves of fingerprint and conventional geometries (case:2, for same areal density).....	74
Figure 4.26. Comparison of dynamic numerical crushing behavior of fingerprint and conventional geometries (cylinder, honeycomb and square) (for same areal density).	75
Figure 4.27. Quasi-static experimental force vs. displacement curves of fingerprint core for 1.2, 12 and 120 mm/min crosshead speeds.	76
Figure 4.28. Quasi-static experimental SAE & Peak force vs. displacement values of fingerprint core for 1.2, 12 and 120 mm/min crosshead speeds.	77
Figure 4.29. a) Deformation history of fingerprint core at 1.2 mm/min cross head speed, b) Final shape of fully crushed fingerprint geometry.	78
Figure 4.30. a) Dynamic experimental force & SAE vs. displacement curves of fingerprint core at 2 m/s impact velocity, b) Final shape of fully crushed fingerprint core.....	79
Figure 4.31. a) Dynamic experimental force & SAE vs. displacement curves of fingerprint core at 3.5 m/s impact velocity, b) Final shape of fully crushed fingerprint core.	80
Figure 4.32. Force vs. displacement curves of fingerprint core under quasi-static and dynamic axial loads.....	81
Figure 4.33. SAE vs. displacement curves of fingerprint at quasi-static and dynamic loads a) at 3mm, b) at densification region.....	82
Figure 4.34. Quasi-static and dynamic experimental SAE & Peak force vs. displacement values of fingerprint core.	83

<u>Figure</u>	<u>Page</u>
Figure 4.35. Comparison of force vs. displacement curves of experimental and numerical quasi-static compression of fingerprint core at 120 mm/min crosshead speed.....	84
Figure 4.36. Comparison of the deformation histories of experimental and numerical quasi-static compression of fingerprint core.....	85
Figure 4.37. Comparison of force vs. displacement curves of experimental and numerical dynamic compression of fingerprint core at 2 m/s impact velocity.....	86
Figure 4.38. Comparison of the deformation histories of experimental and numerical dynamic compression of fingerprint core at 2 m/s impact velocity.....	87
Figure 4.39. Comparison of a) force vs. displacement, b) SAE vs. displacement curves of experimental and numerical dynamic compression of fingerprint core at 3.5 m/s impact velocity.	88
Figure 4.40. Comparison of the deformation histories of experimental and numerical dynamic compression of fingerprint core at 3.5 m/s impact velocity.....	89
Figure 4.41. Investigation of inertia effect with rate sensitive experiment and rate insensitive numerical model.....	90
Figure 4.42. Comparison of a) force vs. displacement, b) SAE vs. displacement curves of numerical bio-inspired sandwich structure and experiment for individual core multiplied by 4 at 2 m/s impact velocity.....	92
Figure 4.43. Comparison of a) force vs. displacement, b) SAE vs. displacement curves of numerical bio-inspired sandwich structure and experiment for individual core multiplied by 4 at 3.5 m/s impact velocity.....	93
Figure 4.44. Deformation history of sandwich structure consisting of aluminum faces and 4 fingerprint core.....	94
Figure 4.45. a) The deformed view of numerically crushed sandwich structure consisting of 4 fingerprint b) The deformed view of experimentally crushed fingerprint core.	95

LIST OF TABLES

<u>Table</u>	<u>Page</u>
Table 1.1. Classification of AM technologies (Source: Kanu, 2016).....	19
Table 1.2. Mechanical properties of ABS specimens (Kanu, 2016).....	21
Table 2.1. Material properties of the Vascomax C350 bars.	38
Table 2.2. Material properties of the 316L Stainless steel bars.	38
Table 3.1. MAT24 material model parameters for fingerprint core.	45

CHAPTER 1

INTRODUCTION

The energy absorbers must have maximum impact energy absorption capacity with minimum density. For this purpose, different lightweight materials (polymers, composites, and sandwich structures), and conventional or bio-inspired geometric patterns (honeycomb, square, cylindrical, corrugated, origami) are used to obtain the further improvement in energy absorption capability at relatively low weights. Geometric design and material selection play an important role in these structures. With the development of new manufacturing techniques, it is possible to produce complex geometries without compromising weight optimization. Thanks to the additive manufacturing (AM), inspiring structures existing in the nature can be manufactured by mimicking.

1.1. Background and Energy Absorption Fundamentals

Designing an energy absorbing structure, dispersing kinetic energy at a fixed controlled rate should be the main purpose (Su and Reid, 1995). Considering design and analysis, when we compare energy absorbing structures with conventional structures, the former withstands great impact loads, and their deformation and failure comprise large geometrical transformations, strain hardening and strain rate effects. On the other hand, conventional structures are subjected to minor elastic deformation under the loads. The strength and stiffness of these structures are required to be sufficiently high since these parameters determine the design and material selection. Unlike the energy absorbing structures, failure of conventional structures is due to fatigue, corrosion etc.

The energy absorption capacity can be measured by ‘crashworthiness’ characteristic, which indicates the response quality of a structure under impact loads (Johnson, 1990; Johnson and Mamalis, 1978). Thanks to their quality of dissipating kinetic energy during dynamic loading, energy-absorbing structures and materials have

been of great importance since 1970s, particularly in automobile and military industries (Johnson and Reid, 1977). Commonly, ductile materials are preferred as an energy absorber, such as low carbon steel and aluminum alloys, as well as lightweight structures (sandwich structures, non-metallic reinforced plastics and foams).

High energy-absorption and consequently crashworthiness are requisites for safety value for vehicles, auxiliary protective devices, as well as auxiliary equipment for human body in sports and games because they are exposed to high plastic deformations under the impacts (Baroutaji et al., 2017; Ali et al., 2006; Heimbs, 2012). Besides these, protective packaging has become an important issue in preserving/storing and distributing goods. To prevent damage, different materials have been used for cushioning, such as shredded waste paper, cellular wadding and rubberized hair (Lu and Yu, 2003). Although these traditional materials are still used, polymer and composite based sandwich structures substituted for traditional ones, as they can be customized for proper protection (Haldar et al., 2016; Yoo et al., 2010; Smardzewski, 2019; Bodaghi et al., 2020).

Mainly, investigation of energy-absorbing structure behavior is initiated by quasi-static experimental testing. Quasi-static properties contain dominant (common) geometrical effects, which are also observed under dynamic loads. At low speed impacts, direct proportion between yield stress and strain rate can be shown by Cowper-Symonds equation. That is, if strain rate increases, the yield stress of the material also increases proportionally which is common in most of the unreinforced polymers and some metals (Hopmann et al., 2016; Lu and Yu, 2003). Briefly, engineering plasticity and crashworthiness are used to investigate the performance of energy-absorbing structures. This differentiates the study of energy absorbers from traditional ones in purpose and method.

The design of energy absorber targets dissipating kinetic energy in a controlled level. Hence, some basic principles can be applied in all design cases. These principles are as follows: “Irreversible energy conversion, limited and constant reactive force, long stroke, stable deformation mode, high specific energy absorption capacity and being light weight ” (Lu and Yu, 2003).

Input kinetic energy should be converted into inelastic energy by plastic deformation or dissipating operations. If it is converted into elastic strain energy, this energy is discharged after reaching a maximum elastic deformation, which is hazardous to the person or structure/system. Plastic dissipation, viscous deformation, energy

dissipation by friction or failure are different types of irreversible energy taking place during deformation stage. For ductile materials, absorbing energy by means of plastic deformation is the most efficient technique (Ali et al., 2006; Lu and Yu, 2003).

The energy absorber's reaction force should be below the threshold maximum, and during deformation stage, it should remain constant, while maximum deceleration due to peak force should be below the threshold to prevent damage and delay (Ali et al., 2006).

“For an energy-absorbing structure, the work done is equal to the magnitude of the force multiplied by the displacement during the period of acting force. Therefore, if absorbing more energy is the concern so the stroke should be sufficiently long” (Lu and Yu, 2003). Accordingly, the more absorption of input-energy, the longer the displacement is supposed to be. Force, F , occurs due to change in momentum, mv and it propagates through impacting regions and spreads wide over time, t . Since it is inversely proportional to t ($F=mv/t$), where longer time means long stroke resulting in decreased peak force, and vice versa, a useful law for decreasing impact damage.

To sustain the reliability of the structure or system, structure's deformation mode and energy absorption potential need to be kept steady and recurring, because applied external dynamic loads show unpredictability in magnitude and direction.

“The energy-absorbing component must be light, with a high specific energy absorption capacity (total amount of energy absorption per unit weight), which is vital for the personal safety devices”. The production of these should be easy and economical, because when their form changes, they are disposed and replaced (Lu and Yu, 2003; Heimbs, 2012).

Generally, the biggest challenge during the design progress of an energy absorbing structure is determining the optimal configuration of a thin-walled structure which perfectly meets the crashworthiness needs. The design and analysis steps should start with geometry selection and be followed by consideration of loading conditions and potential deformation modes. Then, mean crush force (MCF) and peak crush force (PCF) should be determined. Finally, this cycle must be repeated several times to validate (Baroutaji et al., 2017). The design cycle is shown in Figure 1.1.

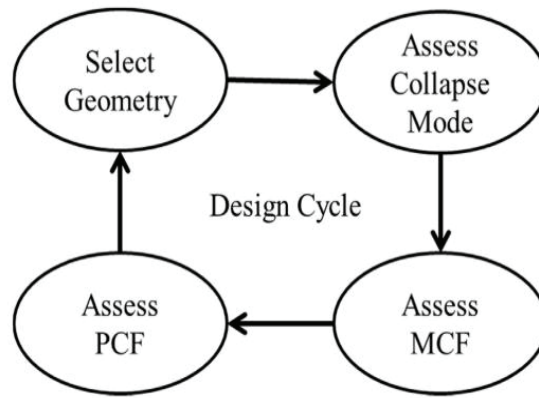


Figure 1.1. Schematic diagram of design cycle of an energy absorbing structure. (Source: Baroutaji et al., 2017)

1.2. Literature Review

1.2.1. Biomimicry

Biological based systems offer innovative solutions in engineering applications due to their versatile advantages. At the same time, putting the reasons underlying this superior mechanical performance of the structure of natural materials existing in nature is a research field that has attracted considerable attention in recent years and has achieved extremely successful results. This research field is called “Biomimicry”, the science inspired by models and systems in nature. In other words, “Bio-inspiration is the study of emulating and mimicking nature, used by designers to solve human problems” (Aziz and El sherif, 2016). In 1960’s, the term ‘Biomimicry’ was used in literature and became common in 1980’s (Fayemi et al., 2014; Aziz and El sherif, 2016). It argues that nature is the most impressive source of innovation. Our perception of nature should be that the nature is a “model, measure and mentor” and the fundamental purpose of this perspective should be obtaining sustainability (Benyus, 1997). Bio-inspired approach is based on detecting a unique behavior in an organism or system and implementing it into designs that meeting the needs at macro or micro-scales. The schematic of biomimetic approach is shown in Figure 1.2.

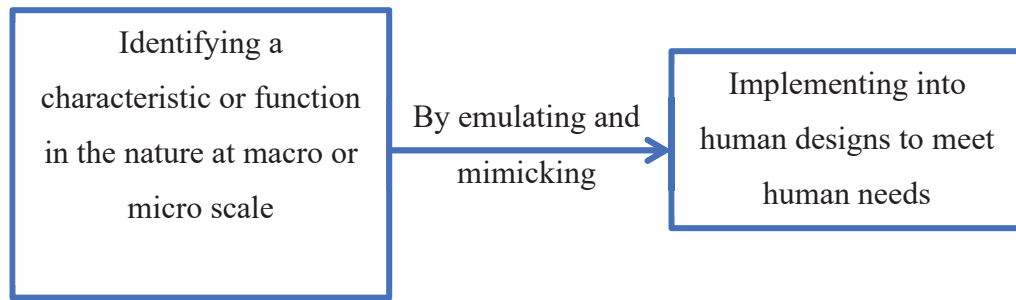
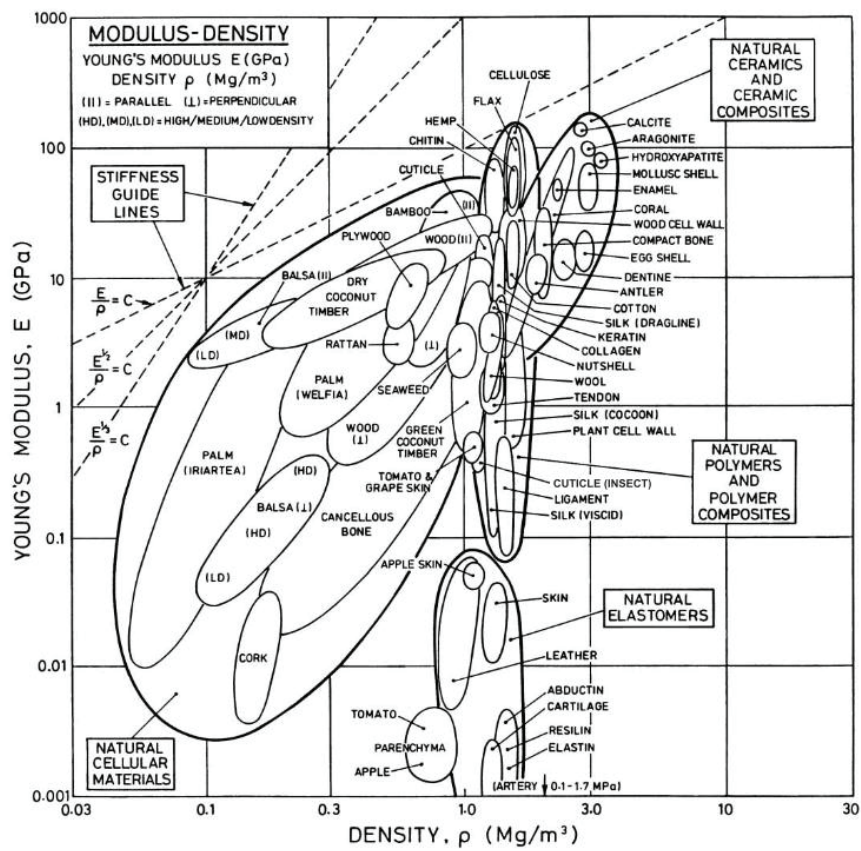
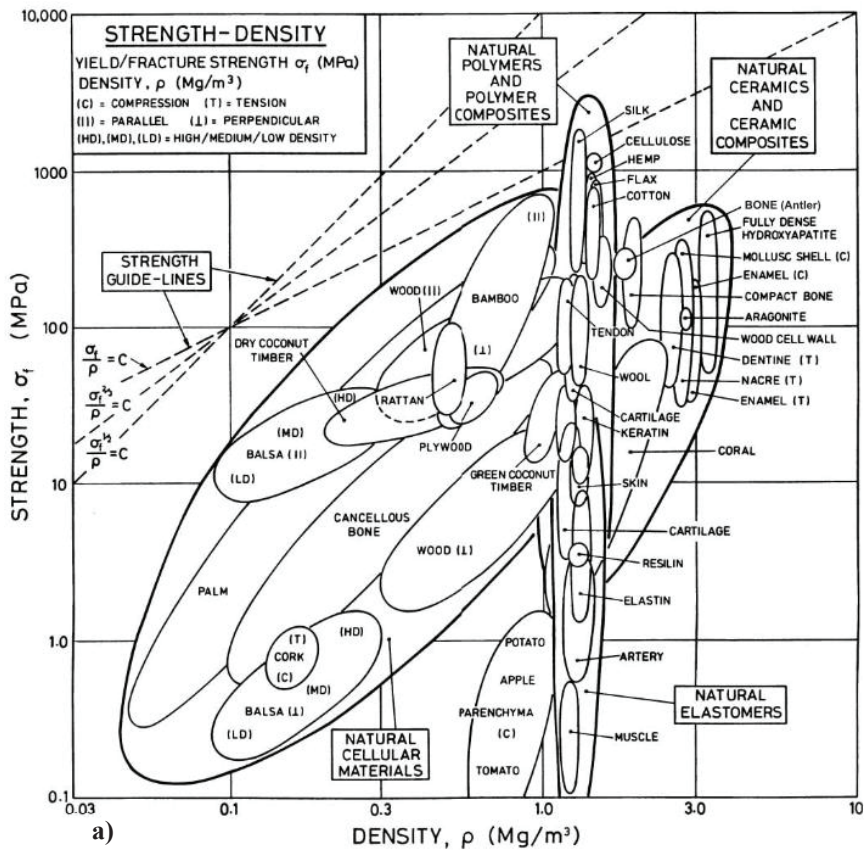


Figure 1.2. Schematic representation of biomimetic basics.

In 2004, Wegst and Ashby were published a review article that covers natural materials and they studied on mechanical efficiency in nature. In the light of their research they claimed that nature-inspired structures are more favorable than nature-inspired materials or natural existing materials in engineering approach (Wegst and Ashby, 2004). They examined natural materials by separating them into four classes. These classes can be listed as follows: i) ceramic and ceramic composites, ii) polymers and polymer composites, iii) elastomers, iv) porous materials. Figure 1.3 represents the strength and modulus of elasticity values of different kinds of materials having different densities, respectively. Wegst and Ashby emphasized that success in bio-inspired work is achieved using the structural properties of these materials. Briefly, structural design is the key to success in bio-inspired designs (Wegst and Ashby, 2004). Meyers et al. summarized the studies which are inspired by the biological materials and systems, focusing on the mechanical properties of these materials (Meyers et al., 2008).

The bio-inspired applications are technological and scientific engineering studies which are based on taking the special properties of living creatures existing in nature and converting these unique properties into design field. The examples related with these bio-inspired studies are as follows:

Seki et al. examined beak structures of bird species called Tukan and Boynuzgaga (Figure 1.4(a)). It was found that the beak is a sandwich composite material that consists of a keratin outer shell and a fiber meshed of bony closed cell foam material. The mechanical tests revealed the bio-inspired beak structure has a superior stiffness and bending resistance in spite of its light-weight due to its synergistic effect between foam and keratin shell. The foam provides internal support to the keratin shell while the shell is deforming, hence its buckling load and bending resistance under flexure loading (Seki et al., 2010; Seki et al., 2006; Seki et al., 2005).



b) Figure 1.3. The strength a) and stiffness, b) values of natural materials with respect to density (Source: Wegst and Ashby, 2004).

Aizenberg et al. examined the skeletal structure of the deep-sea sponge called *Euplectella* and found that it provides superior structural stability at low-cost. Due to the superior properties of this structure, today it is used as a supportive system for skyscraper skeletons (Figure 1.4(b))(Aizenberg et al., 2005).

Parker and Lawrence examined insect species called *Stenocara* and reported that they could draw water from the moisture of the air in desert conditions with the help of their shell. It was shown that the beetle can transfer water from its back to its mouth in order to drink water thanks to its special bumpy, channeled and wax-coated (waxy) surface structure (Figure 1.4(c)). This unique structure is used for controlled collection of moisture from air for drinking or agriculture including areas where there is water shortage with the help of its biomimetic potential (Parker and Lawrence, 2001).

Velcro, one of the biggest commercial applications of bio-inspired structures, found a place in industrial applications with the help of the electrical engineer George de Mestral in 1948. He recognized the gripping feature of burdock burrs (very small hooked tip structure) that are sticky stuffs and he implemented this feature in the field of textile. Today, this application is known as “hook-and-loop and fasteners” (Figure 1.4(d)).

As shown in (Figure 1.4(e)), it was observed that with the help of five hundred thousand micro-sized hairs (setae) on the toe tips of a lizard called Gecko, it is able to hold on to any surface that it touches. According to the measurements, the acting force from the hairs on Gecko’s toe tips in order to attach to the surfaces (adhesion force) was found to be ten times greater than the force applied by the other creatures for attaching onto the surfaces (Autumn et al., 2000). By observing the setae of Gecko’s toe tips, Autumn et al. found that the Van der Waals forces existed between the structure and contact surfaces at atomic level indicate notable adhesive effects (Autumn et al., 2002). Because this creature exhibits an extraordinary gripping behavior onto the surfaces, the synthetic production of the setae was aimed as dry adhesives for wall-climbing and surgical robots and microelectronics by using nanotechnologies (Ge et al., 2007; Sitti and Fearing, 2003; Geim et al., 2003).

Sarikaya et al. examined the shellfish called Abalone and discovered that this creature exhibits superior fracture strength (180 MPa) and fracture toughness ($7\pm 3 \text{ Mpa}\cdot\text{m}^{1/2}$) over many high-tech ceramic materials. They suggested that the Abalone shell could be mimicked in the design of synthetic laminates such as ceramic-metal and ceramic-polymer composites (Sarikaya et al., 1990). In addition, the mechanical response

of Abalone and *Saxidomus purpuratus* shell structures (Figure 1.4(f)) were determined by static and dynamic tests. They reported that these shell structures exhibited strain rate sensitivity and directional dependence of compressive strength like composites (Menig et al. 2000; W. Yang et al., 2011).

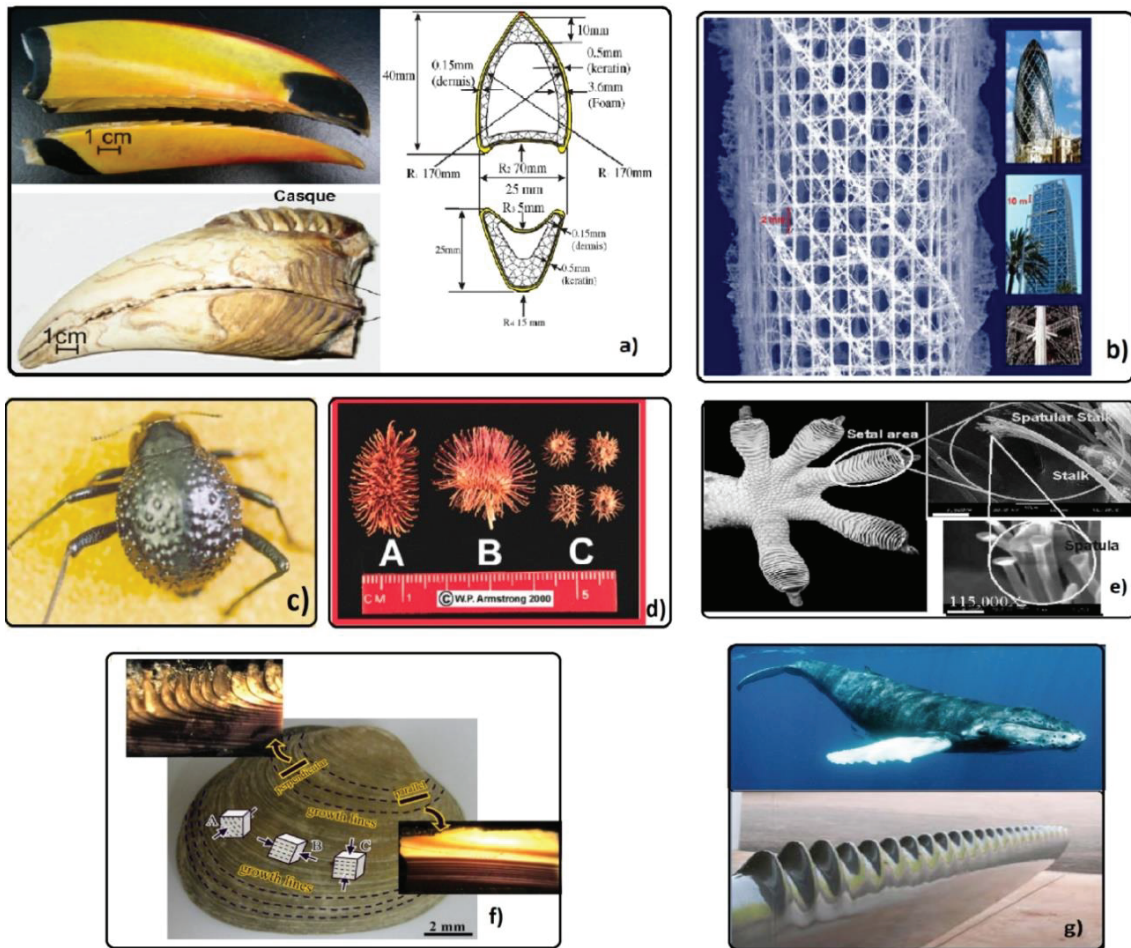


Figure 1.4. a) Beak structure of Tukan birds (Source: Seki et al., 2010), b) Skeletal structure of marine sponge and the buildings inspired by this structure (Source: Meyers et al., 2008), c) *Stenocara* insect species living in the desert and producing their own water (Source: Parker and Lawrence, 2001), d) Burdock burrs showing adhesion ability to different surfaces, e) Gecko's foot and toe tips (Source: Sitti and Fearing, 2003), f) Structure of abalone shellfish (Source: W. Yang et al., 2011), g) Humpback-whale fin and bio-inspired wind turbine blade (Source: <https://whalepowercorp.wordpress.com>).

Frank Fish, a marine biologist, discovered bubbles on the fin of the humpback whale (Figure 1.4(g)). The indentation-like bubbles (tubercles) on the front edge of the humpback whale's fin provide an advantage in terms of hydrodynamic aspects. Fish and Watts patented this application and established a company that develops the wind turbine

blades called 'Whale Power'. The Toronto-based Whale Power Company tested the wind turbine inspired by the whale fin, on the wind farm in Prince Edward Island. The developed turbine blades particularly prevent stalling compared to conventional wings, allowing the turbine to generate more energy at lower wind speeds, and doubling turbine performance. As a result of the researches and tests, it was found that these tubercles reduce noise, increase the strength of the wing, and generate 20% more energy than classical turbines and help to provide 25% more energy absorption from the wind (Tyler, 2008; Aftab et al., 2016; Fish and Battle, 1995; Watts and Fish, 2001).

If brief information is given about fingerprint; fingerprints are small circular papillary protrusions located at the tip of each finger. They are caused by pressure in the developing small fingers of the unborn baby (Champod et al., 2004). The fingerprint development of the fetus is shown in Figure 1.5(b). When the fingertip touches the surface of an object, the materials on the small protuberant ridges and furrows on the fingertips touch to the surface and leave a scar due to sweat gland secretion, which is called a fingerprint (Li et al., 2017; Xu et al., 2015). There are three different glands in the human body. These are eccrine, sebaceous and apocrine. Eccrine is the most important gland used for identification and fingerprint detection in crime scene investigations. The arrangement of the papillary protrusions on the fingers of each human being and the traces that occur due to this arrangement are different. They do not change with growth or with time. There are no two people with the same fingerprint, all fingerprints are unique. The possibility of a fingerprint matching completely by another fingerprint is one in 64 billion. Fingerprints are more unique than the DNA found as genetic material in each of our cells. Even twins with identical or very similar DNA cannot have the same fingerprint. Fingerprints is the most important method of discrimination to reveal the true identity of a person despite changes in his/her identity or denial of false identity and personal appearance due to age, illness, plastic surgery or accident. The use of fingerprints as an identification tool, called dactyloscopy, has become an indispensable part of the modern legal practices.

In 1880, Henry Faulds and William James Herschel reported in an article published in the British Nature Journal that the fingerprint was unique and persistent (Hoover, 2016). Their observations were later confirmed experimentally by the British scientist Sir Francis Galton, who was the first to propose the basic system that classifies fingerprints as arcs, loops and whorls (Champod et al., 2004). Later, this system was

developed by Sir Edward R. Henry and the most widely used classification method today was created. There are several forms of the Henry's system, but the eight basic types of radial loop, ulnar loop, double loop, central pocket loop whorl, plain arch, tented arch, plain whorl and accidental whorl are used by the Federal Bureau of Investigation (FBI) in the United States. The images of different types of fingerprints are presented in Figure 1.5(a) (Davis, 2017). Whorls are generally circular or spiral patterns. The arcs have bumpy (wave-like) lines. Loop-shaped ones make backward turn to themselves without twisting. They are called ulnar or radial depending on their inclination. The radial loop is pointing towards the radius bone (thumb); the ulnar loop is pointing towards the ulna bone (pinky). 65% of the encountered fingerprints is loop, 30% whorl and 5% arc. The most common fingerprint pattern is the ulnar loop (Hoover, 2016). Generally, it is not possible to distinguish most fingerprints directly in daylight, hence it requires special techniques to visualize them. The fingerprint obtained clearly by specific methods is shown in Figure 1.5(c) (Li et al., 2017).



Figure 1.5. a) Fingerprint types (Source: <https://www.touchngoid.com/8-common-fingerprint-patterns/>), b) Fingerprint formation at the 11th week of the fetus in the womb (Source: Champod et al., 2004), c) Fluorescence image of aluminum foil with eccrine fingerprint after dipping into N-1-Cys-coated CdTe QDs solution for 5 seconds (Source: Li et al., 2017).

Usta and Türkmen, Nia and Chahardoli and Yu et al. studied nested structures Figure 1.6 experimentally and numerically and found out that when compared with single thin walled structures with the same outer diameter and height, nested structures possessed better crashworthiness indicators, such as specific energy absorption (Usta and Türkmen, 2019; Nia and Chahardoli, 2016a, 2016b; Yu, Xue, and Chen, 2017).

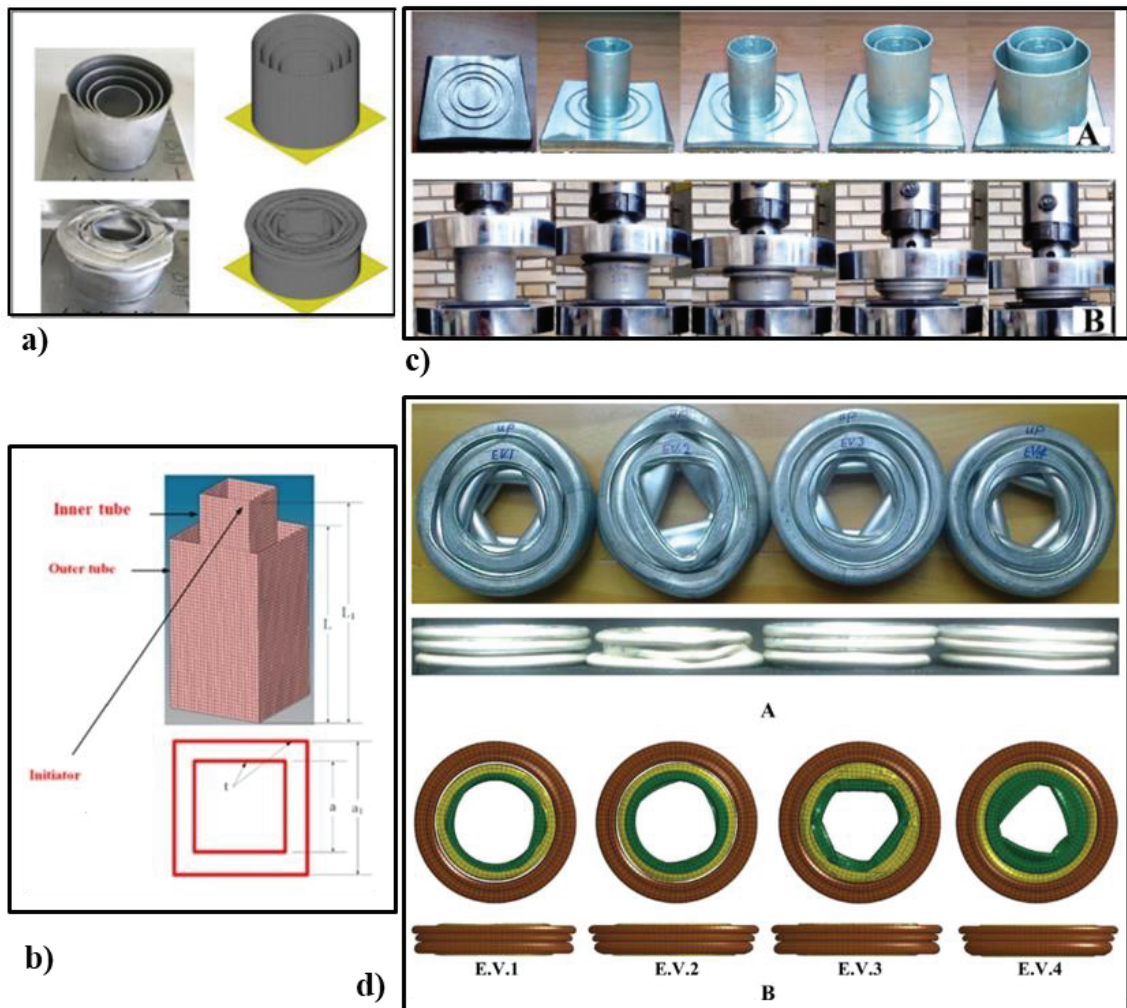


Figure 1.6. a) Empty nested-4 tubes with FE model (Source: Usta and Türkmen, 2019), b) Multi stage nested two-square tube (Source: Tran et al., 2019), c) Multi-tubular 6101 Al alloy structures under quasi-static compression (Source: Nia and Chahardoli, 2016a), d) Deformation of multi-tubular structures under quasi-static compression with FE model (Source: Nia and Chahardoli, 2016b).

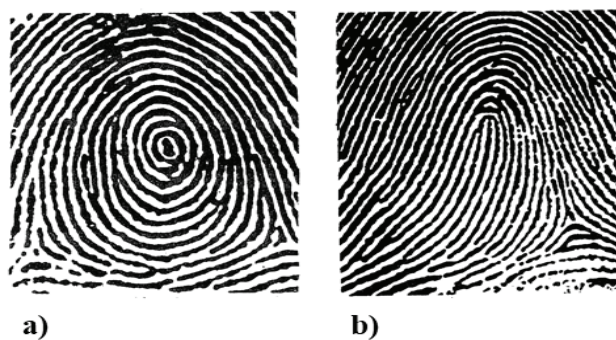


Figure 1.7. Types of fingerprints similar to nested structures: a) Whorl, b) Loop. (Source: <http://www.forensicsciencesimplified.org/prints/principles>)

Fingerprint with its unique spiral structure is analogous to nested structures naturally; therefore, it was assumed that this structure, combination of whorl and loop types (Figure 1.7), would perform better energy absorption capacity when exposed to impact loads as the walls would interact and support each other

1.2.2. Sandwich Structures

Today the structures which are inspired by the nature are being used in many engineering fields. Thanks to their unique features, these structures are able to overcome the challenges of engineering fields and can be integrated into performance improvements of conventional structures. According to the studies in the literature materials inspired by nature are used as core material in sandwich structures. Sandwich structures are composite materials consisted of a thick, low strength and low-density core and two thin high strength plates as faces shown in Figure 1.8. The core structure exhibits high shear strength and energy absorption while the surface plates exhibit high bending and buckling resistance. From this point of view, sandwich structures are able to withstand different loading conditions compared to conventional structures with the help of their high performance (strength or crashworthiness) at relatively low weights. The faces of a sandwich structure are generally in the form of two plates existing at the top and bottom of the structure. They usually have the same material and thickness but in special cases, the surfaces can be designed differently in terms of material type, thickness or sequence etc. These surfaces are designed to resist in-plane loads and flexural moments. The core part of the sandwich structures can be selected from a wide range of relatively lightweight materials, as well as different thicknesses, sequence or geometric parameters. The core, on the other hand, is responsible for the energy absorption, the resistance to damage through thickness direction and resisting the shear loads. Thus, it is an important element in sandwich structures. Sandwich structures are preferred in modern engineering applications due to the diversity of design possibilities offered at the design stage and the versatile crashworthiness characteristics. Sandwich structures, which have high energy absorbing capacity at lightweights, are used in protection and packaging systems, military and vehicle industry.

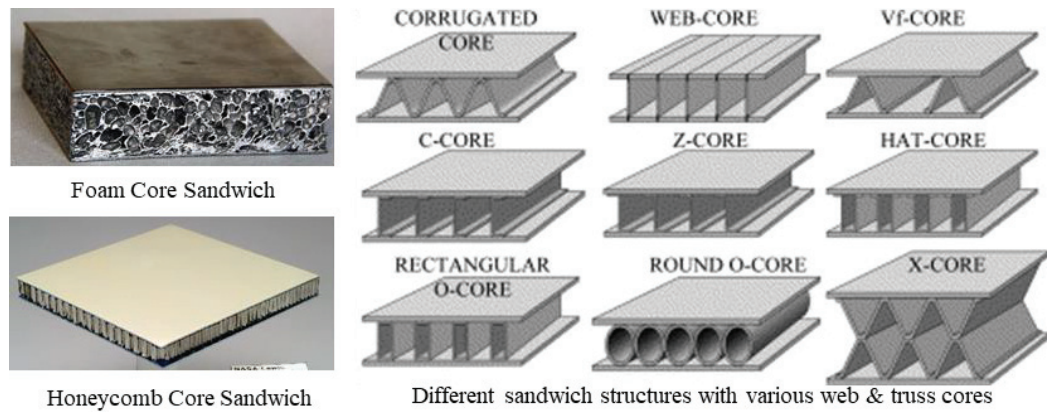


Figure 1.8. Conventional sandwich structures (Source: Bitzer, 1997).

When the existing studies in the literature are examined, it is seen that different sandwich structures and core geometries have been developed by mimicking nature. Especially in recent years, studies on the core geometry have increased with the developments in production techniques.

Yinghan Wu et al. investigated the crashworthiness characteristics of the bio-mimicked sandwich structure with an aluminum honeycomb geometry core and carbon fiber reinforced plastic (CFRP) (Figure 1.11 (a)). They found an increment in energy absorption capacity by using bio-inspired core and CFRP face sandwich, instead of just CFRP as shown in Figure 1.9 (Yinghan Wu et al., 2017) . The peak load of sandwich structures was decreased by adding bio-inspired core as well. As a result, they concluded that by using bio-inspired sandwich structure, the energy absorption capacity can be increased. According to the impact tests performed at three different speeds, sandwich structures containing bio-inspired aluminum honeycomb showed better energy absorption performance between 25.8% and 43.1% than that of carbon fiber reinforced plastic panels.

Wu et al. modeled the honeycomb sandwich structure by mimicking the microstructure of the insect species called Elytra (Figure 1.10) and produced this structure using a 3-D printer. In the three-point bending tests, the produced sandwich structure showed 17.4% higher bending stiffness than the ordinary honeycomb sandwich structure. In addition, optimization studies were carried out to reduce the unit cell weight of the newly developed core structure. The unit cell weight was reduced by 11.8% while showing the same performance (Yuan-qi Wu et al., 2017).

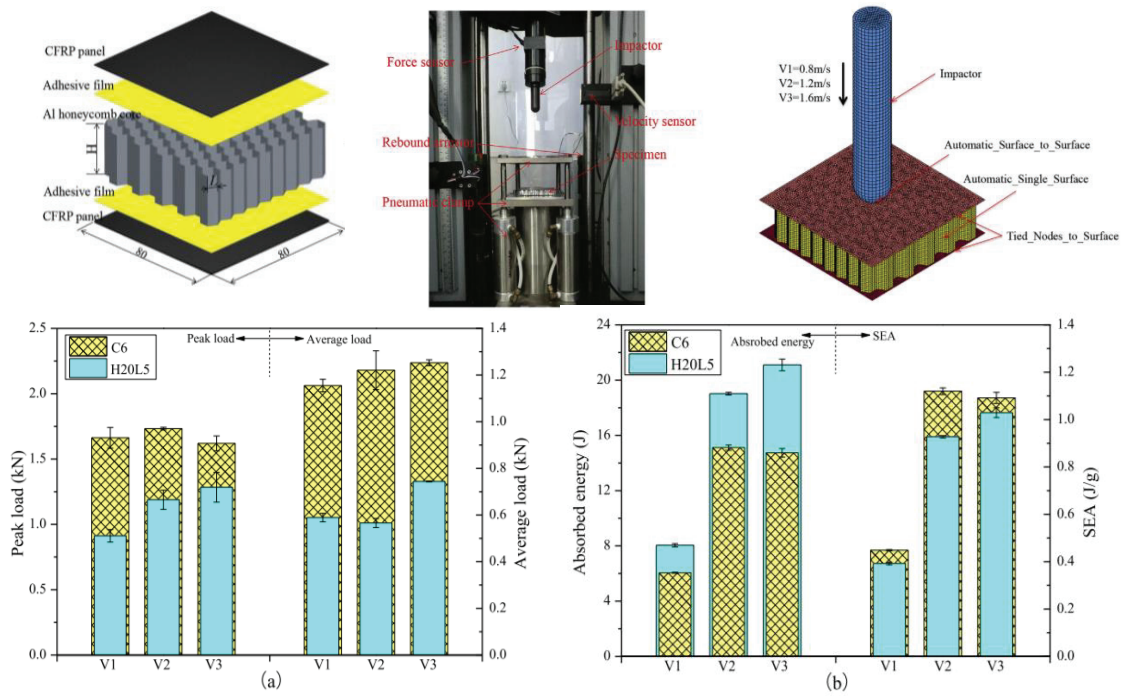


Figure 1.9. Schematic of bio-inspired sandwich structure consisting of honeycomb core and CFRP panels, test setup and FE Model for impact test and test results in terms of load and SEA (Source: Yinghan Wu et al., 2017).

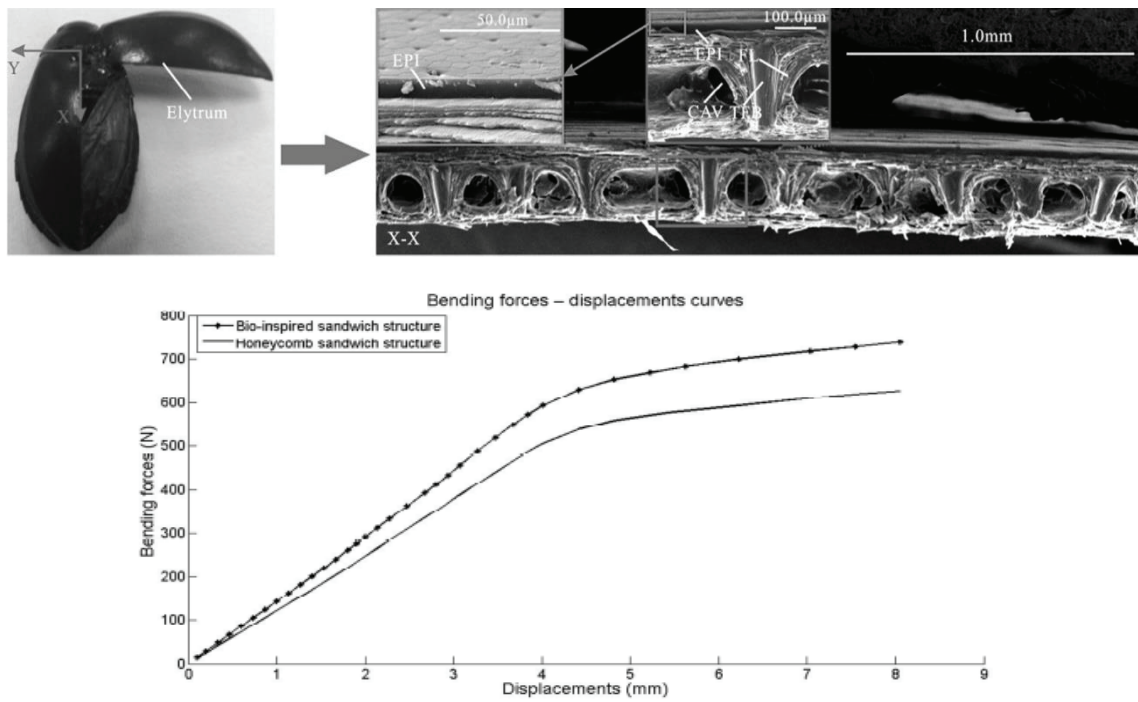


Figure 1.10. Elytra beetle, its microstructure and bending test results. (Source: Yuan-qi Wu et al., 2017)

X. Yang et al. examined the fist size of Mantis shrimp, which is known as the strongest and fastest punching creature in the world, and they recognized that this structure is a zigzag and sinusoidal array structure. Using the biomimicry method, they formed a bio-inspired sandwich structure with a double-sine corrugated core geometry (Figure 1.11(b)). The crushing behavior of this sandwich structure was examined in through thickness direction, it was seen that the energy absorption capacity of this structure, increased significantly compared to regular triangular and sinusoidal corrugated sandwich structures and the initial peak force values decreased (X. Yang et al., 2017).

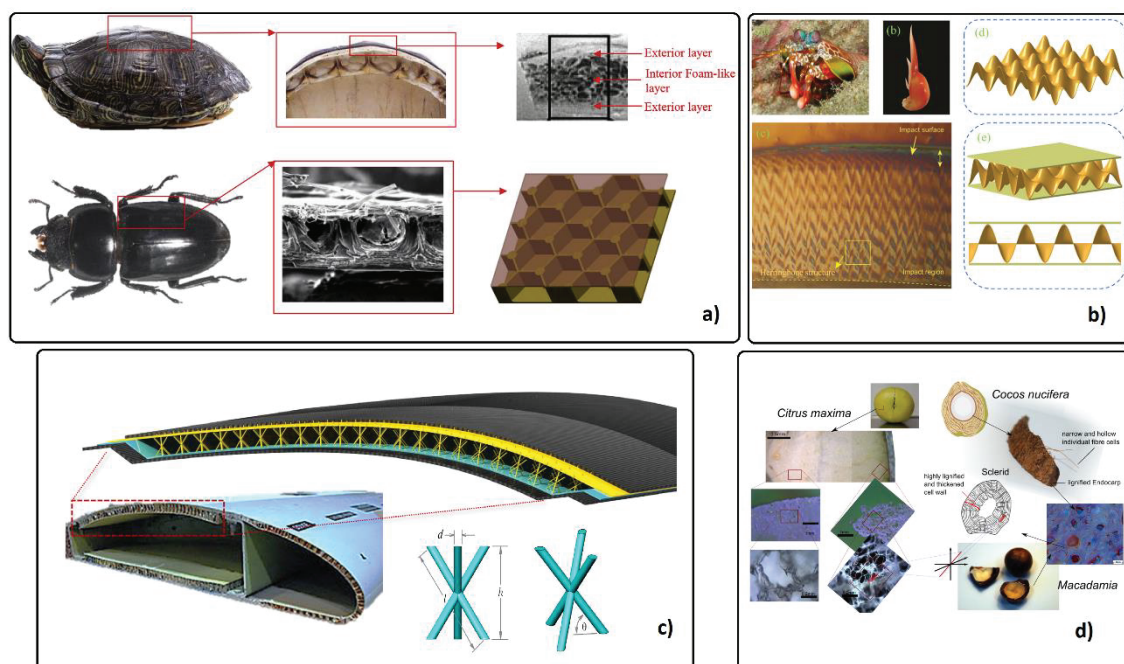


Figure 1.11. Bio-inspired sandwich structures; a) Tortoise shell and insect wing sandwich structure (Source: Yinghan Wu et al., 2017), b) Sinusoidal array core geometry sandwich structure inspired by Mantis shrimp (Source: X. Yang et al., 2017), c) Conceptual design sandwich structure consisting of Kagome core geometry (Source: Ullah et al., 2014), d) Pomelo, coconut shell and macadamia nut structure (Source: Seidel et al., 2010).

Kagome geometry is a core material that is inspired by the rod structure existing in cancellous bone shown in Figure 1.11(c). Ullah et al. produced the Kagome structure by additive production method and applied mechanical tests on different geometric variations (Ullah et al., 2014). According to the results, Kagome geometry showed better compressive and shear strength than conventional honeycomb geometry. Lee and Kang, in their study, investigated the compressive behaviour of Kagome produced by steel wire meshes. Kagome structure with different diameters, strut lengths and number of layers

were examined, and it was concluded that the compressive strength and energy absorption capacity of the Kagome structure is better than aluminum foams, egg box structures and even metal woven textile structures (Lee and Kang, 2010). Hyun et al., on the other hand, showed that the Kagome structure has a superior plastic buckling resistance than the tetragonal support structure under both compression and shear (Hyun et al., 2003). Wadley et al., studied Kagome structure produced by different production methods such as investment casting, metal wire approaches etc. and they found that Kagome offer better strength properties compared to that of tetrahedral pyramid and honeycomb structure with the help of higher specific strength to low relative density ratio (Wadley et al., 2003).

Seidel et al. investigated Macadamia and Coconut structures (Figure 1.11(d)) by performing free fall and cyclic quasi-static compression tests. They found that during the first cycle 75% of the energy is dissipated by the nuts. In addition, the fruit peel of pomelo plant was removed from the its seed and subjected to quasi-static compression tests. It was stated that the structure can recover its initial shape even at high deformation rates. Therefore; they concluded that these types of natural materials can be used to develop new materials with high impact resistance and high energy dissipation (Seidel et al., 2010).

Haldar and Bruck designed a sandwich structure consisting of bio-inspired polymeric foam which is inspired by natural composite material called Palmetto tree as a core and a carbon fiber epoxy panels as a face. The results revealed that the bio-inspired sandwich structure showed better flexural resistance and elastic energy absorption performance than conventional unreinforced core. In addition, the newly developed sandwich structure showed 14 times more volumetric energy absorption capacity than those of conventional cores (Haldar and Bruck, 2013).

The head structure of the woodpecker was used to create a composite sandwich beam, then it was subjected to impact tests (Abo Sabah et al., 2017; Kiam and Hong, 2016). Kiam and Hong applied a low speed impact test by using spring-damper-mass model. The composite sandwich beam and its spring-damper-mass were modeled with numerical programs and the configurations in which the sandwich structure yielded the best results were obtained with genetic algorithm optimization (Kiam and Hong, 2016). Sabah et al., also, studied a sandwich beam consisting of both rubber and aluminum honeycomb cores which is inspired by the head structure of the woodpecker and carbon fiber laminated plates (Figure 1.12). They carried out a numerical and experimental study

in comparison to conventional beams in low speed impact tests at three different energy levels. According to the findings, it was observed that the structure, showed 2.7-5.7 times higher impact resistance than the conventional structure (Abo Sabah et al., 2017).

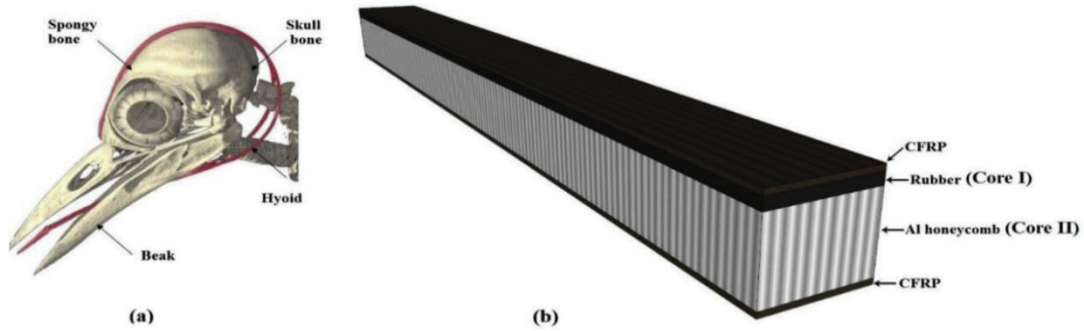


Figure 1.12. a) Head structure of woodpecker, b) Designed sandwich structure consisting of bio-inspired honeycomb core (Source: Sabah et al., 2017).

Taşdemirci et al. developed a thin-walled structure by mimicking the sea creature called “Balanus” and examined the energy absorption characteristics of this structure under dynamic impact loads. Also, they modeled the sandwich structure by FE tool. As shown in Figure 1.13, the conical shaped structure consisting of inner core and outer shell were produced by deep drawing method. According to the results, balanus structure has more energy absorption capacity than inner and outer shell itself under dynamic loads, it was observed that specific energy absorption values increase due to increase of deformation rate. It is stated that the load carrying capacity of the balan structure is higher than the total load carrying capacity of outer and inner parts due to the interaction between the structures. In addition, the increase in average force values, due to increase in interaction, was found to be approximately 5% in the quasi-static strain rates and around 26% in high strain rates (Tasdemirci et al., 2018).



Figure 1.13. Balanus creature and Bio-inspired core (Source: Tasdemirci et al., 2018).

1.2.3. Additive Manufacturing

Additive Manufacturing (AM) is a process which is based on adding materials layer by layer to obtain 3-D objects via polymerization of materials, sintering and selective fusion (Kerekes et al., 2019; Smith and Jeffrey). Figure 1.14 indicates the principle of AM.

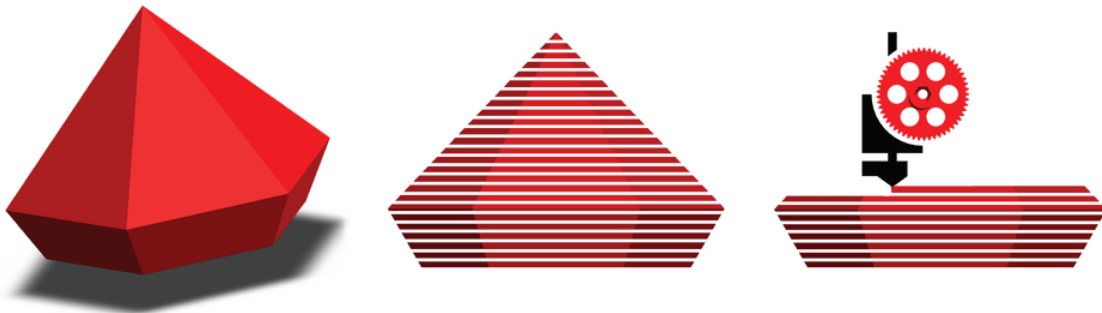


Figure 1.14. 3-D objects manufacturing process via AM Technology.
(Source: <https://aaq.auburn.edu/node/9907/>)

According to desired product in terms of mechanical quality, geometrical accuracy, processing speed and time limitations, different AM technologies can be chosen. The AM families are summarized and categorized according to ASTM F2792 Standard. These are VAT Photopolymerization (SLA), Material Jetting, Binder Jetting, Powder Bed Fusion (PBF, SLM...), Material Extrusion (FDM), Sheet Lamination (LOM) and Directed Energy Deposition (DED, LMD). This categorization can also be done by means of material phase used for production: solid-based systems like FDM, powder-based technologies (SLM, EBM) and liquid-based systems (Inkjet Deposition). Melchels summarized the different types of AM technologies with their pros. and cons. as shown in Table 1.1 (Kanu, 2016, Melchels et al., 2012).

From product customization viewpoint, AM is a good opportunity, compared with conventional machine tooling processes (subtractive manufacturing), for engineers and designers. It is especially used for low-volume production like prototyping. With AM technology, manufacturing steps and waste reduce. Therefore, complexity of parts become independent of the manufacturing steps. In other words, it is cost and time saver with less labor and risk. However, among the injection molding, CNC machining and AM, three dimensional (3D) printed objects by AM can be less strong in some axes due

to its manufacturing principle; nozzle movements and woven direction (Kerekes et al., 2019).

Table 1.1. Classification of AM technologies (Source: Kanu, 2016).

Technique	Accuracy (µm)	Materials	Advantages	Disadvantages	Refs
Inkjet printing (thermal or piezo-electric)	20-100	Liquids, hydrogels	Use of existing cheap technology, multiple compositions	Low viscosity prevents build-up in 3D, low strength	Wilson & Boland, 2003; Boland et al., 2003; Xu et al., 2007
3D printing	50	Polymers, ceramics	Multiple compositions	Requires powder, cell-unfriendly environment	Giordano et al., 1996; Seitz, 2005
Stereolithography (incl. two-photon polymerization)	0.5-50	Hydrogels, polymers, ceramic-composites	High accuracy	Single composition, requires photo-curable material	Arcaute et al., 2010; Lu et al., 2006; Melchels et al., 2010; Chan et al., 2010
Laser direct writing	20	Cells in media	Single cell manipulation	No structural support, scalability	Odde & Renn, 1999
Direct writing	1	Polyelectrolytes	High accuracy	Requires solvents, cell-unfriendly environment, scalability	Gratson et al., 2004; Ghosh et al., 2008
Melt extrusion (Including FDM)	100	Thermoplastics, composites	Technologically simple	Requires strong filament and high temp.	Hutmacher et al., 2001; Zein et al., 2002
Robotic dispensing	100	Hydrogels, polymers, ceramic-composites	Multiple compositions	Relatively low accuracy	Censi, 2011; Pescosolido et al., 2011
Selective laser sintering	50	Polymers, ceramics		Requires powder, cell-unfriendly environment	Antonov et al., 2005; Williams, 2005
Bio-laser printing	10	Liquids	High accuracy at high speed	Low viscosity prevents build-up in 3D	Barron et al., 2004; Guillemot, 2010
Robotic assembly	5	Rigid solids	No heat, light or reaction required	Expensive machinery	Zhang, 2005

The studies on the mechanical behavior of the structures produced by AM are summarized as follows:

Gautam et al. produced the Kagome core structure from ABS plastic material using a 3-D printer and examined the compressive behavior of the structure in different geometric variations and build orientation (Gautam et al., 2018). Zhang et al. produced the honeycomb structure with 3-D printer and investigated energy absorbing performance by through in-plane compression tests. The results revealed that the 3-D printed specimens showed high energy absorption performance (Zhang et al., 2018). Dikshit et al. used the sandwich structures produced by 3-D printer in quasi-static indentation tests (Dikshit et al., 2017). Goh et al. examined the performance of carbon fiber and glass fiber reinforced thermoplastic structures produced by additive production method with tensile

and flexural tests. They concluded that with the help of design flexibilities, AM is very suitable during the development process of novel structures (Goh et al., 2018).

1.2.3.1. Fused Deposition Modeling (FDM)

Fused deposition modeling (FDM), in other words, Fused Filament Fabrication method is based on material extrusion principle by depositing flow of viscous thermoplastic filament using a nozzle. The nozzle is poured the material onto the manufacturing table or already poured material in fibrous form or dots. The material hardens rapidly while being in liquid state at the nozzle tip. The final geometry is obtained from the combination of the layers. Thermoplastic filaments and pellets are the well-known material types that are used in FDM. The demand of the FDM technology is highly increased in recent years and it is expected to be continued in the future. Because it is inexpensive, produced parts have good mechanical qualities and it offers design diversity from the color selection to geometrical flexibility. The manufacturing method is shown in Figure 1.15.

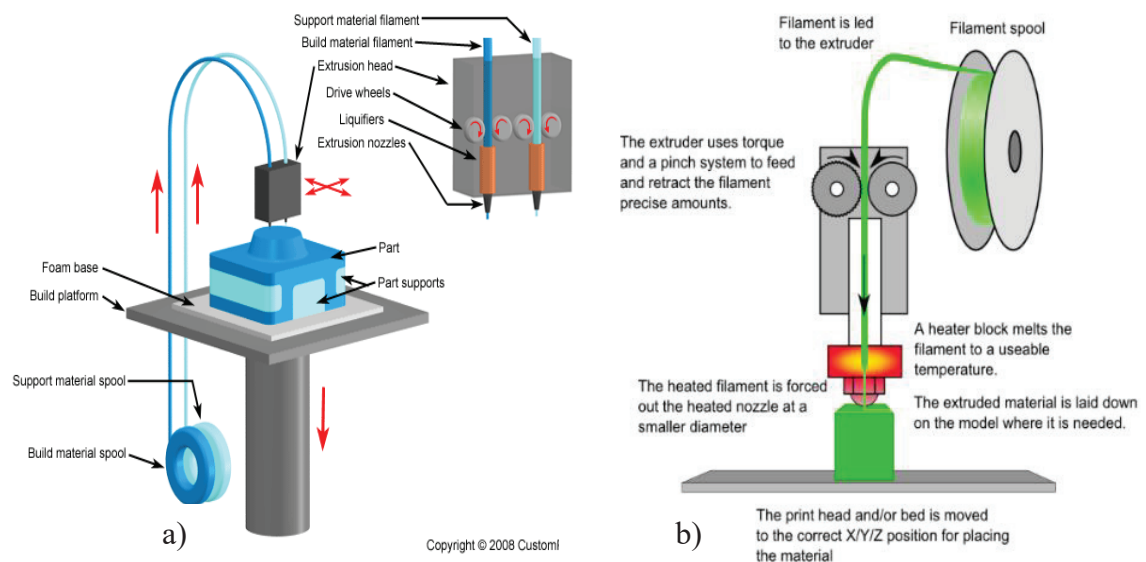


Figure 1.15. Fused Deposition Modeling (FDM) working principle (Source: a) <https://aaq.auburn.edu/>, b) Kanu, 2016).

Polymers and plastics are highly used in FDM procedure because they offer design flexibility, they are durable and available with color alternatives. However, they

have some limitations, such as limited weathering resistance, probable warpage risk and flammability. Acrylonitrile butadiene styrene (ABS filament) is a prevailing plastic used in conventional 3D printers due to its high strength, impact resistance, toughness and durability when compared to other plastics. It has wide range of usage areas from automotive parts and electronic housing to moving parts and packaging applications. On the other hand, shrinkage can be a problem if cooling speed is not controlled. Since the cooling speed depends on nozzle and bed temperature, fine tuning should be done to obtain high quality parts.

Kanu et al. conducted a study and investigated whether the ASTM D638-02a Standard (Standard Test Method for Tensile Properties of Plastics) can be used in the mechanical characterization of the ABS material produced by FDM method. For this purpose, they performed quasi-static tensile tests on specimens produced by injection molding followed by laser cutting and specimens produced by three different types of 3D printers with $\pm 45^\circ$ raster angle and 100% infill density. They found that the mechanical properties of 3D printed ABS samples as shown in the Table 1.2. They concluded that the results are not very different considering the cost and convenience and emphasized that FDM can be used especially in prototyping instead of conventional methods (Kanu 2016).

Table 1.2. Mechanical properties of ABS specimens (Kanu, 2016).

Methods	Modulus of Elasticity (GPa)	Tensile Strength at Yield (MPa)	% Elongation at Yield	Tensile Strength at Break (MPa)
Laser Cutting (avg.)	2.03	30.78	1.96	27.1
3D printing (avg.)	1.9	29.79	2.2	26.6

Sagias et al., investigated the effect of 3-D printing operational parameters on the mechanical properties of the parts by using Taguchi methodology. In this design of experiment research, Fused Deposition Modeling technology with ABS (Acrylonitrile Butadiene Styrene) material were used. As a result of this research, the optimum combination of the printing parameters found as 70 μm layer thickness, solid infill density

and honeycomb print pattern. Also, they noted that layer thickness and infill density are the most influencing factors according to analysis of variance (Sagias et al., 2018).

1.3. Thesis Objective

The scope of this study is to design a novel lightweight sandwich structure with high capacity of energy absorption by mimicking natural geometry. The mechanical response of bio-inspired sandwich structure core, namely fingerprint, was investigated, optimized and compared with other conventional geometries. The selected core geometry is analogous to nested structures naturally; therefore, studying the effect of interaction between the walls of the structure on the energy absorption characteristics was targeted within the scope of this study.

Although there have been many researches on energy absorption characteristics of sandwich and bio-inspired sandwich structures produced by additive manufacturing, only a few researches have studied the sandwich structure produced by FDM. With FDM method, complex-shaped geometries which are difficult to produce by conventional methods can be produced easily at considerably light-weight, like fingerprint core.

Since there is no certain test standard for parts manufactured with 3-D printers, the static and dynamic mechanical characterization methodology specific to these structures was also developed in the scope of the study.

Strain rate effects on the deformation behavior and energy absorption characteristics for a bio-inspired 3D printed sandwich core were analyzed by performing experiments and simulations via finite element code LS-DYNA. The proper material model was selected and modified to better understand the mechanical behaviour of 3-D printed sandwich core.

Bio-inspired sandwich structure consisting of 4 fingerprint core were compared to fourfold individual 3-D printed cores numerically in order to recognize the effect of interaction between the specimens as well as the walls on energy absorption performance under compressive loads.

CHAPTER 2

MATERIALS AND METHODS

This chapter provides detailed information about manufacturing of the 3-D printed specimens that is used for both characterization of ABS plastics and fingerprint core and theory of materials' behavior. In the first part, additive manufacturing process and its effect on material properties are discussed. Then, experiments that were conducted for material characterization are explained with their theory. The mechanical characterization of 3-D printed specimens needs to develop modified testing methodology on previously prepared standards. Although there are certain test standards for plastics under tension and compression loads, these standards cannot directly be applied to specimens produced by additive manufacturing method. Furthermore, since ABS material is strain rate sensitive like most of the thermoplastics, the dynamic tests conducted at high strain rates and their importance on mechanical characterization are as well as the quasi-static tests.

2.1. Design and Production of Specimens by FDM

2.1.1. Determining Process Variables

The FDM machine Stratasys uPrint SE, which has 0.4 mm nozzle diameter and maximum build size 203 mm x 203 mm x 152 mm, was used. This machine uses a well-known thermoplastic which is Acrylonitrile Butadiene Styrene (ABS) with 1.75 mm diameter as a filament. The operation temperature was taken default, which is approximately 300°C for the nozzle tip and 80°C in the chamber, for all of the specimens (tension, compression and fingerprint and conventional cores). Most of the processing variables (layer thickness, feed rate, raster angle) were taken as default value and some of them (build orientation and infill density) were selected. The reason of these selections is explained below.

Among the processing variables, the build orientation has the largest effect on the mechanical performance of 3-D printed objects in terms of strength and strain value at failure. Therefore, mechanical properties of the samples produced with different build directions (flat, on-edge and upright) are very different even if the same 3-D printer and operation parameters are used. According to the studies, horizontal (flat) orientation gives greater mechanical properties compared with perpendicular and vertical directions (Chacón et al., 2017; Rahim et al., 2017). It is also very challenging to perform layer-by-layer production in the other two building orientations (on-edge and vertical); since, the specimen height is relatively too huge, and it is very difficult to keep in balance during the manufacturing. Furthermore, it needs additional supports or bed to produce it upright or on-edge direction (Maso and Cosmi, 2018). Moreover, the dimensional tolerance in horizontal orientation is relatively finer than the other orientational directions. Thus, flat orientation on the XY plane was selected for 3-D printed tension specimens shown in Figure 2.1. With the help of this orientation, applied tension load becomes parallel (in X-direction Figure 2.1 (b)) to the layers. As a result, the delamination between the layers can be minimized. The specimens have greater strength and modulus of elasticity value in build orientation (XY direction) rather than the through thickness direction (Z-direction). In brief, the structures produced with 3D printer exhibit anisotropic behavior like composites due to production method (Kerekes et al., 2019).

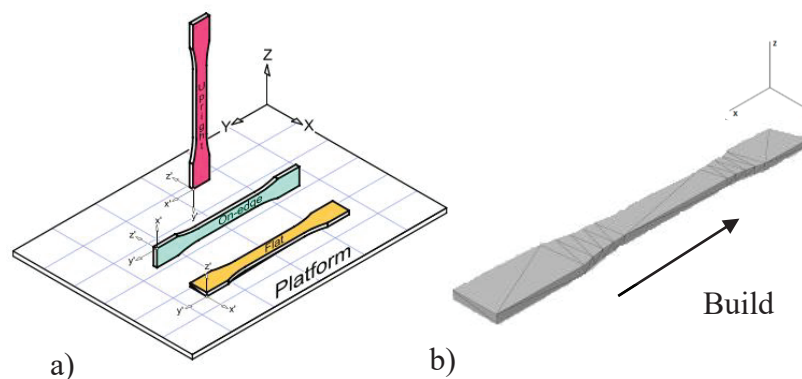


Figure 2.1. (a) Built orientations (Source: Caminero and Caminero, 2017), (b) Isometric view of selected building orientation (flat) of ABS tension specimens.

There are three infill density options; low, high, and solid indicating in Figure 2.2 (a). In the preliminary study, two different infill density options were tested in

compression samples and it was observed that there is no obvious difference between the mechanical properties of the samples. In addition, since there would be more warpage with solid infill density, production was made with the high infill density option for all samples used throughout the study.

The layer thickness (0.254 mm) and the raster angle (+45/-45° mesh-like orientation) (Figure 2.2(b)) were automatically determined by the printer during the manufacturing process. This default features were used because it cannot be changed in uPrint SE due to increase the machine life and obtain same wear in both x and y axes of the machine.

First the outer frame of the specimen was created then, the printer filled the inside of this frame with predetermined raster angle and infill density. The printing process of the specimens is shown in Figure 2.2 (c).

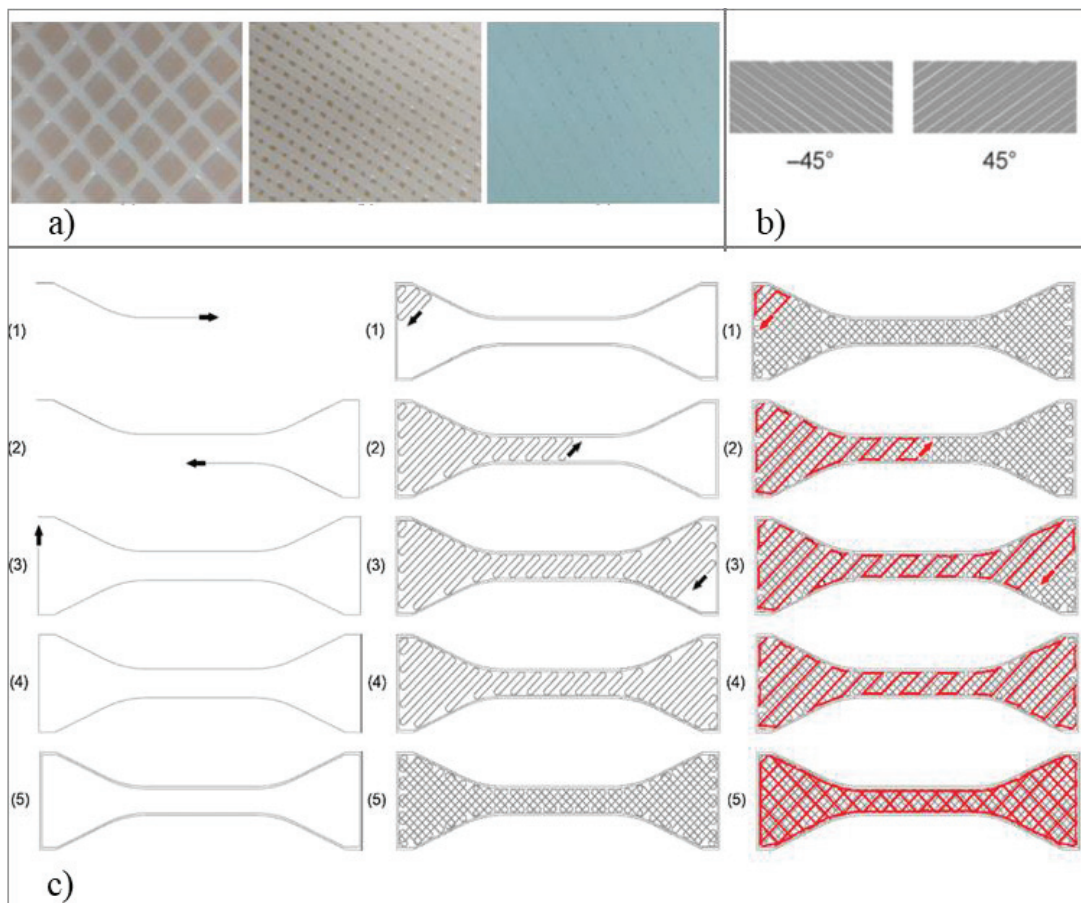


Figure 2.2. (a) Infill densities low, high, and solid respectively, (b) uPrint SE default raster angle, (c) Printing illustration of uPrint SE with outer shell and infill density (Source: Webbe et al., 2019).

2.1.2. Manufactured Parts by FDM

The parts manufactured can be divided into two main categories: for material characterization and for bio-inspired sandwich cores. For the tensile characterization of thermoplastic material, samples having three different geometric types were prepared by AM method keeping production parameters constant. For the compression test, the same geometric sample was used in all tests. In the light of the experience obtained from the material characterization tests, printing operation parameters of the core structure were determined, and then different sizes of samples were obtained with changing the geometric dimensions (height and length). The preparation of tension and compression specimens as well as manufacturing of bio-inspired core structure by AM are explained below. The specimen preparation process by FDM is summarized in Figure 2.3.

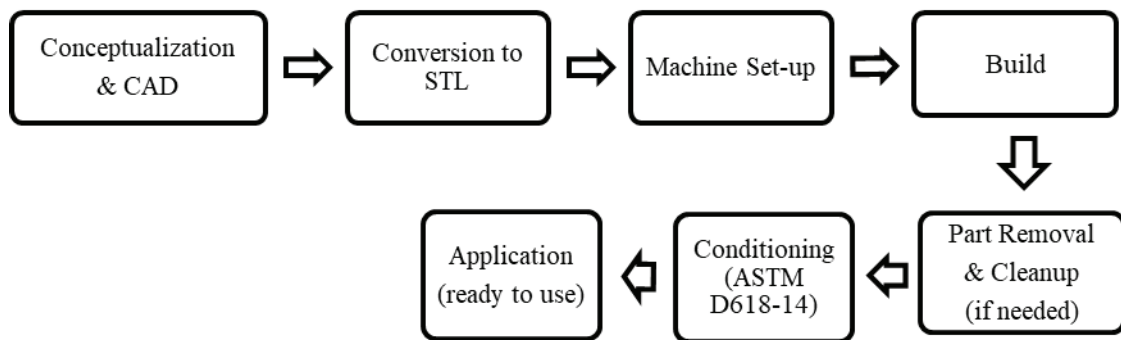


Figure 2.3. Basic steps of FDM process for specimen preparation.

First, ASTM Type I tensile specimens, which was used to obtain tensile property of ABS plastics, were manufactured according to ASTM D638-2a standard which is technically equivalent to ISO 527-1 (ASTM D638-2a). As stated in this standard, it might be used for laminated materials. However, since ASTM-D638 standard is not exactly valid for FDM production, the tensile tests could not be achieved as desired and the tensile samples having different geometrical dimensions were tried. The Type I specimen, which is indicated in Figure 2.4, was manufactured in flat build orientation with high infill density and other parameters (raster angle (+45/-45), feeding rate etc.) were automatically assigned by uPrint SE as discussed above.

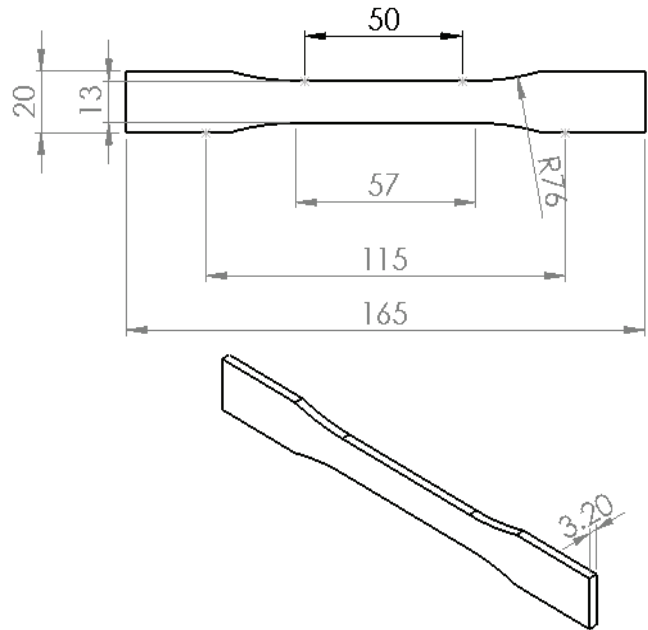


Figure 2.4. Type I, quasi-static tensile test specimen for ABS characterization, according to ASTM D638-02a (Dimensions are in mm).

After that, custom specimen recommended by Prof. Dr. Alper Taşdemirci was manufactured for tensile tests. Also, in dynamic tensile characterization tests, custom specimen was preferred because of having shorter gauge length. It is commonly desired for Split Hopkinson Tension Bar (SHTB) in order to break the specimen by one mechanical wave. The specimen and its technical drawing are shown in Figure 2.5.

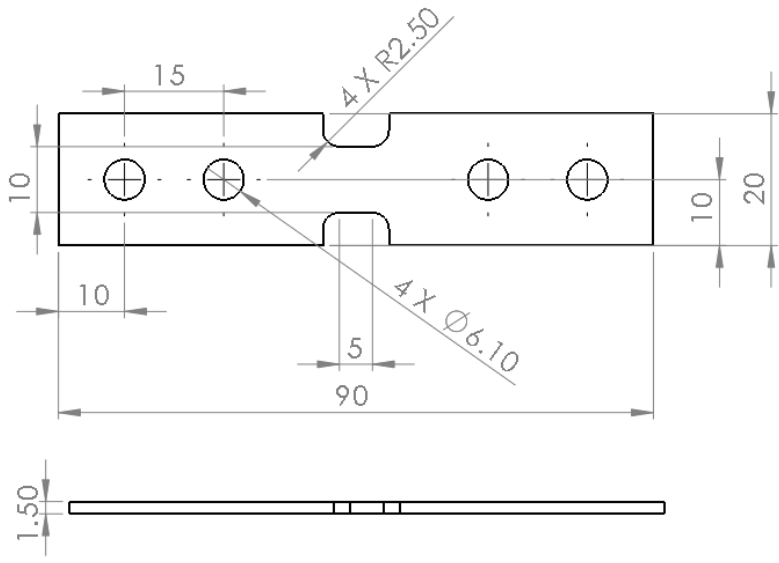


Figure 2.5. Custom tensile specimen used in both quasi-static and dynamic tensile tests for ABS characterization (Dimensions are in mm).

(cont. on next page)



Figure 2.5. (cont.)

The last manufactured specimen in order to use for quasi-static tensile tests was Type IV as specified in ASTM D638-02a. Characterization studies with this sample (indicated in Figure 2.6) provided the desired performance.

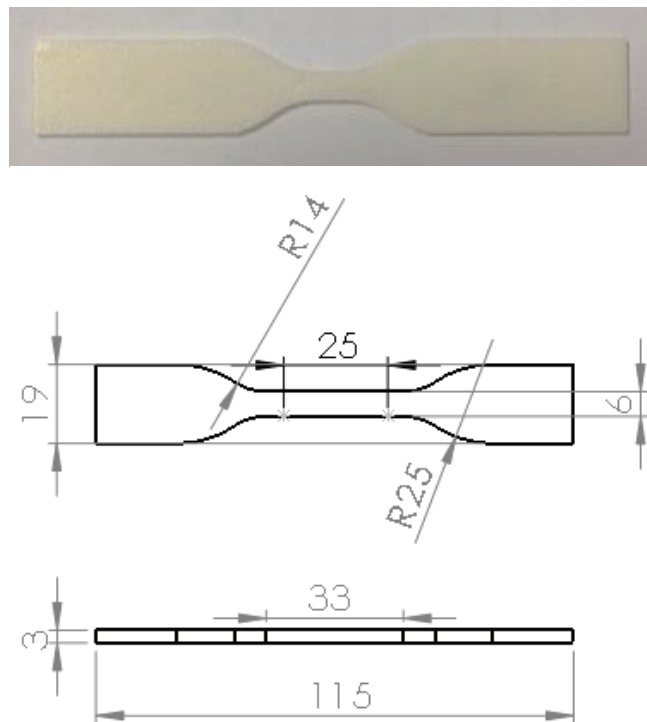


Figure 2.6. Type IV, quasi-static tensile test specimen for ABS characterization, according to ASTM D638-02a (Dimensions are in mm).

After tensile specimen preparation and testing, the quasi-static uniaxial compression and dynamic compression test specimens were produced. Having 8mm diameter and 8 mm height compression specimens were manufactured with flat build orientation. The same manufacturing procedure was valid for the compression specimens as in tensile coupons. Outer ring was printed after then the empty ring was filled with mesh-like high density filling as shown in Figure 2.7 and Figure 2.2(c).



Figure 2.7. 3-D printed test specimen used in both quasi-static and dynamic compression tests.

Finally, fingerprint core structures having different length and thickness values and conventional geometries (cylinder, honeycomb and square) were produced by FDM as shown in Figure 2.8 and Figure 2.9, respectively. Again the same build direction (horizontal) was chosen for obtaining the best mechanical performance and making the manufacturing process easier.

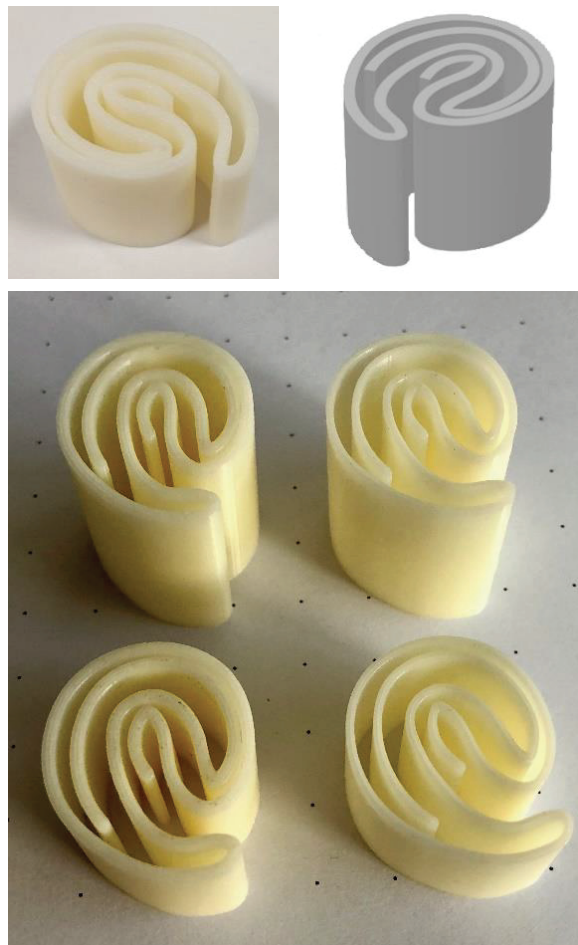


Figure 2.8. 3-D printed fingerprint cores with different height and thickness values.

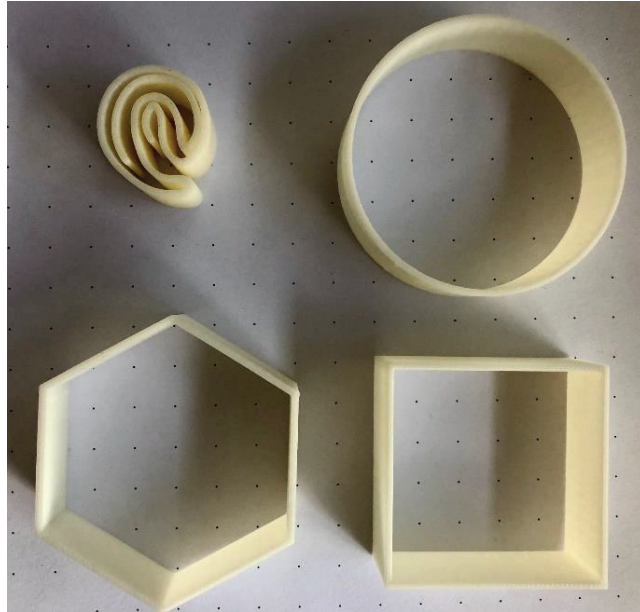


Figure 2.9. 3-D printed fingerprint core and conventional geometries; cylinder, honeycomb and square, respectively.

2.2. Material Characterization and Crushing Tests

In this section, the techniques used in experimental study are presented. The experimental study was conducted for two main purposes: 1) characterization of strain rate dependent behavior of ABS material and 2) evaluation of energy absorbing capacity of sandwich structure's bio-inspired core geometry.

2.2.1. Quasi-Static Testing

Since the quasi-static test set up is more basic than that of dynamic test setup and enables to obtain deformation history, the study was started with the application of quasi-static test. In order to obtain detailed knowledge about the plastic deformation mechanism of 3D printed ABS specimens, continuous monitoring of load and displacement was performed during quasi-static tests.

The most proper method for defining the deformation of materials under applied loads is to conduct a quasi-static test, known as simple tensile test, on flat or cylindrical

samples of the material. Two constants, namely Modulus of Elasticity (Young's Modulus, E) and Poisson's ratio (ν), characterize the behavior of the material in the linear elastic region. The former indicates the constant slope of the stress-strain curve, and the latter shows the ratio of the negative strain in the transverse direction to the longitudinal tensile strain. When the load reaches a certain level, metals and polymers yield, that is, the material no longer behaves in the way it does in linear region; thus, plastic deformation starts. This stage ends with a failure of specimen. The failure of material occurs after the stress reaches a maximum level, referred to as ultimate stress (σ_u), indicating strength of the material. The corresponding strain is called failure strain (ϵ_f), which is an indicator of ductility of the material under tension. Under compression, most materials behave similarly as they do under tension although their materials' constants are different.

Since the aim of the thesis is to design an energy absorbing structure, it should indicate significant plastic deformation. It means that elastic strain of the structure can be neglected. The plastic material response has much more influence on material behavior rather than the elastic properties.

2.2.1.1. Tension Test

One of the most common methods for material characterization is the uniaxial tensile test as mentioned above. A Shimadzu AG-X universal testing machine with maximum load carrying capacity of 300kN (Figure 2.10), was used for quasi-static tension tests. This testing machine enables to perform quasi-static tests at the strain rates ranging from 10^{-4} /s to 10^{-0} /s. A video extensometer was employed as an auxiliary tool to observe the movement of the gauge markers placed on the specimens. The stroke measurements were done by using this video extensometer to obtain more accurate results. Furthermore, a camera was used as a recorder to observe the crack propagation and deformation history. During the study, three different quasi-static strain rates (10^{-3} /s, 10^{-2} /s, 10^{-1} /s) recommended by relevant ASTM standards were applied. The behavior of material subjected to various strain rates was investigated. Due to the anisotropic behavior of 3-D printed parts, premature failure occurred at some of the specimens in the form of delamination at weak bonding regions. Therefore, a couple of precise tests were repeated for each strain rate for compatibility.



Figure 2.10. Quasi- static tension test set-up with different load carrying capacity chins.

2.2.1.2. Compression Test

Shimadzu universal testing machine was used again for quasi-static compression tests of both ABS characterization specimens and bio-inspired cores. In this test set up, fully constrained rigid lower plate was used as a base. The specimen was compressed by downward (z -direction) moving of the upper head at a constant velocity. The desired strain rate was obtained by adjusting the upper cross head velocity using Equation 2.1, where $\dot{\epsilon}$ is the strain rate, V_{CHS} is the cross-head speed of upper moving rigid plate and L is the height of the specimen.

$$\dot{\epsilon} = \frac{V_{CHS}}{L} \quad (2.1)$$

The test set-up for quasi-static compression tests is shown in Figure 2.11 Gauge markers were placed on the moving and fixed heads. Specimens were sandwiched between the moving and stationary plates. In order to detect the movement of gauge-

marks during the test and to observe the crushing behavior of bio-inspired cores the experiment was recorded by the video extensometer and the camera.



Figure 2.11. Quasi-static compression test set-up.

2.2.2. Dynamic Testing

Since the aim of this study is designing energy absorbing structure, it should indicate significant plastic deformation when it subjected to crushing forces. Therefore, the behavior of the material, while undergoing plastic deformation, at high strain rates needs to be examined. Experiments having strain rates between the $10^0/s$ and $10^4/s$ are called dynamic tests. Drop-weight Impact Test and SHPB-SHTB were used as dynamic test tool for both crashworthiness and characterization studies respectively.

Dynamic loads cause rapid deformation and thus high strain rates. Thermoplastic polymers, like ABS, indicate strain rate dependent behavior. Polymer chains in thermoplastic materials which exceed the glass transition temperature slip/slide over each other in the form of viscous flow called as viscoplasticity (Lu and Yu, 2003). The rapid

alignment of polymer chains resulting in strain rate dependency can be expressed by proper constitutive material models and equations which is described in Chapter 3. This strain rate sensitive behavior affects the deformation and energy absorption mechanism of a structure directly.

2.2.2.1. Drop-Weight Impact Test

Fractovis Plus drop weight test device is used for low-to-intermediate dynamic strain rates ($10^0/s$ – $10^2/s$). It gives an idea of energy absorption capability of the structures while applying axial low-velocity impact loads to the specimen. The device is composed of a striker reaching 222 kN maximum force capacity, additional weight attachment unit and weights in order to supply required kinetic energy to the striker, a velocity sensor, and a rigid and fully constrained bottom plate. In this test, the kinetic energy required to crush the sample (at least 75% of specimen height) is obtained by altering impact velocity and additional masses. The device measures the velocity by the photocells of the machine. The impact velocity can be calculated basically or dropped height can be calculated indirectly from free fall equation shown in Equation 2.2 where V is impact velocity, g is gravitational acceleration and h is the drop height.

$$V = \sqrt{2gh} \quad (2.2)$$

Advanced data acquisition system DAS 16000 is integrated to the drop weight to obtain force and displacement values with respect to time and the readings are recorded. Recording with the high-speed camera during the experiment is important to verify the displacement and deformation of the specimens properly. The energy absorbed by the specimen can be calculated by integrating force versus corrected displacement curves. Figure 2.12 shows all the details of drop-weight test set-up.

The strain-rate is not constant because the velocity of the striker is variable until the striker reaches a stationary position. Therefore, this test method was not used for characterization. It was used, however, to simulate the impact event to obtain the energy absorption characteristic of the bio-inspired sandwich structure.



Figure 2.12. Drop-weight test set up with DAS.

2.2.2.2. SHTB and SHPB Tests

Split Hopkinson Tension Bar (SHTB) and Split Hopkinson Pressure Bar (SHPB), consisting of long bars, loading mechanism and DAS including conditioners and oscilloscope, are commonly used testing methods to obtain strain rate dependent behavior of materials for strain rates between the $10^2/s$ and $10^4/s$. In addition to the test apparatus, high-speed camera (Fastcam SA1.1) and light source (Dedolight Daylight 400D) were used as auxiliary elements. The high strain tension loading was conducted by conventional SHTB as indicated in Figure 2.13 Since the experimental setups and theory are similar and only the loads (compressive and tensile), which the specimens are exposed to, are different, only the theory of a SHPB test setup will be explained. The theory is briefly as follows:

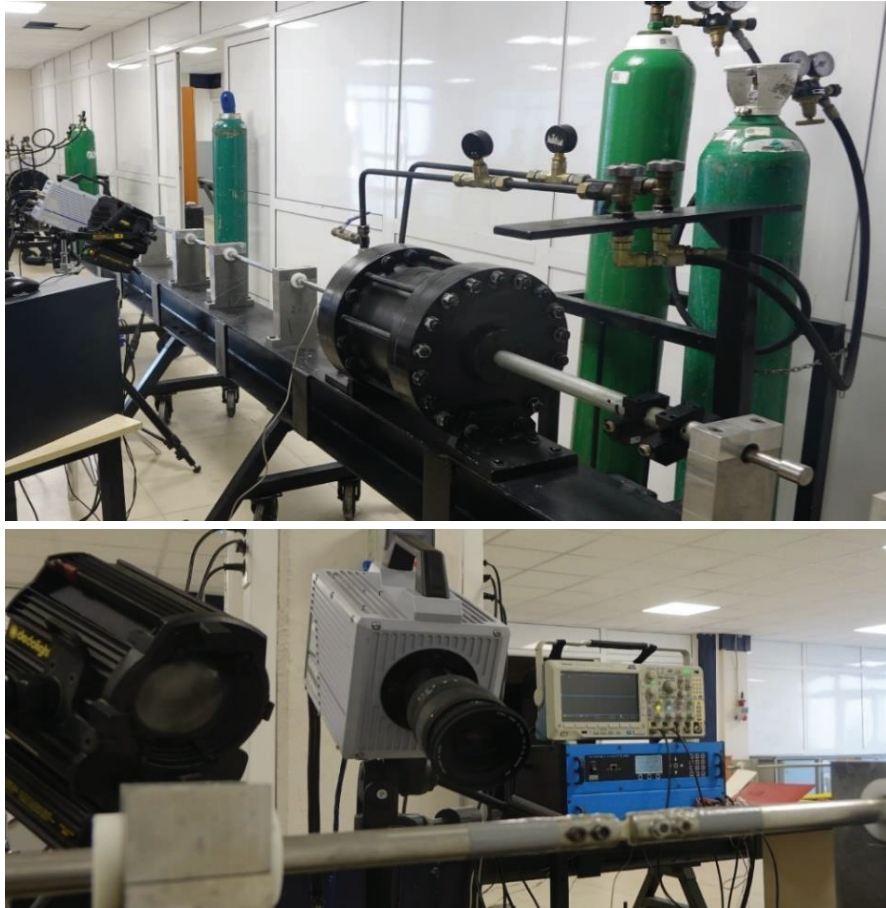


Figure 2.13. SHTB test set-up for dynamic tensile characterization.

The test set-up (Figure 2.14) consists of gas gun which was connected to a striker bar. The striker provides velocity then, the impact velocity is transferred to an incident bar in which the first strain gauge is placed on. The same strain gauge captures the reflected wave. Elastic stress wave, generating from the striker bar, propagates through the incident bar. Then incident bar transmits the wave to the specimen which is sandwiched between the incident and transmitter bar and then reaches to transmitter bar. Thus, the specimen undergoes the plastic deformation. The other strain gauge on the transmitter bar captures the transmitted wave coming through the specimen. The measurements obtained from the strain gauges are transferred to an oscilloscope. Strain gauges with a 2.16 gage factor are positioned at an equal distance over the incident and transmitter bars. Measurements taken with strain gauges usually have small values therefore, signal amplifier is used to read the accurate strain values. With the excitation voltage (10 V) value applied using the signal conditioner, the signals, received from the strain gauges, can be read on the oscilloscope as the voltage value. The output signals are

then converted into strain, stress and strain rate as a function of time. Mechanical behavior of the specimen at high strain rates is obtained from the strain time plots of the bars with the help of proper formulas.

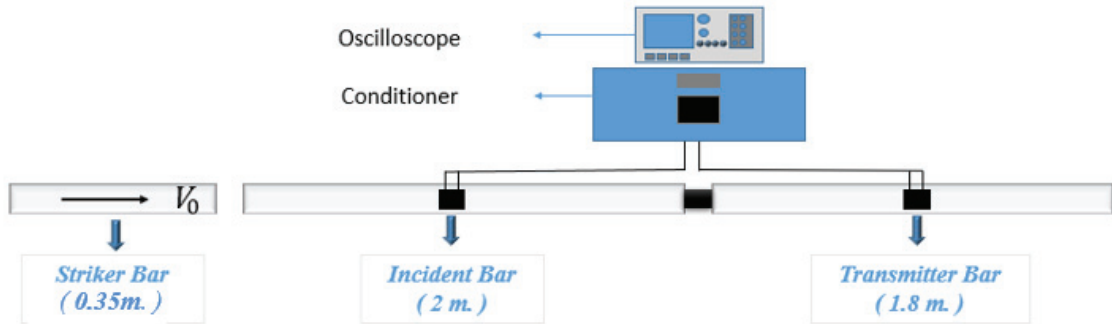


Figure 2.14. Schematic representation of SHPB (Source: Bayhan, 2018).

The main components namely, striker, incident and transmitter bars are made of the same material Vascomax C350 alloy. The material properties of the SHPB components are shown in Table 2.1.

The same working principle is also valid for Split Hopkinson Tension Bar (SHTB) test. However, in this case the striker that exists on the incident bar as a tube shape is pulled through the backward by the gas gun. Therefore, it creates tension wave on the incident bar instead of compression. The schematic representation of SHTB test is shown in Figure 2.15. The physical properties of SHTB components are shown in Table 2.2.

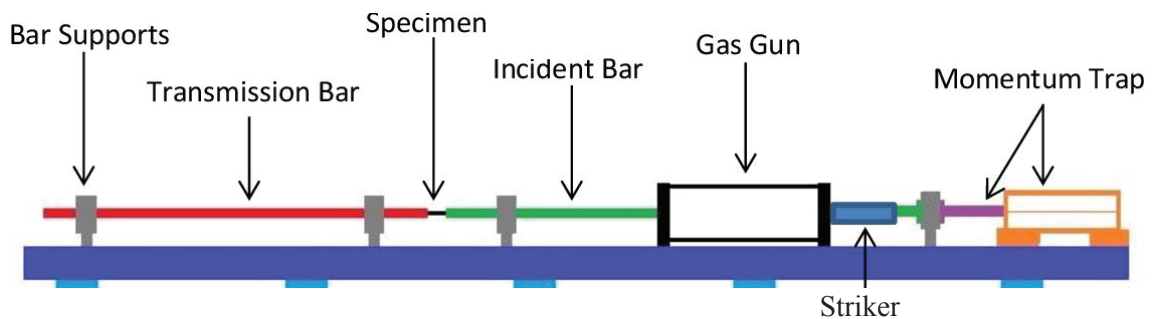


Figure 2.15. Schematic representation of SHTB (Source: Young, 2015).

Table 2.1. Material properties of the Vascomax C350 bars.

<i>Physical Properties</i>	<i>Values</i>
Density	8100 kg/m ³
Elastic Modulus	180 GPa
Poisson's Ratio	0.3

Table 2.2. Material properties of the 316L Stainless steel bars.

<i>Physical Properties</i>	<i>Values</i>
Density	8000 kg/m ³
Elastic Modulus	193 GPa
Poisson's ratio	0.3

Theory of the wave propagation and related formula for the strain as a function of time are described as follows:

Stress wave is assumed to be a longitudinal elastic stress wave (c_L), when the applied load is below the yield strength of the material. E denotes the modulus of elasticity and ρ density of the material in Equation 2.3. This type of stress wave occurs through the incident and transmitter bars when the striker impacts the bars.

$$c_L = \sqrt{\frac{E}{\rho}} \quad (2.3)$$

Plastic stress wave propagation, on the other hand, initiates at the impact region when the stress exceeds the yield limits. For materials having both linear or non-linear strain hardening behavior in which their stress value (σ) is a function of strain (ϵ), the longitudinal plastic stress wave (c_p) can be described by Equation 2.4 This type of stress wave occurs in the specimen which is stiffer than the bars.

$$c_p = \sqrt{\frac{d\sigma/d\epsilon}{\rho}} \quad (2.4)$$

In Equation 2.4, $d\sigma/d\varepsilon$ stands for the tangential modulus of the material. For most materials such as metals, $d\sigma/d\varepsilon$ ratio is two or three orders less than the modulus of elasticity value E , therefore, elastic waves move faster than the plastic waves when the material is subjected to impact loading.

If perfect collision occur between the two collinear bars, which are incident and transmitter, then stress (σ) and strain (ε), and the duration of the incident pulse (T) can be determined by following Equations (2.5)-(2.7), respectively.

$$\sigma = \frac{c_b \rho_b v_o}{2} \quad (2.5)$$

$$\varepsilon = \frac{\sigma_b}{E_b} \quad (2.6)$$

$$T = \frac{2L_1}{c_b} \quad (2.7)$$

where σ is the stress pulse, v_o is the impact velocity of the striker bar, c_b is the wave velocity, ρ_b is the density of the bar, L_1 is the length of the striker and E_b is the elastic modulus of the bar.

The dynamic mechanical response of the structure is obtained from the voltage-time curve by applying the following equations. First, the voltage values are converted into strain value ($\varepsilon(t)$) by Equation 2.8.

$$\varepsilon(t) = \frac{2V(t)}{V_{exc} * GF * K_{gain} * (1 + \nu)} \quad (2.8)$$

Where, V_{exc} is the excitation voltage arranged to 10V, GF is gauge factor, K_{gain} is the gain value arranged to 200 for incident and 800 for transmitted waves.

After that by following the Equations (2.9)-(2.11) the stress, strain, and strain rate values of the specimen with respect to time can be calculated.

$$\sigma_{sp}(t) = E_b \frac{A_b}{A_{sp}} \varepsilon_{trans}(t) \quad (2.9)$$

$$\varepsilon_{sp}(t) = -\frac{2c_{0b}}{L_{0sp}} \int_0^t \varepsilon_{ref}(t) dt \quad (2.10)$$

$$\dot{\varepsilon}_{sp} = -\frac{2c_{0b}}{L_{0sp}} \varepsilon_{ref}(t) \quad (2.11)$$

where; $\sigma_{sp}(t)$ is stress occurred in the specimen, E_b is the modulus of elasticity of the bars, surface areas are denoted as A_b and A_{sp} for the bars and the specimen, respectively, ε_{trans} , ε_{ref} are the transmitted and reflected strain values, $\varepsilon_{sp}(t)$ is specimen strain, $\dot{\varepsilon}_{sp}$ refers to strain rate value of the specimen, L_{0sp} is the initial length of the specimen,.

With the help of the equations shown above, the strain rate and dynamic stress-strain graphs of the 3D printed ABS specimen were obtained. For the dynamic tension characterization this theory was implemented as well by SHTB.

CHAPTER 3

MODELLING

The modeling process of bio-inspired 3D printed core specimen consists of computer aided 3D design, meshing, pre-processing, post-processing and verification with experimental results. After experimental and material characterization studies, numerical analysis were carried out and a model suitable for the behavior of the 3D printed core structure was developed. With the help of this model, the effect of geometry and energy absorption characteristics could be examined for the cases which could not be tested. Numerical studies are promising in terms of test simulations which are difficult to perform and/or causes waste of time and material with over-testing. Material constants and test conditions, however, must be well defined and integrated into the numerical program in the convenient format.

Finite Element Method (FEM), which is one of the numerical tools, is commonly used for engineering problems. Ls-Dyna is a highly used FE tool that deals with these problems especially in military, automotive and aviation areas. Particularly, it is utilized for stubborn problems in which multiple nonlinearities exist. Non-fixed or altering boundary conditions, high deformations (such as crushing, collision) and plasticity behavior of materials (such as thermoplastics) cause nonlinearities.

In this study the designed fingerprint structure contains multiple "non-linear" states due to its manufacturing technique (FDM) and material (ABS plastics), being subjected to new local contacts while being crushed and exposing to dynamic loads. Therefore, using Ls-dyna will give reasonable results and a better understanding about the crushing behavior of fingerprint core.

In this section, first of all, the material model that can predict the material behavior under dynamic loads and its parameters obtained from material characterization tests are explained. Then, models developed for optimizing the core structure and observing the crushing structure are explained.

3.1. Material Model Development

Polymers are highly preferable in many industrial areas such as in automotive industry or industrial products etc. In some cases, these structures are subjected to large strain values (deformation) and high strain rates therefore, choosing suitable material model that takes the strain rate effects into account is crucial.

The ABS material, which is one of the well-known thermoplastics, is relatively complicated material because its mechanical properties depend on strain rate (test speed), load type, temperature etc. The material exhibits non-linear behavior hence it is required to be modeled appropriate material model which including plasticity. General thermoplastic behavior can be summarized as follows: Hookean region, elastic limit region, plastic region followed by yield, and necking (Hopmann et al., 2016; Appelsved, 2012). However, the additive manufacturing principles are based on the layer by layer manufacturing with a predetermined raster angle, it causes the structure to become highly anisotropic (Maso and Cosmi, 2018). Hence, the mechanical properties of 3-D printed ABS structure can be affected adversely such as decrease in modulus of elasticity or early and unexpected brittle failure due to high strain rate levels. Nevertheless, with appropriate selection, it is possible to model polymeric structures by selecting available material models that are most convenient for the material behavior itself.

A suitable material model which takes the strain-rate dependent behavior of the material into account was chosen. MAT_PIECEWISE_LINEAR_PLASTICITY (MAT_24) (LSTC, 2016) which is an elasto-plastic material model with rate dependent plasticity was combined with MAT_EROSION card including proper failure/erosion parameters in order to be compatible with the behavior of thermoplastic material. This material model is accurate, relatively simple and gives good prediction where the plasticity (non-linearity) is of interest. When the characterization results of 3-D printed ABS were investigated, it was found that the material's modulus of elasticity did not change with strain rate like metals. Therefore, MAT_24 was used in modeling of the core structure (Lobo, 2008).

In MAT24 material model, deviatoric stresses can be determined by using Equation (3.1), shown as below:

$$\phi = \frac{1}{2} s_{ij} s_{ij} - \frac{\sigma_y^2}{3} \leq 0 \quad (3.1)$$

Where the yield function can be defined as:

$$\sigma_y = \beta [\sigma_0 + f_h(\varepsilon_{eff}^p)] \quad (3.2)$$

In simulations, the hardening function, $f_h(\varepsilon_{eff}^p)$, was defined in tabular data as stress versus strain curves for each varying strain rate. With the help of β parameter, strain rate effects were considered. The load curve, which is the scaling factors of yield stress versus each strain rate, was defined as the β parameter.

The deviatoric stresses are updated elastically with respect to yield function. The deviatoric stresses are expected if the update check is fulfilled. If it is not satisfied, the plastic strain increment is calculated by Equation (3.3):

$$\Delta \varepsilon_{eff}^p = \frac{\left(\frac{3}{2} s_{ij}^* s_{ij}^*\right)^{1/2} - \sigma_y}{3G + E_p} \quad (3.3)$$

Where G and E_p is the shear modulus and plastic hardening modulus, respectively. The trial deviatoric stress, s_{ij}^* , is scaled back by Equation (3.4) (Livermore Software Technology Corporation, 2017):

$$s_{ij}^{n+1} = \frac{\sigma_y}{\left(\frac{3}{2} s_{ij}^* s_{ij}^*\right)^{1/2}} s_{ij}^* \quad (3.4)$$

As it is shown in Figure 3.1, this material model allows the definition and tabulation of stress-strain curves for each varying strain rate values. As mentioned in the previous chapter, the plastic material response has much more influence on material behavior rather than the elastic properties. This material model uses true yield stresses vs. true plastic strain values for the same reason. Interpolation is performed when the strain

rate values fall in between the limits. If the strain rate value does not fall in between the limits of varying strain rate values, the material behavior, then, is determined according to the first or last curve definition. Therefore, material characterization at a wide range of strain rates is crucial for detailed modeling and obtaining realistic behavior (LSTC, 2016).

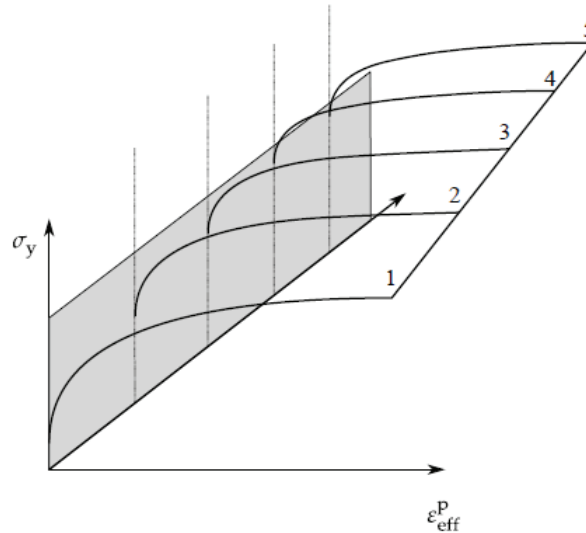


Figure 3.1. True Yield stress vs true plastic strain curves for implementing rate sensitivity (Source: LSTC, 2016).

When the preliminary analysis of 3-D printed structure was done using both tensile and compression curves separately and the results were compared, it was observed that the compression curve was dominant in the crushing behavior of the material. This may be due to its manufacturing technique (layer-by-layer production) resulting in porosity and the voids existing between each raster and layer. Therefore, the compression curve in the form of true yield stress vs. true plastic strain for $10^{-3}/s$ strain rate value was taken as a base curve. The curves obtained from material characterization were compared for different strain rates and yield stress scaling factors were obtained with respect to the base compression curve. The $10^{-3}/s$ curve was multiplied by these scaling factors to obtain the material curves at various strain rates (Figure 3.2). This tabulated data and scaling factors were used instead of Cowper-Symond plasticity equation for the same purpose.

In addition to this material model, material failure (element removal from the core structure) was activated with EROSION card instead of using failure strain in material card in order not to deviate the material behavior from the intended way. Therefore, in preliminary analysis, failure was not allowed. After the model response is better

understood, EROSION card with appropriate failure parameters, which were obtained from tensile experiments, was activated. Consequently, crack propagation was modeled properly, and deformation histories compared to experiments.

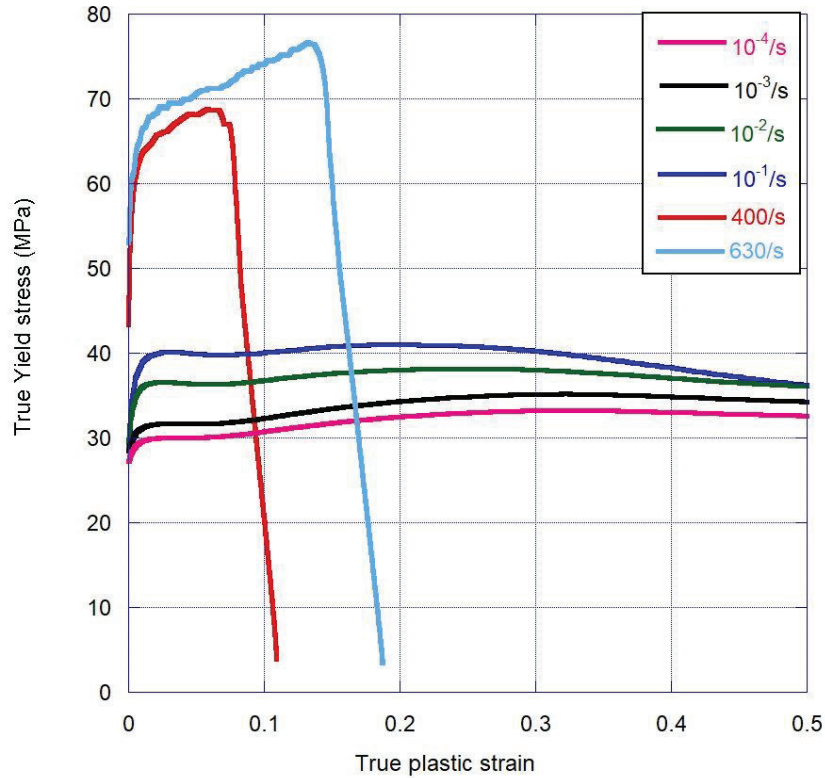


Figure 3.2. Material model input curves for yield stress scaling factors with respect to varying strain rates.

The material model card used for the core structure is summarized in Table 3.1. All of the material constants and defined curves were obtained with experimental study.

Table 3.1. MAT24 material model parameters for fingerprint core.

Definition	Value
Density, ρ (kg/m ³)	935
Elastic modulus (compression), E (GPa)	1.33

(cont. on next page)

Table 3.1. (cont.)

Poisson's Ratio	0.35
Load curve (LCSS): Yield stress versus effective plastic strain (in uniaxial case, it is equal to true yield stress vs. true plastic strain)	Table was defined for each strain rate value
Load curve (LCSR): Load curve ID defining strain rate scaling effect on yield stress	Load curve scaling factor vs. strain rate was defined

3.2. Modeling of Experimental Tests

Finite element code Ls-Dyna was used as a implementation of crash analysis. Fingerprint specimen was designed in computer-aided-design tool (CAD) SolidWorks and was transferred to the HyperMesh by IGES (Initial Graphics Exchange Specification) extension. The solid fingerprint geometry was discretized to brick (solid) elements in HyperMesh (Figure 3.4). The upper and lower plates, on the other and, were modeled in Ls-PrePost directly without using CAD and mesh generator program. Initial and boundary conditions were identified according to the experimental data. After successful completion of the simulation, the post-process was performed and the results were compared with the experimental data. Schematic representation of modeling approach is shown in Figure 3.3.

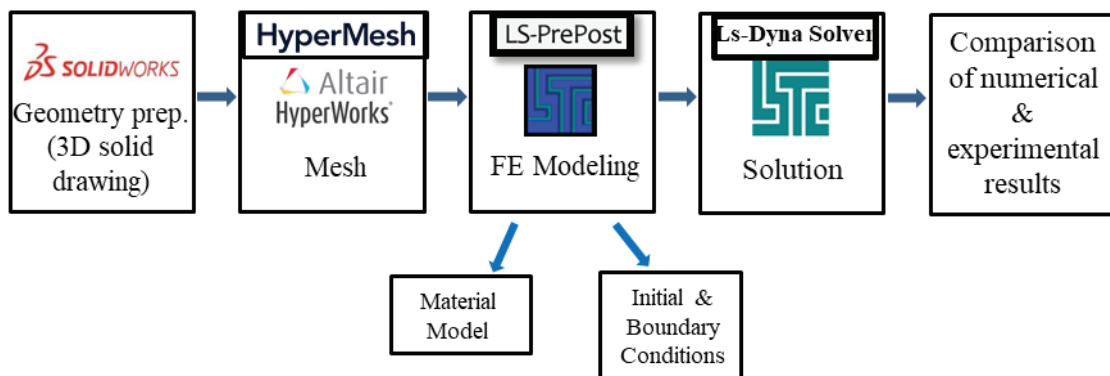


Figure 3.3. Schematic representation of FEA steps.



Figure 3.4. Sketch, 3D solid drawing and discretized model of fingerprint core.

The optimized fingerprint, having around 30 mm outer diameter, 1.5 mm thickness and 20 mm height, was discretized into 11400 eight-noded brick elements with six degrees of freedom per node. Instead of higher-order elements, simple order elements were used for model efficiency (Fasanella and Jackson, 2002). Therefore, hexahedral element formulation (ELFORM 1: under integrated constant stress) was selected. The fingerprint consisted of three elements through thickness in order to provide enough integration points. The mesh discretization kept fine enough to eliminate large deformations due to coarse mesh size. However, to minimize computational cost, usage of very small element size was avoided. The element size of fingerprint is kept almost uniform both in axial and circumferential direction which is approximately 1mm. In preliminary studies coarser (2 mm) and finer (0.75 mm) mesh size alternatives were tried as well as chosen element size. Having approximately 1 mm element size and uniform mesh density distribution gave the accurate results with a reasonable CPU cost.

Zero energy modes should be controlled in one-point integration solid elements in order to overcome the hourglassing modes. Hourglass control Type 5; Flanagan-Belytschko stiffness form exact volume integration with 0.15 hourglass coefficient and Type 6; Belytschko-Bindeman strain corotational stiffness form were selected for explicit and implicit analysis, respectively. Viscous damping coefficient (VDC) was activated in contact card to eliminate the undesirable hourglass modes for the high-speed crushing simulations.

In order to simulate quasi-static and dynamic tests the numerical model was developed in Ls-PrePost shown in Figure 3.5. All parts in the models were created by constant stress solid elements. The cross heads were modeled as RIGID.

In crush analysis, initial conditions are very important as well as material model definitions. Initial velocity was defined in upper-moving rigid plate by INITIAL_

VELOCITY_GENERATION and BOUNDARY_PRESCRIBED_MOTION_RIGID for explicit and implicit simulations, respectively. The specimen was sandwiched between the upper moving plate and fixed bottom plate. In drop-weight analysis, additional mass (20kg) was assigned to top moving head with ELEMENT_MASS_PART option.

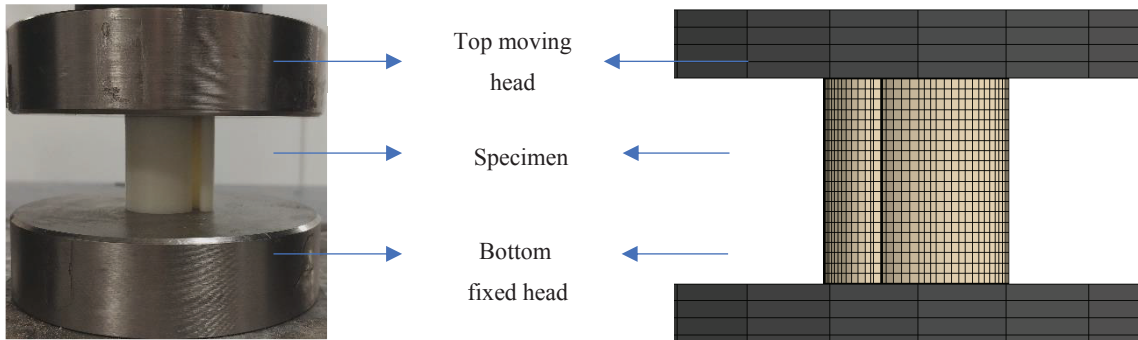


Figure 3.5. Fingerprint crushing test set-up and its model.

Penalty-based contact definitions CONTACT_AUTOMATIC_SURFACE_TO_SURFACE and CONTACT_ERODING_SINGLE_SURFACE were used with SOFT=1 (Soft-Constraint-based approach) in order to get rid of contact troubles. In this option, the contact stiffness is calculated with respect to the nodal masses and the global time step size as shown in Equation (3.5).

$$k = SOFSCL \frac{m}{\Delta t^2} \quad (3.5)$$

Where m is the nodal masses and Δt is the global time step size. SOFSCL is equal to 0.1 by default. This type of contact stiffness calculation is suitable for the contact between the parts made of different materials. Between the heads and the specimen static and dynamic contact friction coefficient were found numerically by trial and error method as 0.3 and 0.25, respectively. Since the stiffness values of heads and specimen are different, viscous damping coefficient (VDC) value was set to 0.20 (20%) to eliminate oscillations as mentioned before. The wall interaction of the core structure was modeled by combining self-contact definition (CONTACT_ERODING_SINGLE_SURFACE) with setting EROSOP and IADJ to 1 and MAT_EROSION to observe damage behaviour properly.

For the optimization of fingerprint structure a couple of dynamic analysis were performed by varying the geometric parameters, as indicated in Figure 3.6 and Figure 3.7. Thicknesses were set to 1 and 1.5 mm, while heights to 20,30 and 40 mm. Hence, 6 different models were created.

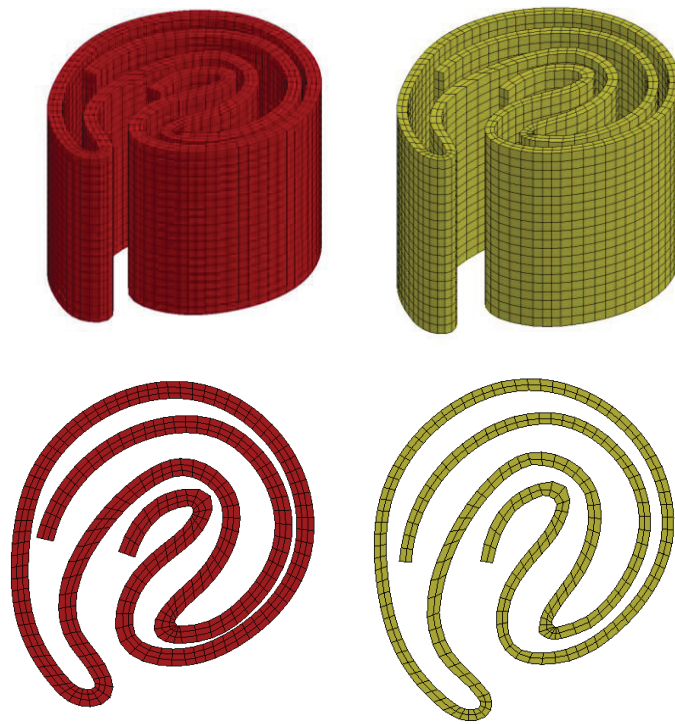


Figure 3.6. Fingerprint cores with different thickness (1.0 and 1.5 mm) values.

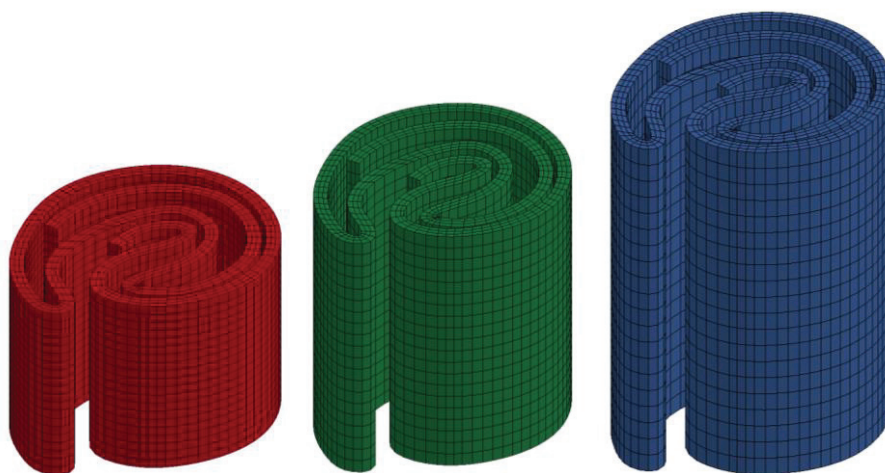


Figure 3.7. Fingerprint cores with different height (20, 30 and 40 mm) values.

In addition, in order to compare the fingerprint structure with other conventional structures, nested designed models having the same areal density were created as shown in Figure 3.8. This was aimed because the helical (spiral) structure of the fingerprint is desired to be applied to other models in a similar analogy. Thus, geometries having the same areal density, the same height and weight were obtained, and energy absorption capacities were compared to each other.

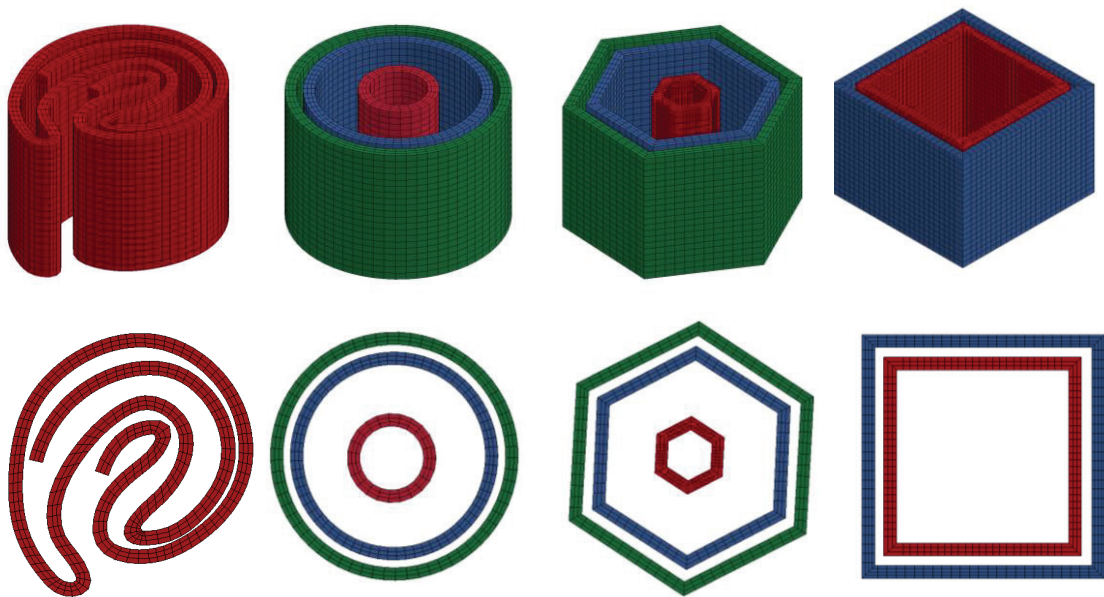


Figure 3.8. Fingerprint and conventional geometries (cylinder, honeycomb and square) having the same areal density, same height and mass.

After the numerical model of the single core structure was developed and crushing simulations were validated with experiments successfully, 4 fingerprints were placed in a geometric pattern and placed between aluminum face sheets and a sandwich structure was obtained as shown in Figure 3.9. The obtained sandwich structure was compared with experimental values of a single fingerprint geometry by multiplying the experiments by 4.

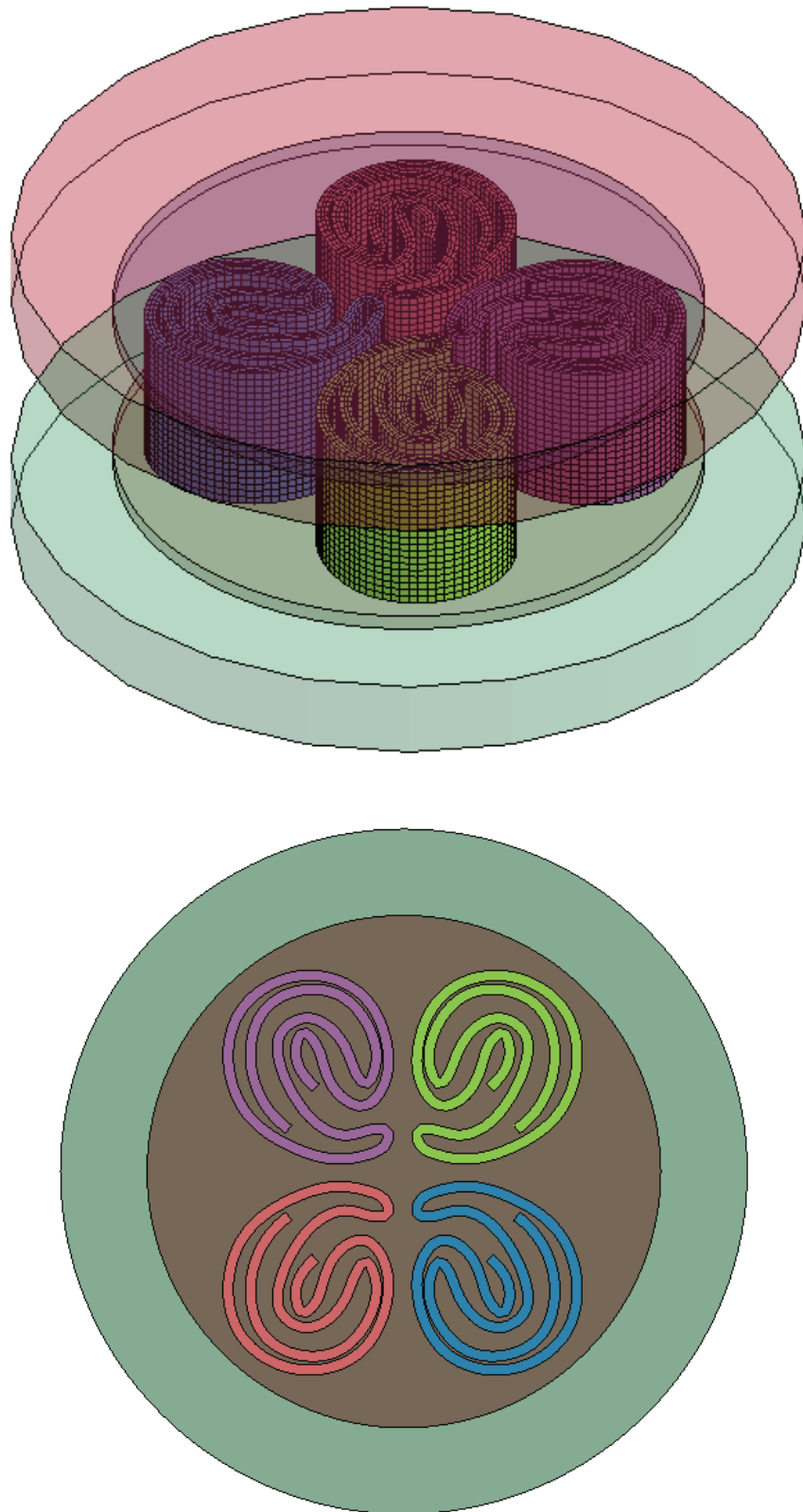


Figure 3.9. The sandwich structure consisted of 4 fingerprint as a core and Al face sheets.

CHAPTER 4

RESULTS AND DISCUSSION

4.1. 3D Printed ABS Material Characterization Results

As stated in ASTM D638-2a, “Standard for tensile properties of plastics”, this standard can be used for characterization of laminated materials. Also, Kanu investigated whether this standard is suitable for specimens produced by AM method and he concluded that it is applicable for 3D printed samples (Kanu, 2016). Considering these, ASTM D638 standard was used at quasi static tensile characterization tests. Furthermore, according to ASTM D618-14, “Standard for Conditioning Plastics for Testing”, the printed specimens were maintained for at least forty hours at room temperature.

3D printed ABS samples exhibit initially Hookean (linear) behavior and then plastic deformation starts, then the samples reach ultimate stress value. After these, engineering stress starts to decrease while strain increases until the failure. Sometimes, the failure can occur suddenly with a crack propagating due to the existing voids or delamination, however, most of the times failure occurs without any discontinuity. In fact, failures which appear suddenly are undesirable because, they cause misinterpretation of material behaviour.

First, quasi-static tensile tests with Type I tension specimen according to ASTM D638-2a Standard were performed to plot the engineering stress-strain curves shown in Figure 4.1. The testing speed was 5 mm/min which refers to 10^{-3} /s strain rate value. Due to the nature of the additive manufacturing (anisotropy, voids between layers) the specimen underwent failure earlier than expected as mentioned above. Hence, the modulus of elasticity, and failure strain values were affected negatively. Thus, these values were found to be lower than those reported in the literature. Although the raster angle, which is the most influential parameter on mechanical properties, is the same, the results did not match completely. Even though the percent of elongation at yield (approximately %2) was similar for both results, the failure strain and tensile strength at yield values were from the given in the literature (Kanu, 2016). The fact was thought to

be due to the differences in the 3D printers and their operation parameters (build orientation, infill density, feed ratio etc.) used in the studies. It was observed that, unexpectedly, none of the specimens either in the present work or literature was broken in the middle part.

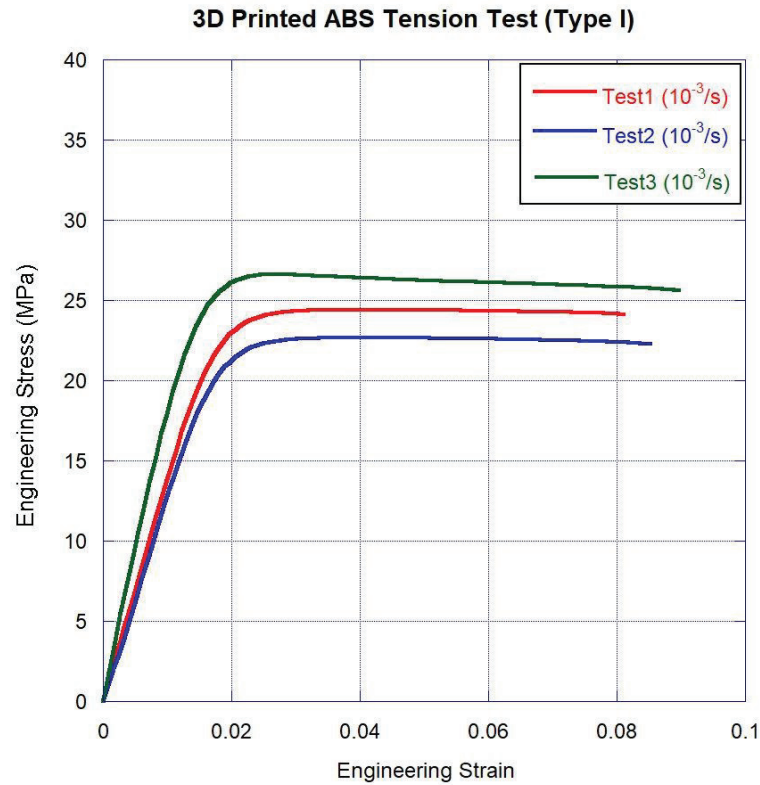


Figure 4.1. Quasi-static tensile stress-strain curves of 3-D printed Type I tensile specimens.

As stated in the literature, the specimens manufactured by FDM technique exhibit ductile-to-brittle transition compared with the polymers manufactured by conventional methods such as injection molding (IM). Although, there is no significant variation in stiffness of FDM and IM samples, the strain value at break decreases dramatically resulting in reduction in toughness proportionally. Since toughness is the area under the stress-strain curve until the fracture of the material, in other words absorbed energy by the material per unit volume, its value is directly dependent on the failure strain. The reason behind this phenomenon is caused by FDM production principle and can be explained as follows: In layer-by-layer production, the underlying cold layer is bonded with the hot layer coming from the nozzle. Because of the temperature gradient between the layers, stress concentration occurs at the interface of the layers and cause further

delamination resulting in sudden failure with a brittle behavior at a lower strain level than it normally proceeds. The same results were reported by other researches (Rahim et al., 2017).

As it can be seen from Figure 4.1, the test results also show inconsistencies for the same strain rate due to premature failure. For this reason, quasi-static tensile tests were performed again with a new custom geometry, which was used in dynamic tensile characterization as well, with the same operational conditions as discussed for Type I. As it can be seen in Figure 4.2, although the obtained failure strain values are almost consistent with the literature, the yield and failure stresses are lower than expected. Since the surface finish at the radius corners of 3D printed specimens were relatively poor, failure started at these corners. Strain softening followed by brittle-like failure was observed. Thus, the specimens failed at the undesired point (at the root of corner), as shown in Figure 4.3.

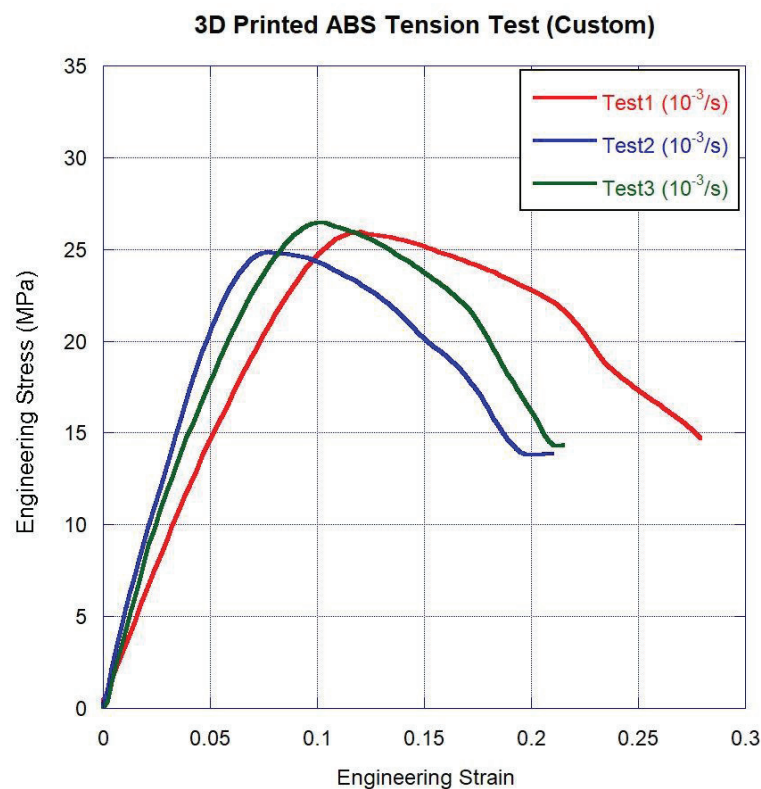


Figure 4.2. Quasi-static tensile stress-strain curves of 3-D printed Custom tensile specimens.

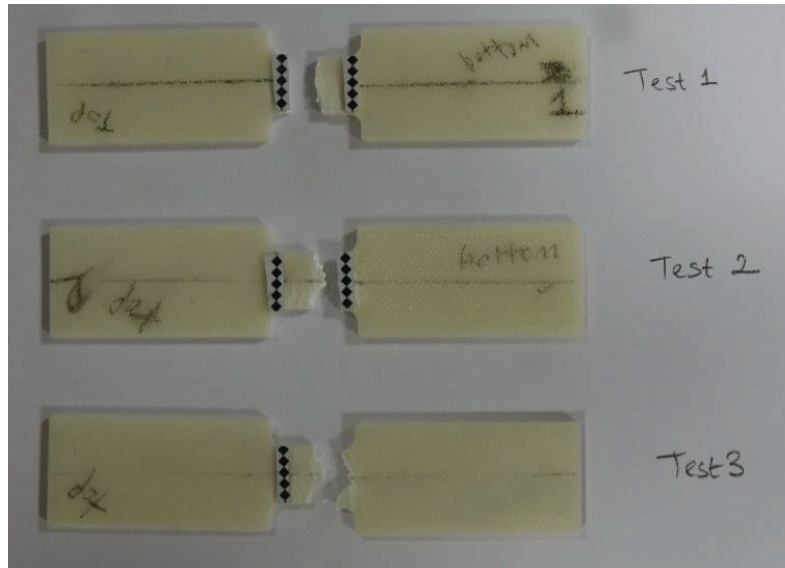


Figure 4.3. Custom Type specimens after quasi-static tensile test.

Finally, Type IV specimen, which is suitable for non-rigid plastics, was used for static tensile characterization. The failure of specimens occurred in gauge length region as indicated in Figure 4.4. Since the desired failure behavior is met with the repeated tests for each strain rate, the results obtained from Type IV specimen were used. The crosshead speed was arranged to 1.5, 15 and 150 mm/min to perform the tests between the $10^{-3}/s$ and $10^{-1}/s$ strain rates. In Figure 4.5, the average tensile stress-strain graphs are shown for three different strain rate values. For $10^{-3}/s$ strain rate, the strength at yield and break was measured as 28 MPa and 27 MPa, respectively, which well-agreed with the literature (Kerekes et al., 2019; Kanu, 2016). The percent elongation at yield was measured as approximately 3.5%. The elastic modulus values were calculated as 0.8, 1.1 and 1.2GPa for the 1.5, 15 and 150 mm/min cross head speeds, respectively. These results are consistent with other study in the literature (Owolabi et al., 2016). For the lowest strain rate, failure occurred gradually. However, since the material is strain rate dependent, the failure strain values decreased as strain rate increased and the material exhibited more brittle behavior. Furthermore, the results showed that the failure strain of polymers is directly related with the strain rate value (Siviour et al., 2006).



Figure 4.4. Type IV specimens after quasi-static tensile test.

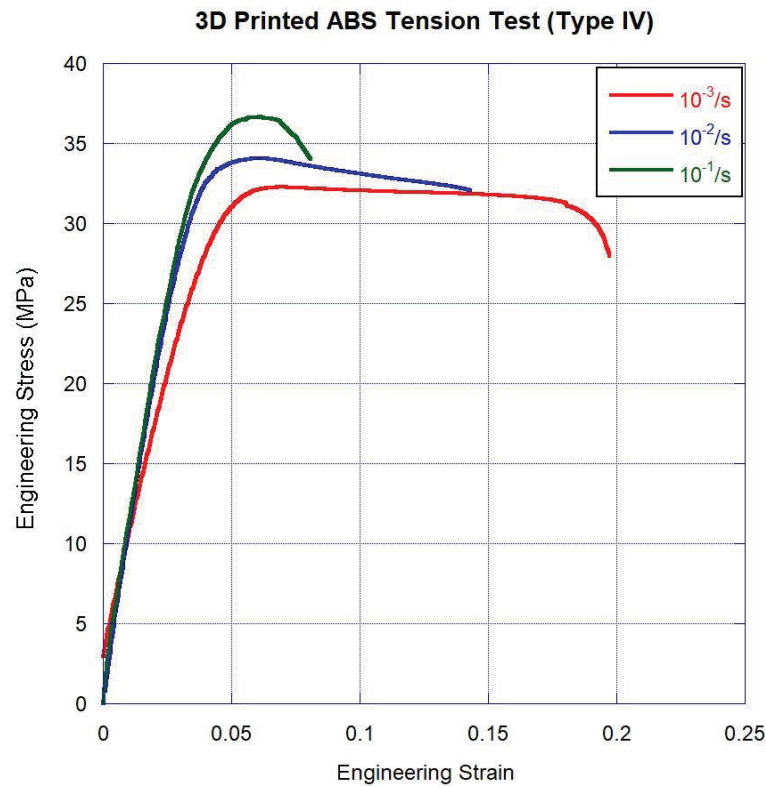


Figure 4.5. Quasi-static tensile stress-strain curves of 3-D printed Type IV tensile specimens.

The quasi-static tensile test results for three different types of specimens were compared in Figure 4.6. The gauge-length and width of specimen was found to play an important role in characterization studies due to anisotropy in the macroscale (raster and build orientation). Type IV specimen stress-strain curve was found to be very close to those reported in the literature. Since failure strain is directly related to operation parameters, it is possible to encounter very different yield and failure stress values in the literature. As the build orientation and raster type/angle are different in each study, a comparison was made with the studies which has the same operation parameters to obtain accurate results. Besides, care was taken to ensure that the tests are repeatable by means of precision. Therefore, Type IV was used in numerical analysis in order to determine failure criteria (erosion parameters) of bio-inspired core structures.

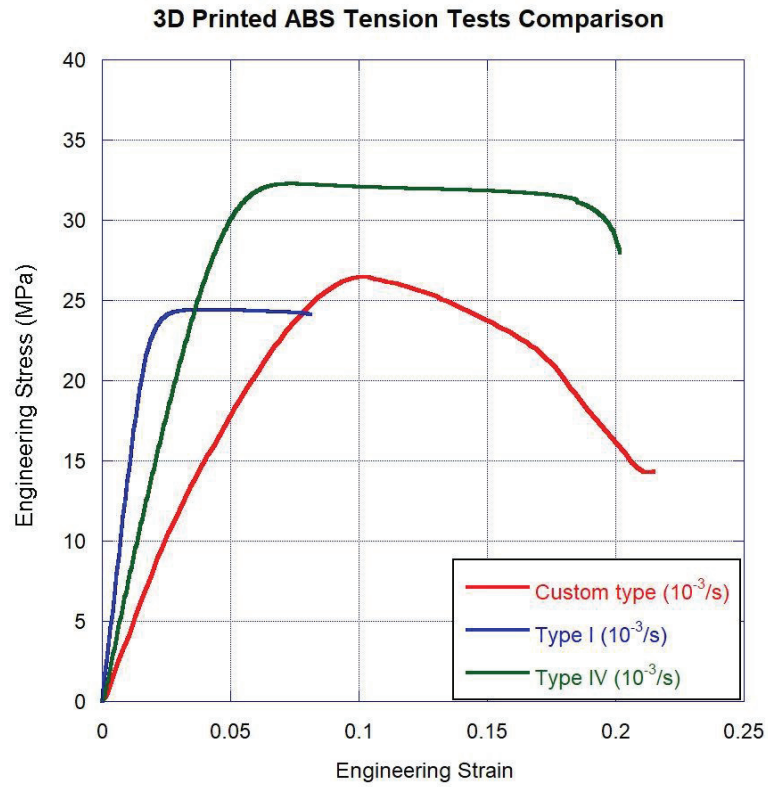


Figure 4.6. Comparison of quasi-static tensile stress-strain curves for different shape tension specimens.

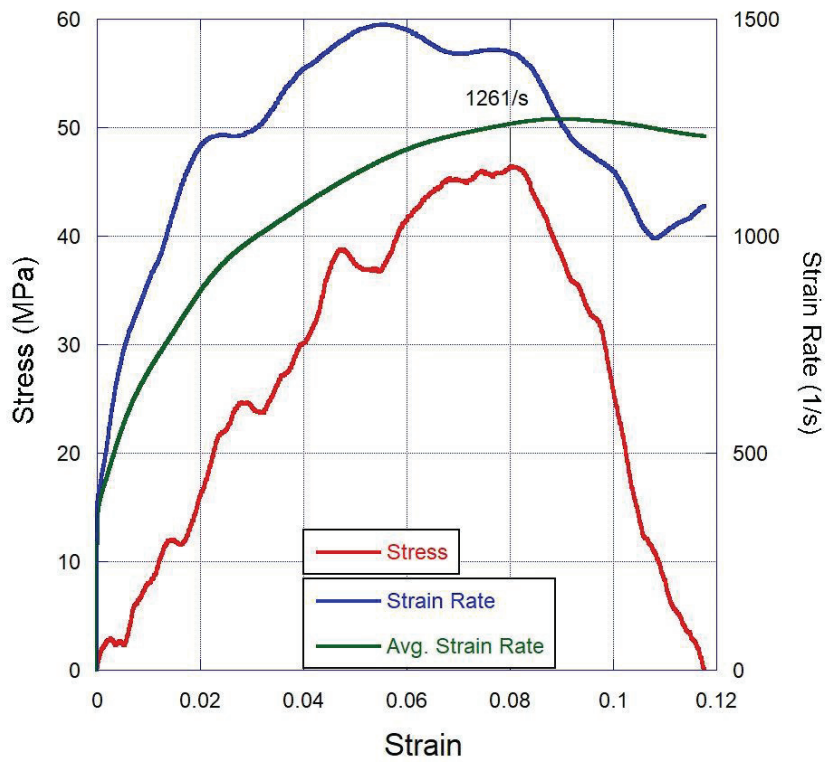


Figure 4.7. Dynamic tension stress-strain curve of 3-D printed ABS.

For dynamic tensile mechanical characterization of 3D printed ABS, custom specimen was used and SHTB tests were performed. The dynamic mechanical behavior of the specimen is indicated in Figure 4.7. The specimen failed at 0.08 strain at the average strain rate of 1261/s and tensile strength at failure was measured as 46.5 MPa.

The deformation history obtained from high speed camera is shown in Figure 4.8. The first image demonstrates the initial time 0. The specimen is starting to be exposed to the tensile load in the second image. First crack formation is shown in the third image and the following images indicate crack propagation and finally failure occurs at the last image which refers to 0.08 strain. The crack formation initiated perpendicular to the loading axis, and the crack proceeded parallel to the raster orientation of the 3D printer prior to fracture.

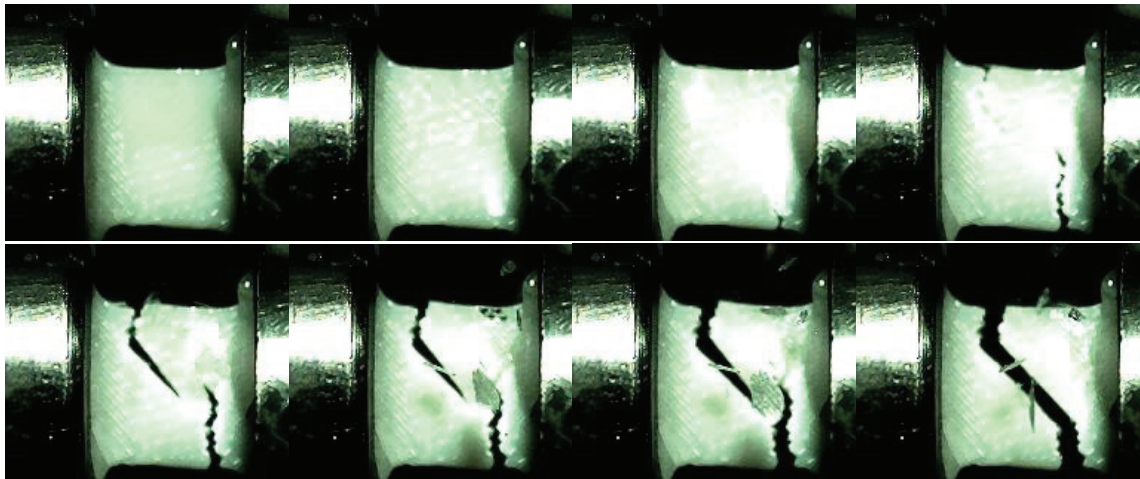


Figure 4.8. Deformation history of specimen under dynamic tension loads (SHTB).

As it can be seen in Figure 4.9, failure strain of ABS is directly related with the loading rate. In other words, final strain is inversely proportional to the strain rate (Siviour et al., 2006). Additionally, strain rate sensitivity increases when the loading rate is increased (Mulliken and Boyce, 2006). The yield strength increased by 17% when the strain rate raised from $10^{-3}/s$ to $10^{-1}/s$. The yield strength, on the other hand, reached to 46.5 MPa by 66% increment at an elevated loading rate of 1261/s. In brief, the yield strength is majorly affected by the applied strain rate.

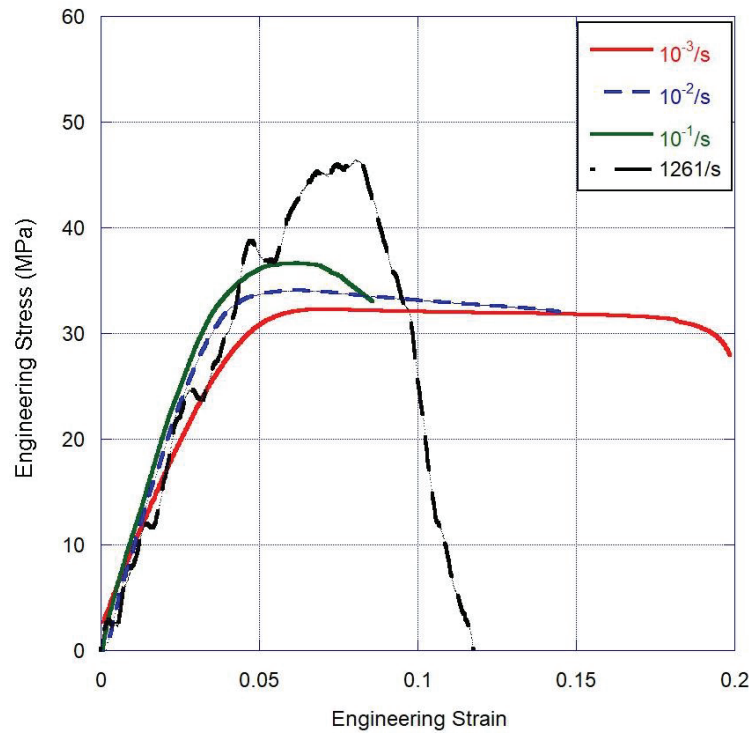


Figure 4.9. Comparison of quasi-static and dynamic tension stress-strain curves of 3-D printed tensile specimens.

Quasi-static compression stress-strain curves of 3-D printed ABS having 8mm diameter and height are shown in Figure 4.10. The crosshead speeds were arranged to 0.48, 4.8 and 48 mm/min, respectively.

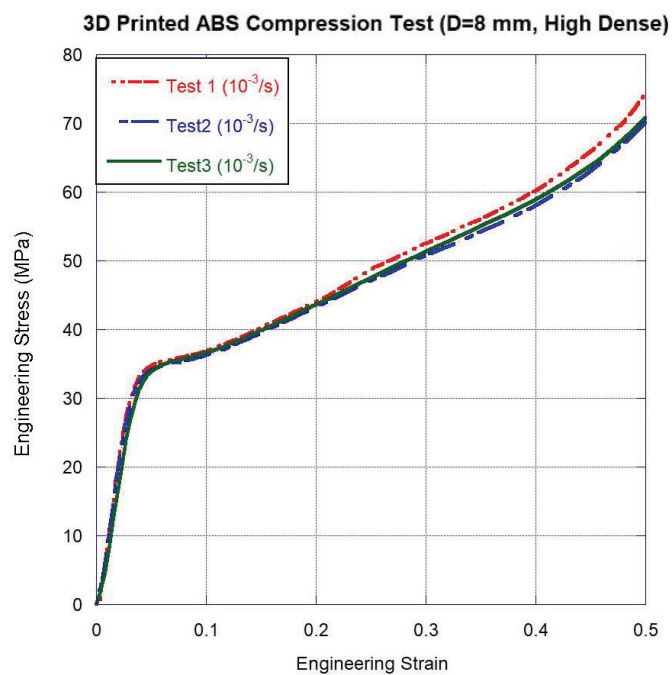


Figure 4.10. (cont.)

(cont. on next page)

3D Printed ABS Compression Test (D=8 mm, High Dense)

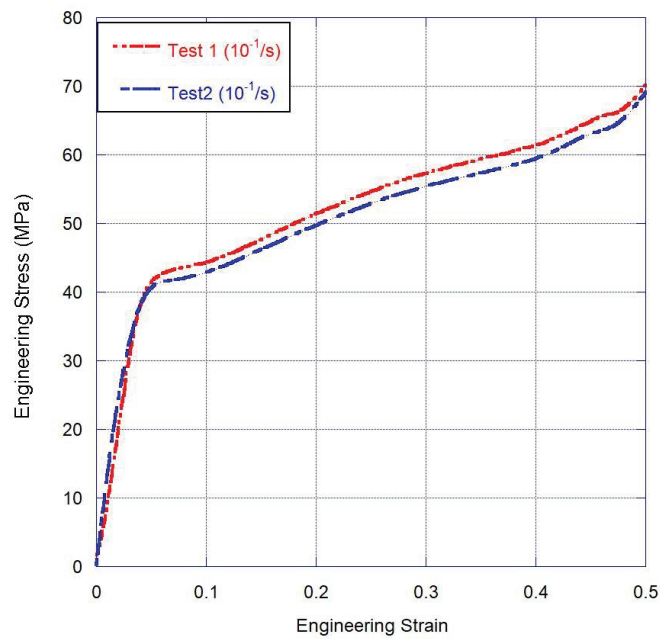
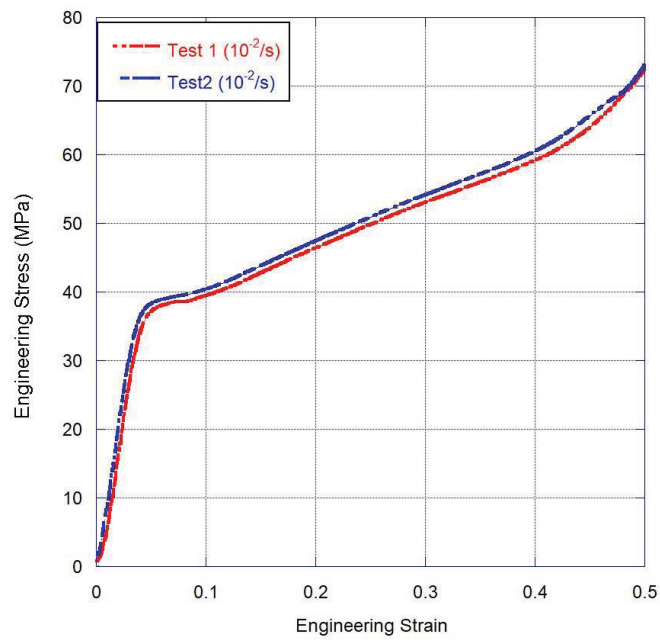


Figure 4.10. Quasi-static compression stress-strain curves of 3D printed specimen.

Figure 4.11 shows the comparison of the quasi-static compression curves between the $10^{-3}/s$ and $10^{-1}/s$ strain rates. The yield stresses were measured as 36.6, 38.6 and 43 MPa, respectively. As in the behaviour under tension loads, the material exhibited strain rate dependent behaviour under compression as well.

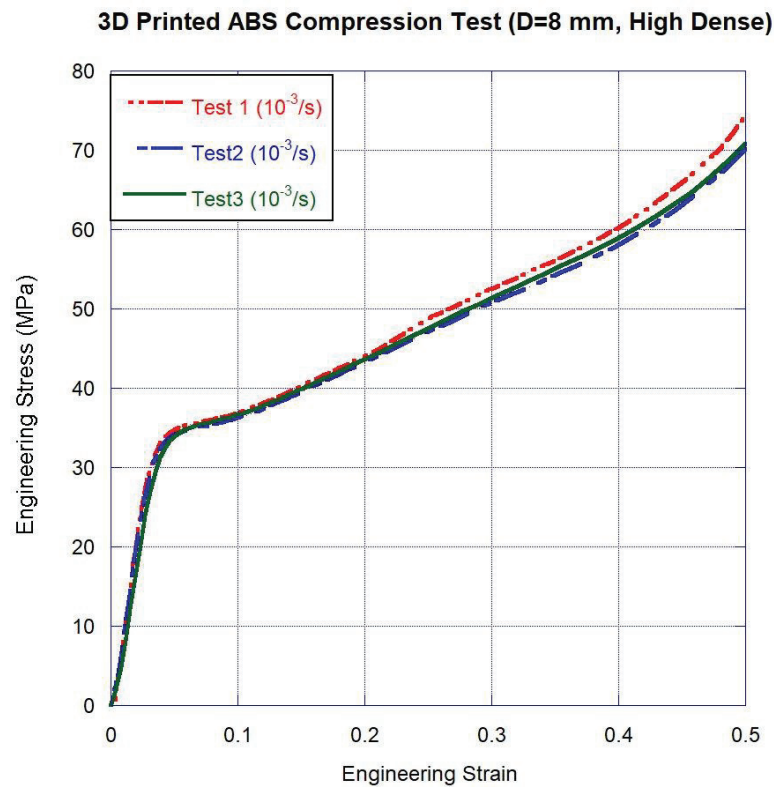


Figure 4.11. Comparison of quasi-static compression stress-strain curves of 3-D printed compression specimens.

Owolabi et al. conducted high strain compression tests for 3D printed ABS and concluded that the damage evolution became more profound when the strain rate exceeded 1000/s. At strain rates below this value, the specimen could be compressed up to maximum of 60% of its height and only buckling occurred instead of complete fracture. Therefore, it was aimed to exceed the strain rate of 1000/s in this study. For an average strain rate of 2500/s, the yield point and the maximum stress were found as 87.8 and 100 MPa, respectively. The measured values make sense when compared with the other tests in the literature conducted under the same operational conditions. As shown in dynamic test result of the specimen (Figure 4.12), there is an almost linear relation between the stress and the strain until the yield point (Owolabi et al., 2016).

Dynamic deformation history of ABS under compressive loads was recorded by a high-speed camera. As it can be seen in Figure 4.13, the fracture evolution started to become more drastic after exceeding the compression ratio 60%.

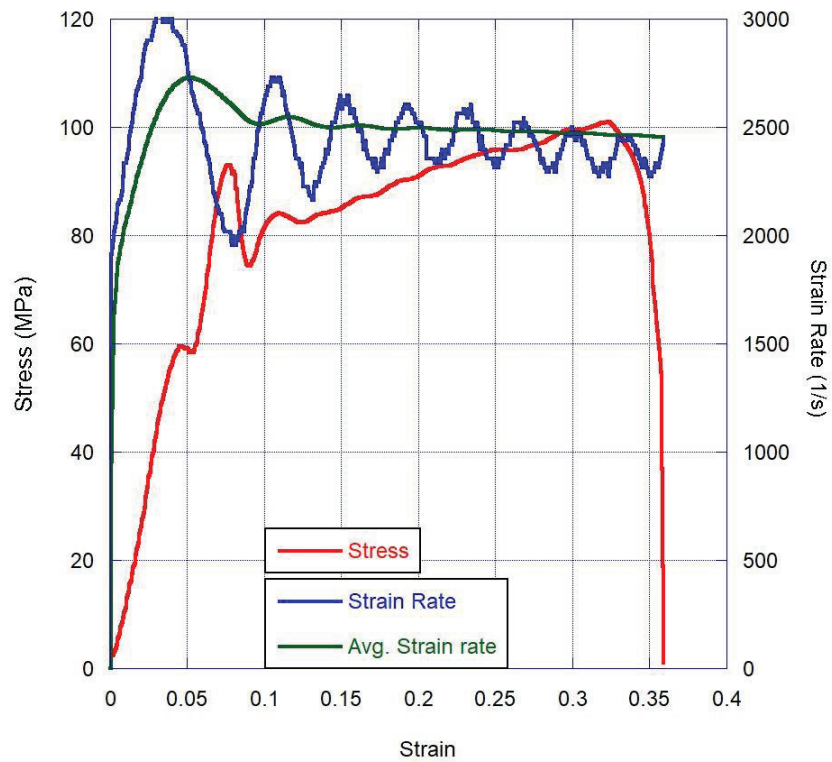


Figure 4.12. Dynamic compression stress-strain curve of 3-D printed ABS.

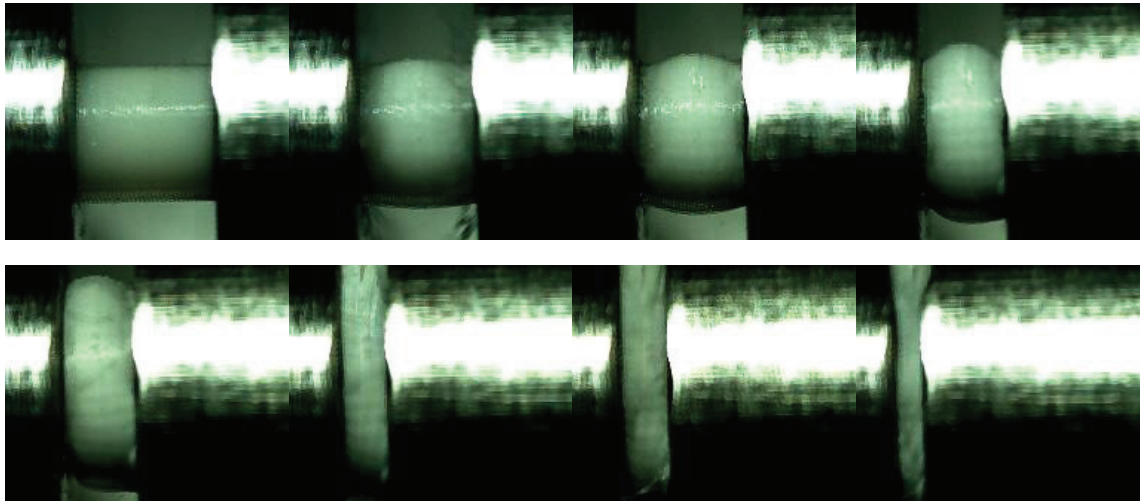


Figure 4.13. Deformation history of specimen under dynamic compressive loads (SHPB).

The compressive yield strength increases when strain rate is increased. Hence, the higher stress levels observed as strain rate increased (Figure 4.14). However, sudden increase in stress caused the specimen to fail at earlier strain levels.

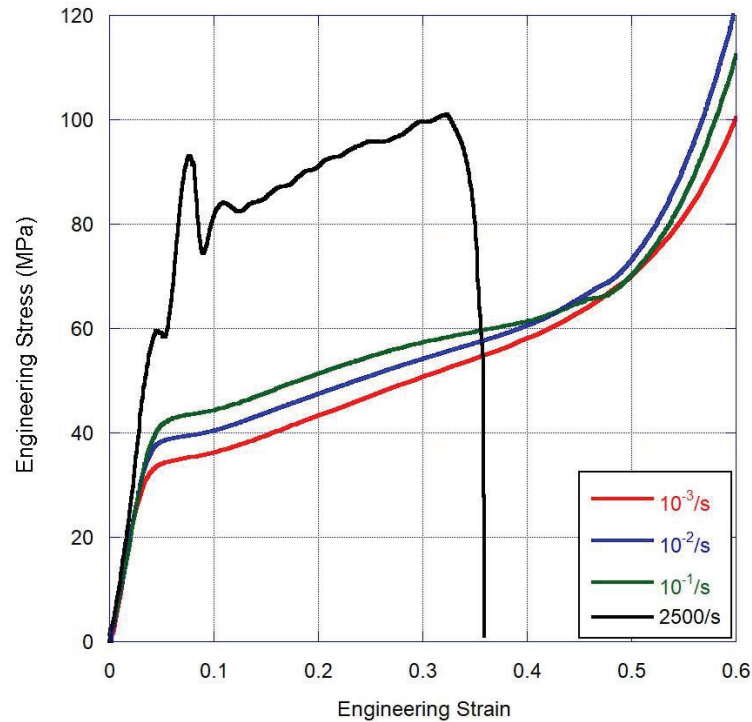


Figure 4.14. Comparison of quasi-static and dynamic compression stress-strain curves of 3-D printed compression specimens.

4.2. Fingerprint Core Crushing Behavior Results

Since the axial crushing behavior of the thin walled structures is almost 10 times higher than the that of horizontally crushed ones in terms of specific energy absorption (SEA or SAE), all crushing behavior studies were performed in axial direction (Baroutaji et al., 2017). First, three different fingerprint geometries were modeled to optimize the bio-inspired core structure. Then the final design (geometry) was decided by preliminary numerical analysis. Both experimental and numerical studies were performed simultaneously to investigate the energy absorption characteristics of the core by varying the geometrical parameters such as wall thickness and height.

Due to the design of the core, thickness could not be more than 1.5 mm. At the same time, the tolerance of 3-D printer did not allow the production of 0.5 mm thickness value. Therefore, samples of 20 and 30 mm in height and 1 and 1.5 mm in thickness were produced and their quasi-static crushing test results were compared (Figure 4.15). Also, dynamic compression analyses were performed numerically in Ls-dyna for heights of 20,

30 and 40 mm and thicknesses of 1.0 and 1.5 mm which were discussed in the following sections.

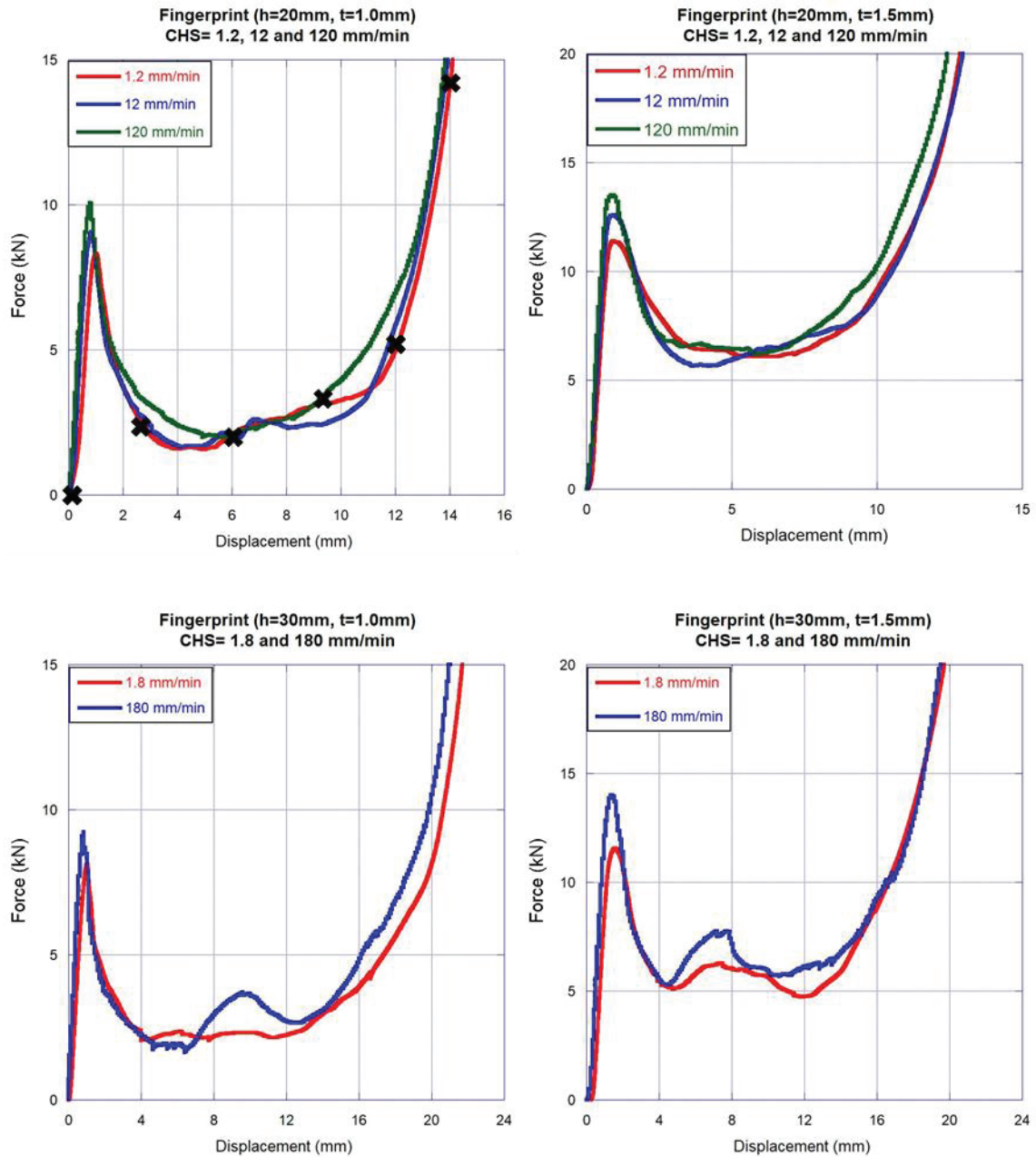


Figure 4.15. Quasi-static experimental force vs. displacement curves of fingerprint for varying height and thickness values.

The structures having 20mm height and, 1.0- and 1.5 mm thicknesses were tested statically. The crosshead speeds were arranged to 1.2, 12 and 120 mm/min to obtain desired strain rate levels. The other structures having 30mm height and 1.0- and 1.5 mm

thicknesses were tested as well. For this height value only 2 different crosshead speeds were chosen which were 1.8 and 180 mm/min. The quasi-static crushing behavior of fingerprint cores for varying height and thickness values are shown in Figure 4.16.

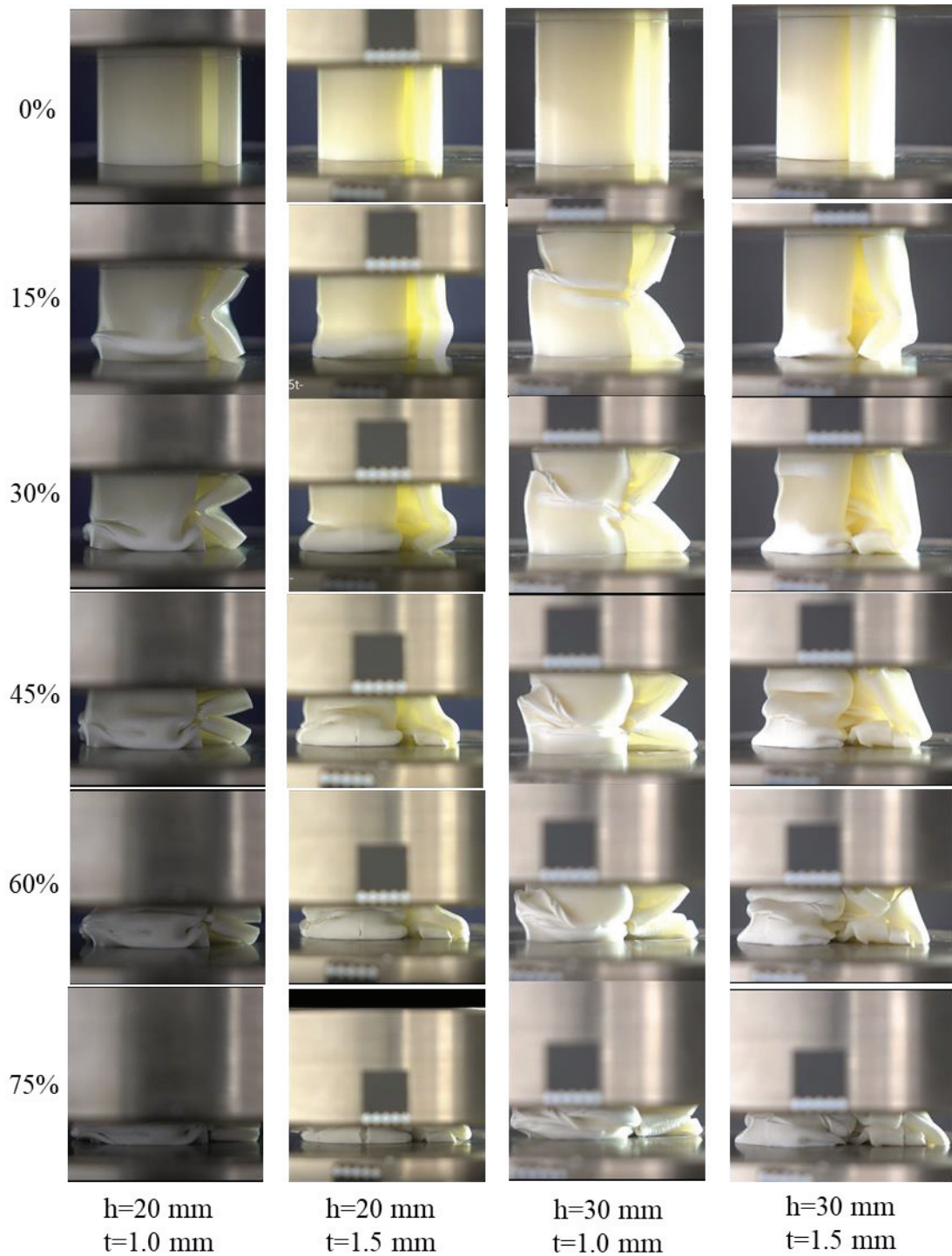


Figure 4.16. Comparison of quasi-static crushing behavior of fingerprint cores for varying height and thickness values.

Peak crushing force and specific absorbed energy values were compared in order to investigate the effect of height and thickness parameters of fingerprint geometry on energy absorption performance (Figure 4.17). The specific absorbed energy (SAE) versus displacement graph was obtained by dividing the area under the force-displacement graph by the mass of the fingerprint specimen by using Equation 4.1.

$$SAE = \frac{\int F(t)dx(t)}{m} \quad (4.1)$$

Where $F(t)$ and $x(t)$ refer to force and displacement with respect to time, respectively, and m refers to mass of the fingerprint sample. In all graphs it is obvious that the energy absorption capacity increases with the strain rate increment.

In Figure 4.17, peak force and SAE values for each height are summarized. Although the force values (peak and average) did not significantly change with the change in height value, the SAE was directly affected as can be seen clearly. SAE value decreased due to mass increase when height increased from 20 mm to 30 mm.

When the force-displacement graphs were investigated for each crosshead speeds, it was observed that the first peak force values increased with the strain rate increment. Therefore, the energy absorption capacity (SAE) of fingerprint core was improved by increasing quasi-static strain rate.

The maximum force values for the sample of 20 and 30 mm in height and 1 mm in thickness increased by approximately 25% with increase in strain rate. When the thickness was increased from 1 mm to 1.5 mm for the same heights, there was an increase in the maximum force value of about 35%. For 20 mm height, irrespective of the strain rate, the average force value increased by 60% when the thickness value was increased to 1.5 mm. On the other hand, for a thickness of 30 mm, the average force value increased by approximately 40% when the thickness value was increased to 1.5 mm, irrespective of the strain rate. For 20mm and 30mm heights, the highest SAE value was measured at 1.5 mm thickness. When the thickness was increased to 1.5mm for 20mm height, the SAE increased by 59%, while for the 30mm height, the SAE value increased 43% with the same thickness increment (Figure 4.17).

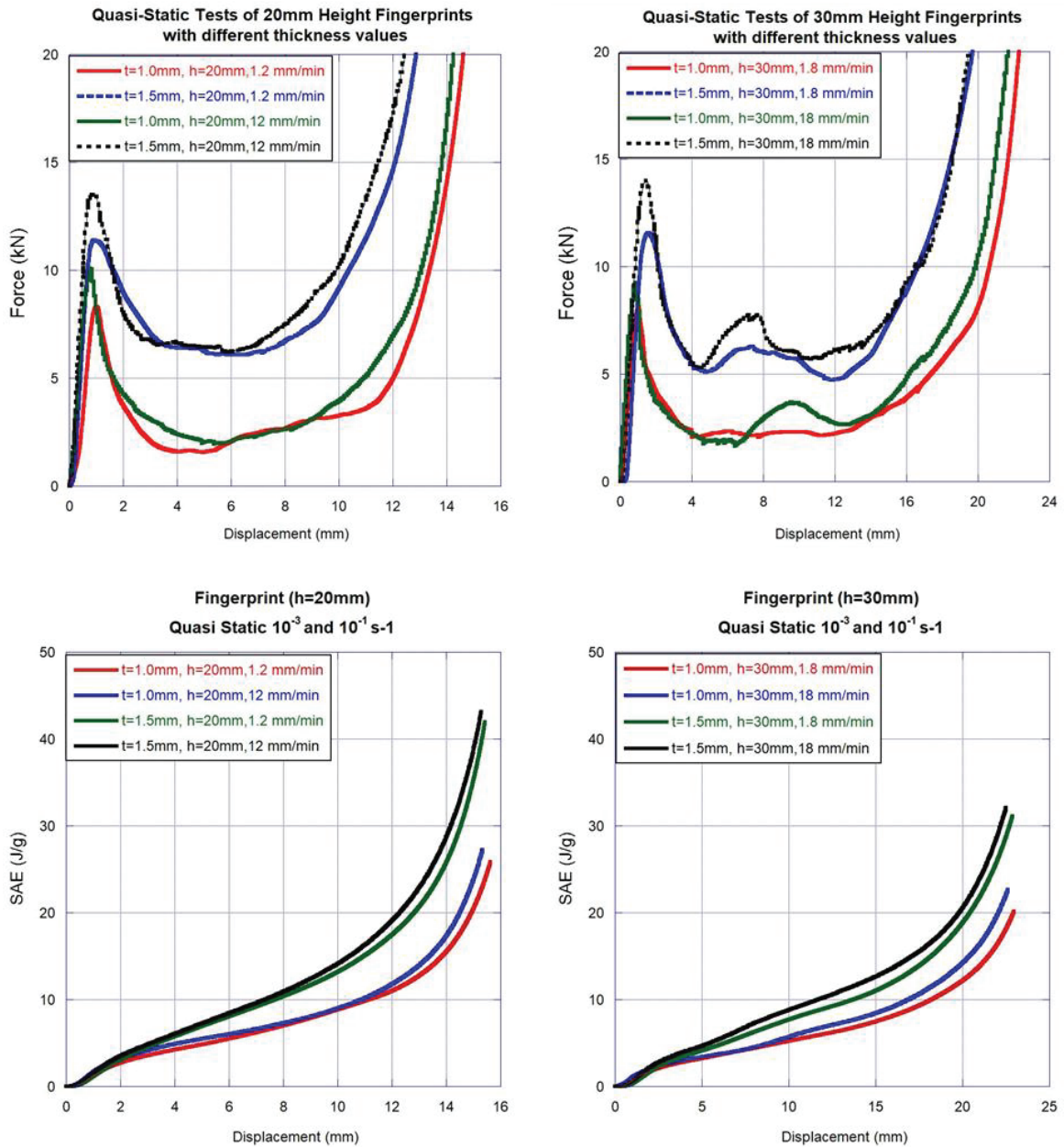


Figure 4.17. Quasi-static experimental force & SAE vs. displacement plots of fingerprint cores for varying height and thickness values.

All experimental results are summarized in Figure 4.18 as a histogram graph for the crosshead speeds corresponding to the minimum strain rate level. For 1mm thickness, the maximum force values at different heights were close to each other. When the thickness increased from 1 mm to 1.5 mm, the maximum force was measured approximately 11.5 kN in the sample with a height of 30mm. When SAE values were compared, SAE values of short samples being 20mm in height, were higher than long specimens when compared to each thickness value. The fact was arisen from increase in

mass upon increasing height of the specimen. However, the samples with higher mass could not compensate this mass increase in terms of crushing performance, so the SAE values were lower. Briefly, crushing performance did not improve despite the increase in mass. It was also observed that there was a direct correlation between SAE and thickness of the specimens. The highest SAE value, which was 43 J/g, was observed in the sample with a height of 20 mm and a thickness of 1.5 mm.

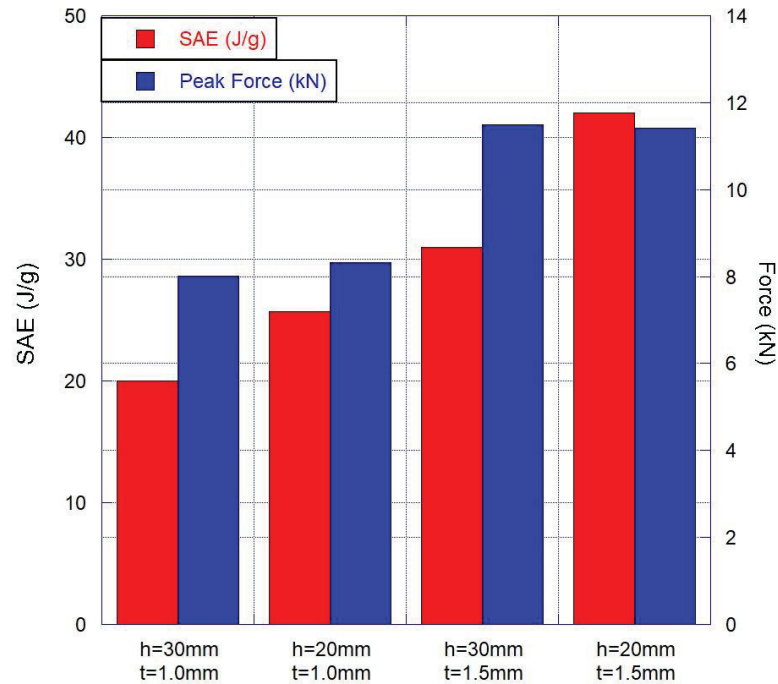


Figure 4.18. Quasi-static experimental SAE & Peak force vs. displacement values of fingerprint cores for varying height and thickness values.

Numerical analyzes were performed to observe the effect of the change of geometric parameters on the energy absorption capacity under dynamic loads. Samples with heights of 20, 30 and 40 mm and thicknesses of 1.0 and 1.5 mm were crushed at a speed of 10 m/s. The specimens were crushed under the same conditions without activating failure parameters in order to reduce computational cost. Figure 4.19 shows the force vs. % displacement for six different fingerprint structures. As shown in both graphs, the thickness has the highest impact on the force value and consequently on the energy absorption capacity. It should be noted that the thickness has a significant effect on the energy absorption performance of the core structure. As it can be seen in Figure 4.20 having thickness of 1 mm specimens were subjected to global bending. The increase in

thickness provided higher global bending resistance and higher contribution to the impact energy absorption of the structure, thus, the specimens having 1.5 mm thickness exhibited more energy absorption capacity.

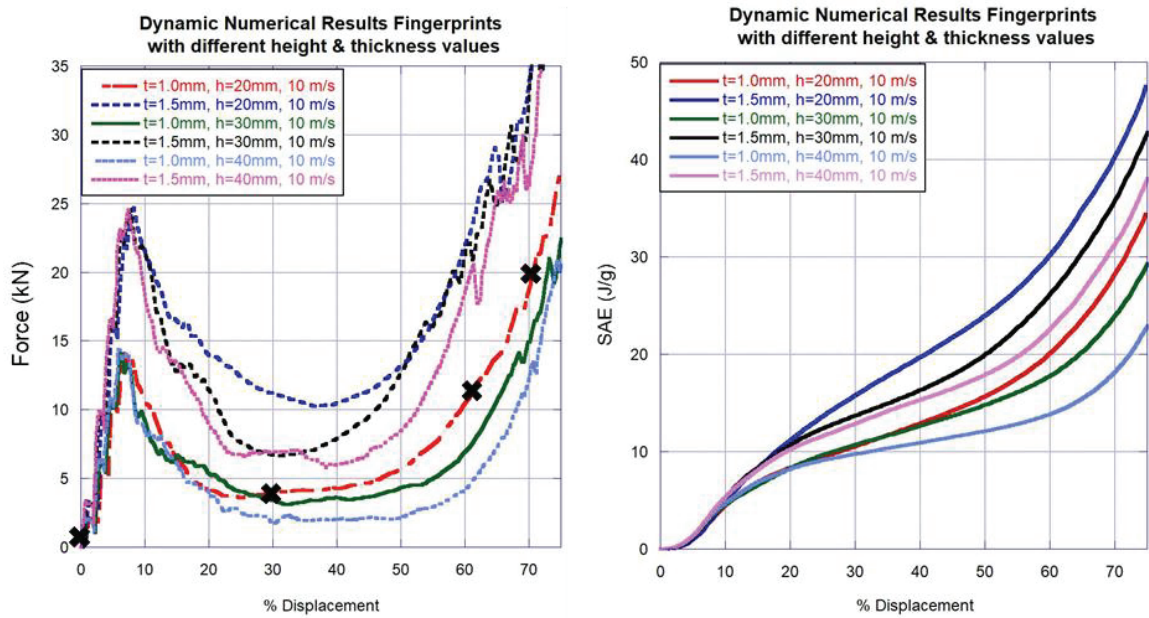


Figure 4.19. Dynamic numerical force & SAE vs. % displacement curves of fingerprint cores for varying height and thickness values

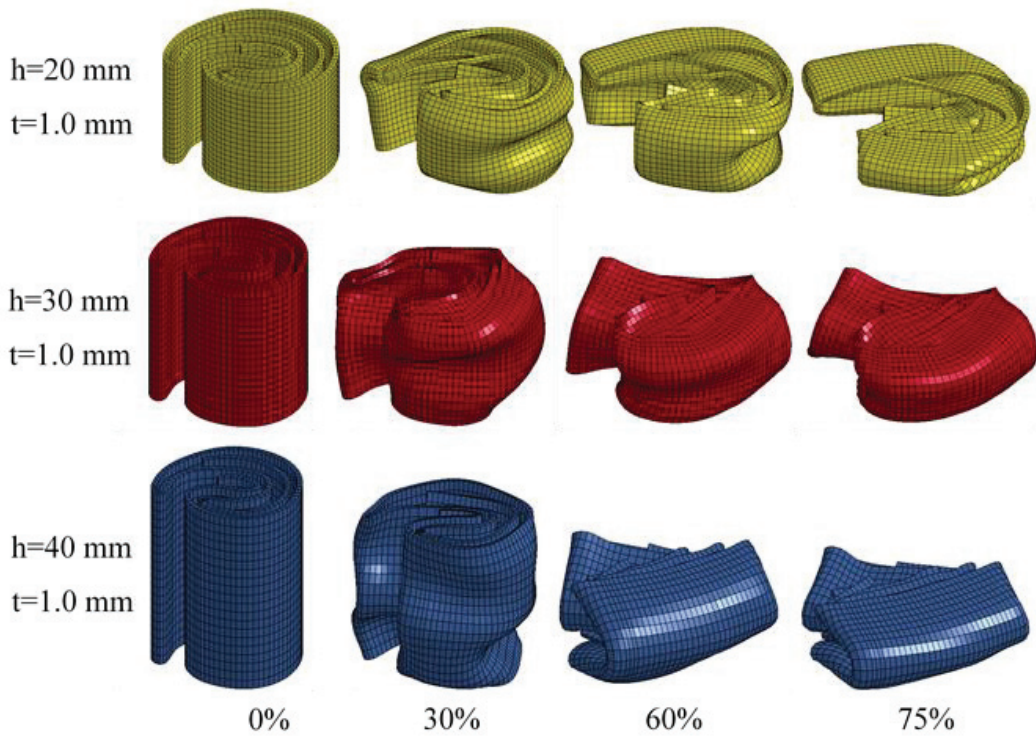


Figure 4.20. Comparison of dynamic numerical crushing behavior of fingerprint cores for varying height and thickness values.

Moreover, since the strain rate is the ratio obtained by the dividing of the crosshead velocity (impact velocity) to the length of the structure, short specimens (20mm) were exposed to a higher strain rates when the velocity is the same. Therefore, short specimens showed better mechanical performance resulting in better energy absorption capability. In long tubes, on the other hand, which were 30 mm and 40 mm in height, Euler type buckling, and global bending occurred. Therefore, due to buckling during the crushing instead of fold formation, the energy absorption capacities were less than that of 20 mm height ones. In other words, the global buckling negatively affected the energy absorption capacity especially at increased heights and lower thickness values. This phenomenon limits the further energy absorption capacity of the structure. Similar conclusion is made by other researchers (Cetin and Baykasoğlu, 2019).

It is obvious that the proper selection of the geometrical parameters of the structure is highly critical in order to optimize the energy absorption capacity and efficiency of the structure. As a result of the experimentally performed quasi-static analysis and numerically modeled dynamic analysis, fingerprint specimen with a height of 20 mm and a thickness of 1.5 mm was superior in terms of energy absorption. Therefore, in the subsequent crushing studies, samples with this geometric dimension was used.

After completing the parametric study of fingerprint geometry, the fingerprint was compared with the other conventional structures (square, cylinder and honeycomb). Thickness value, as was also seen in the parametric studies of fingerprints, directly affects the energy absorption capacity. Besides, the increase in height causes global buckling and bending rather than fold formation resulting in better crushing performance. For these two reasons, the thickness and height of the geometries were kept constant as 1.5 mm and 20 mm, respectively.

For this purpose, comparisons were made in two parts. These are as follows:

- 1- Same height, same thickness, and same mass, but different diameters resulting in different areal densities.
- 2- Same height, same thickness, same mass and same diameter, resulting in the same areal density.

The first part of the investigation was performed experimentally at quasi-static strain rates. The second part, on the other hand, was numerically analyzed.

For the first comparison criterion, since fingerprint geometry is a spiral-like structure, other geometries should have a larger diameter to capture the same mass. Since the thickness to diameter ratio corresponds to a value of about 0.03-0.0375 which is too small, they could not exhibit exponential crushing behavior as can be seen in Figure 4.21.

The peak, generally maximum, crushing force is concerned primarily, because it is the most influencing parameter in terms of the energy-absorption capacity of these structures under axial loading. The ideal peak crushing force should not be too much and should be close to the mean force, however, the difference between these two force values is very high when compared to the geometries other than fingerprint.

As shown in Figure 4.21, other conventional structures have remained almost 4.5 times lower in terms of average force value compared to fingerprint. There was also a approximately 6 times difference between the maximum and mean force values. This difference was calculated as around 1.6 in fingerprint geometry.

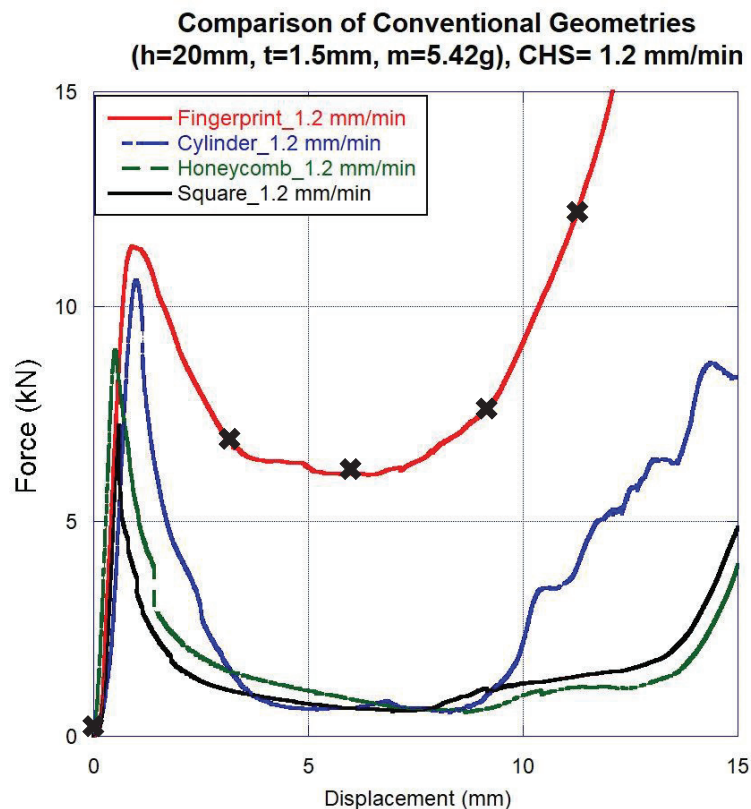


Figure 4.21. Quasi-static experimental force vs. displacement curves of fingerprint and conventional geometries (case:1, for different diameters).

The deformation histories of fingerprint and conventional geometries for the determined points in the force-displacement graph is shown in Figure 4.22.

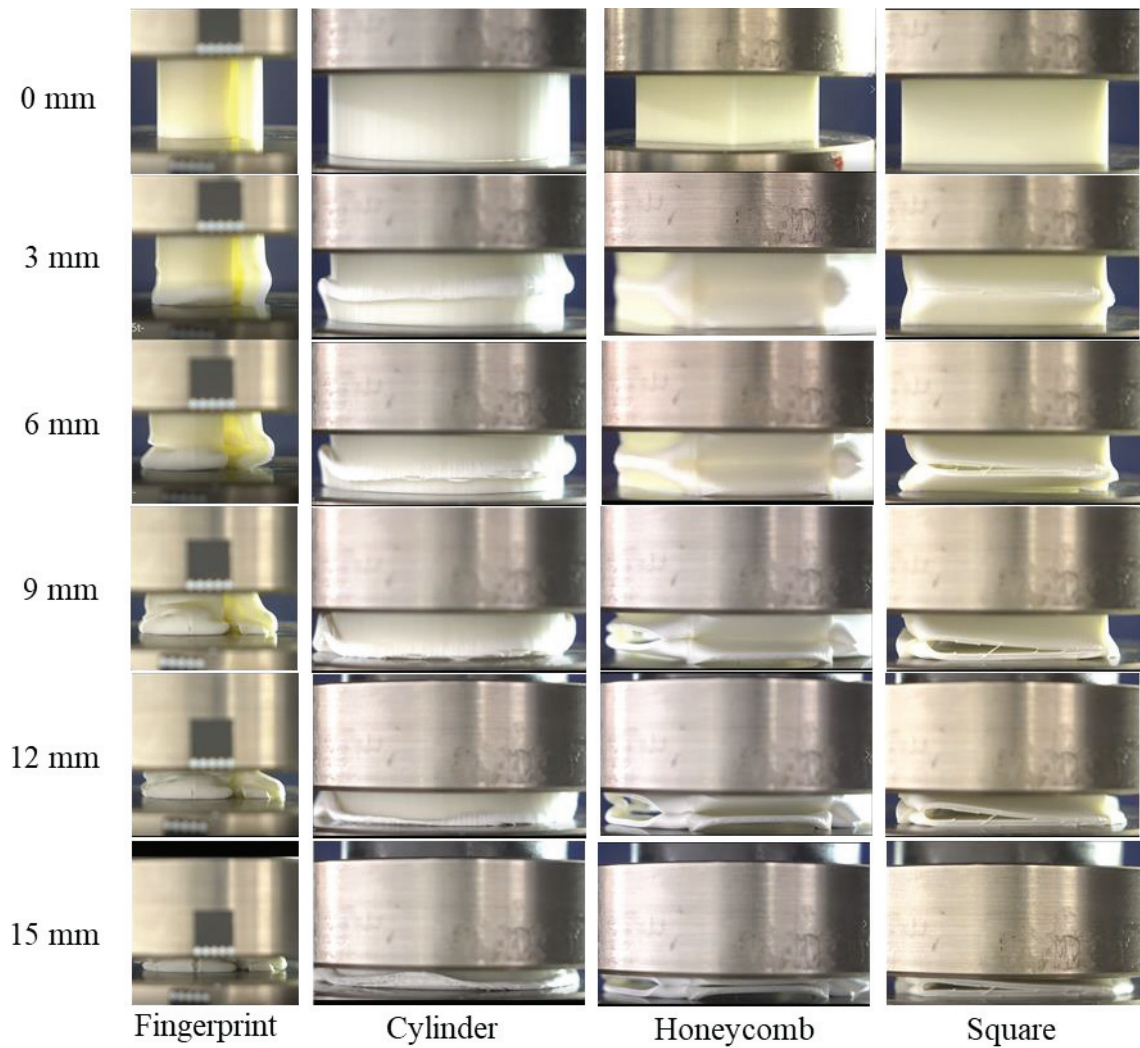


Figure 4.22. Comparison of quasi-static crushing behavior of fingerprint and conventional geometries (cylinder, honeycomb and square) (for different diameters).

Fully crushed views of conventional structures after the quasi-static axial crush test are shown in Figure 4.23.



Figure 4.23. Fully-crushed views of conventional structures (square, cylinder and honeycomb) after the quasi-static compression test.

Comparison of fingerprint and conventional geometries in terms of crashworthiness parameters (SAE and peak force) are demonstrated in Figure 4.24 as a histogram graph. In the square and honeycomb structures, early damage prevented the structures to absorb further energy. Therefore, they showed the lowest SAE values. On the other hand, since the mean force and maximum force values were close to each other in the fingerprint structure, SAE value increased through the densification. The reason of having weaker mechanical performance of other conventional structures was that they had larger diameters to achieve the same mass value as the fingerprint. As a result of larger diameters and relatively thin thickness, D/t ratios (~ 30 - 33) were relatively large (Lu and Yu, 2003) and resulting in an adverse effect on the crushing behavior.

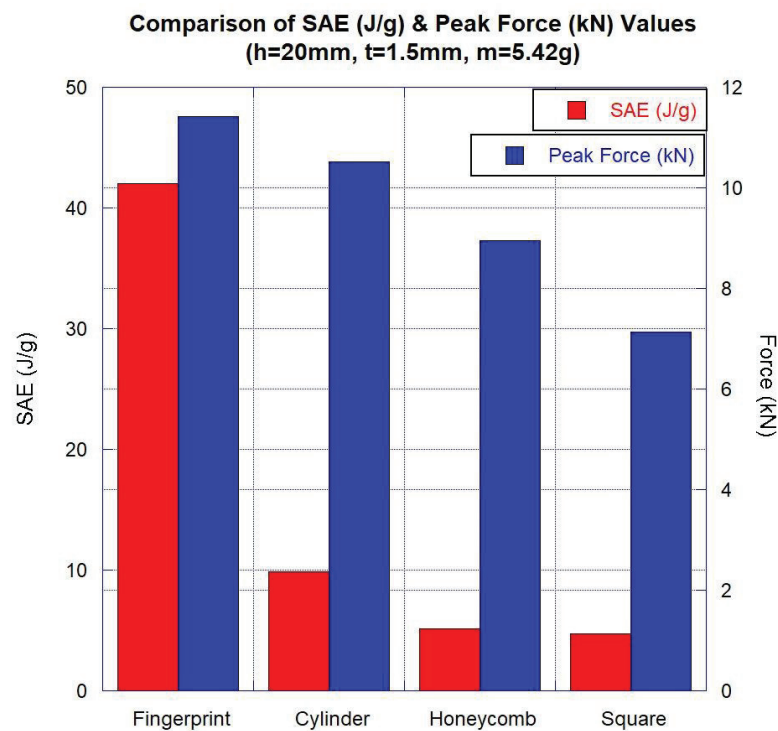


Figure 4.24. Quasi-static experimental SAE & Peak force vs. displacement values of fingerprint and conventional geometries (case:1, for different diameters).

For the second criterion, in order to obtain the same areal density, smaller structural forms of each geometry were added to inside of each of them. Therefore, by adding smaller structures, nested structures were created. The aim was to be able to establish similarity between the fingerprint and the other conventional structures in terms of mimicking self-contact formation during axial crushing.

Figure 4.25 shows the comparison of conventional structures and fingerprint geometry by means of peak force and SAE value according to second criterion which is same areal density. The maximum force values for the honeycomb, cylinder and fingerprint geometry were measured as approximately 25 kN. The peak force of square, on the other hand, was found as 22.5 kN. In nested geometries, the densification could not be observed because global bending appeared in the outermost geometry rather than fold formation. This resulted in a decrease in average force value at higher deformation levels. Thus, the SAE value of the fingerprint geometry was measured 1.45 times greater than the that of cylinder and the honeycomb at densification point which was approximately 13-14 mm. The deformation histories of numerically crushed fingerprint and conventional structures are shown in Figure 4.26.

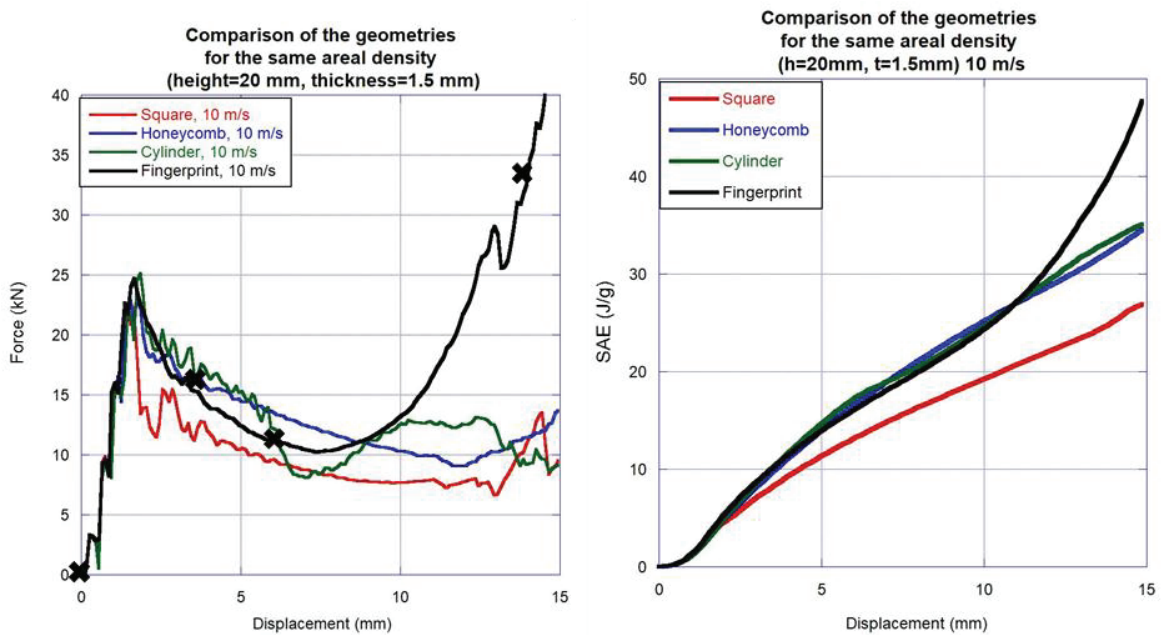


Figure 4.25. Dynamic numerical force & SAE vs. displacement curves of fingerprint and conventional geometries (case:2, for same areal density).

The comparison of the fingerprint and conventional structures (cylinder, honeycomb and square) in terms of two parameters (for different diameters and for same areal density) revealed that the unique geometry of the fingerprint allowed the coils to interact with each other (formation of local contact regions) while crushing and offered better mechanical performance.

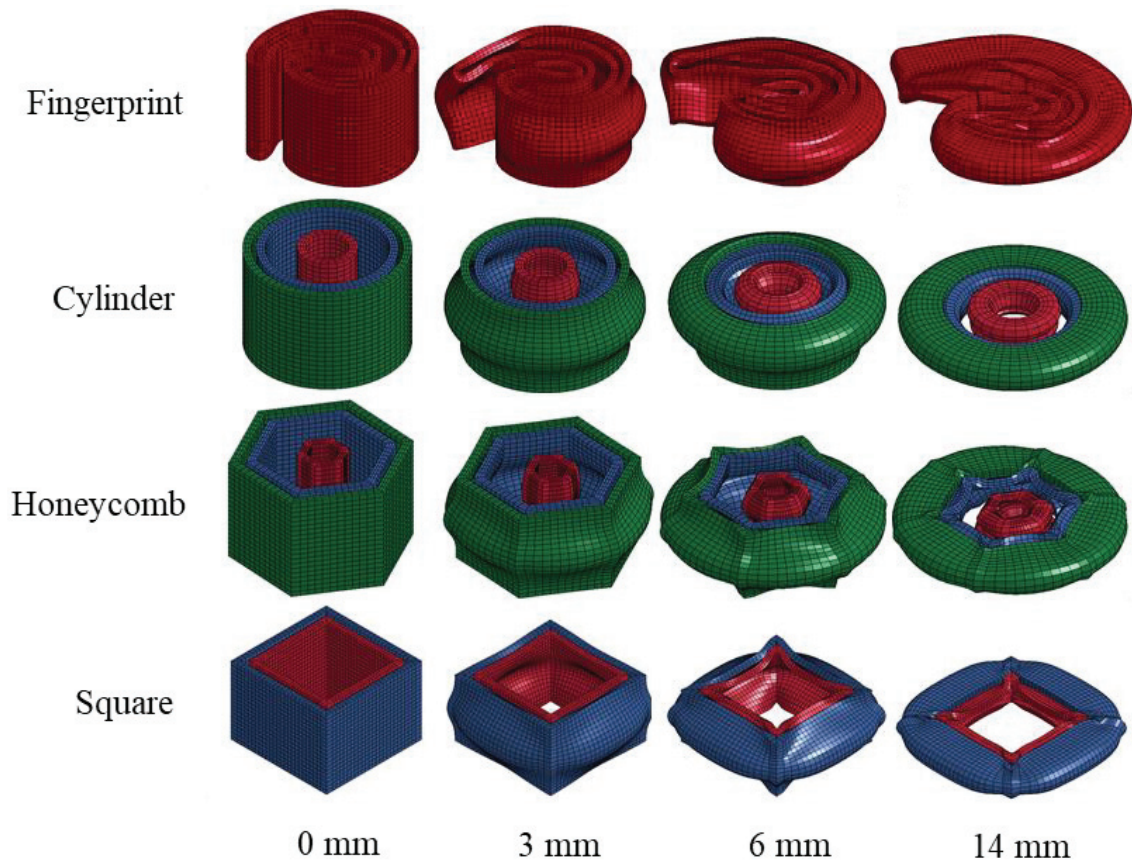


Figure 4.26. Comparison of dynamic numerical crushing behavior of fingerprint and conventional geometries (cylinder, honeycomb and square) (for same areal density).

After demonstrating the superior properties of fingerprint geometry, static and dynamic crushing behavior studies on fingerprinting (for 20 mm height and 1.5 mm thickness) was carried out to gain deep knowledge about the behavior of the structure. The investigation of crushing behavior of the geometries started with quasi-static crushing tests. Shimadzu AG-X universal compression test machine was used with arranged cross head speeds ranging between 1.2 to 120 mm/min. Test results were plotted for each crosshead speed as shown in Figure 4.27.

Figure 4.27 obviously shows that the force increased linearly when the specimen initiated to deform, and the first fold formation occurred. First fold formation is seen as a first peak in the force-displacement curves. As the deformation proceeded, first damage occurred and then the crushing force decreased rapidly. The fold formation of the outer wall was not observed after this damage, while the inner walls were still crushed by the confinement effect of the outer walls. After the inner and outer wall contacts completed,

the specimen became fully compacted. Beyond 12 mm deformation, the densification region started, and the specimen showed no further deformation.

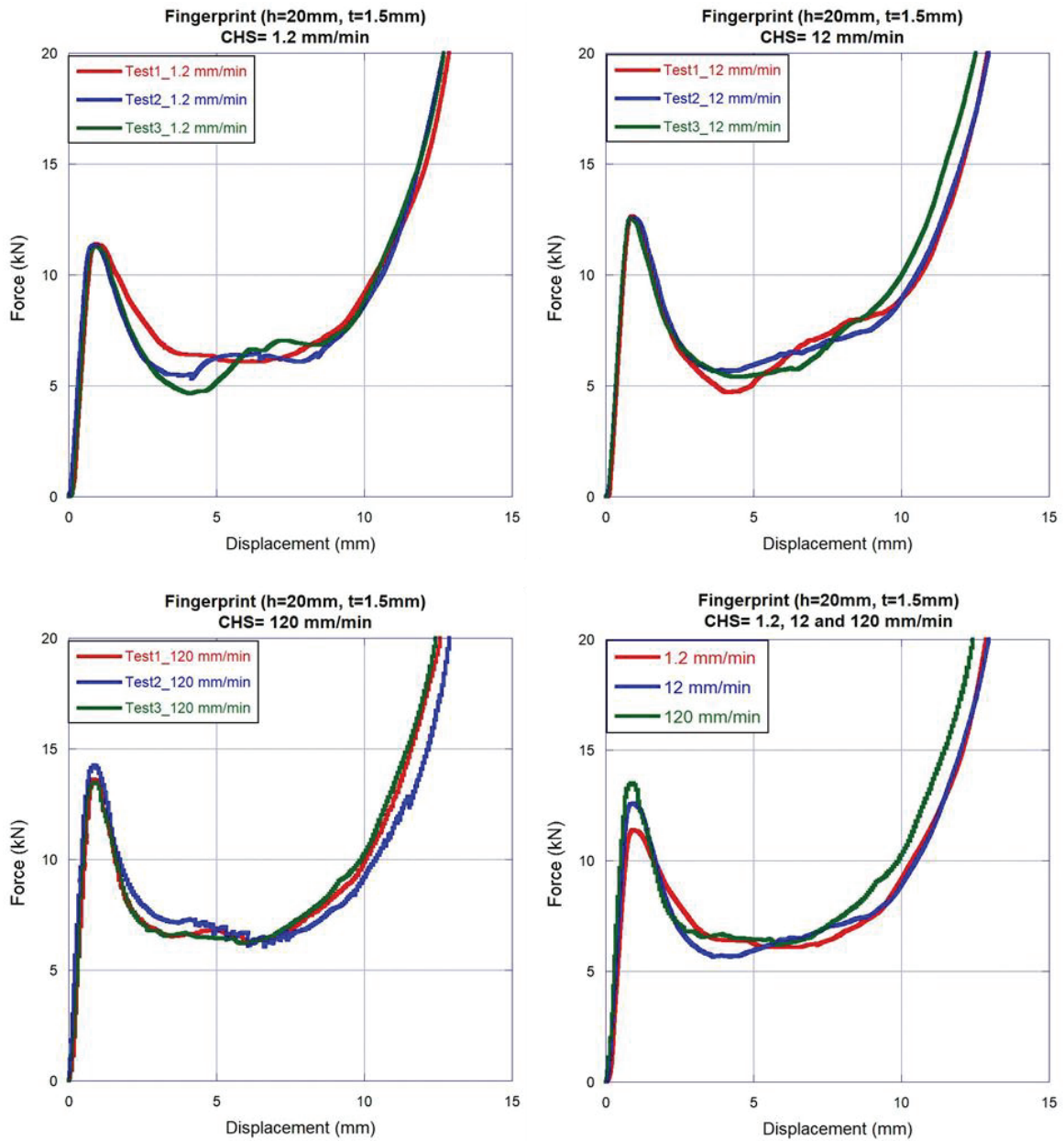


Figure 4.27. Quasi-static experimental force vs. displacement curves of fingerprint core for 1.2, 12 and 120 mm/min crosshead speeds.

Since the crashworthiness characteristics of the structures can be examined considering the force-displacement responses, SAE and peak crush force parameters are the indicators of crushing performance. The experimental results clearly show that the peak crushing force value of the fingerprint cores varies with the quasi-static strain rates.

This is expected because most of the thermoplastic materials exhibit strain-rate dependent behavior even under static conditions (Vincent et al., 2005; Hopmann et al., 2016). When the SAE values of the statically crushed fingerprint cores at 1.2 and 120 mm/min head speeds were compared, it was seen that there is a linear relation between them with respect to strain rate. In other words, the SAE value increased when the strain rate was increased. However, the experiment at 12 mm/min crosshead speed did not follow this rule. Although the initial peak force values increased linearly with increase in strain rate, the SAE value at this crosshead speed did not show the expected increase and remained below the values at 1.2 mm/min crosshead speed as shown in Figure 4.28. The mean force values, calculated for each test at 12 mm/min crosshead speed, were lower than the mean force values at other speeds. This is why the computed SAE values were less than the expected ones. Although the experiments were repeatable and consistent for each strain rate, it may be caused by the imperfections arisen from the manufacturing process. The tested samples selected for this strain rate may remain at the corner sides of the three-dimensional printer table during the manufacturing and therefore, their mechanical properties may have weakened due to manufacturing conditions. However, it could not be understood before the test because it is not possible to see these imperfections with the naked eye. In addition, it is not possible to estimate the presence and to measure the distribution of these imperfections in the specimens.

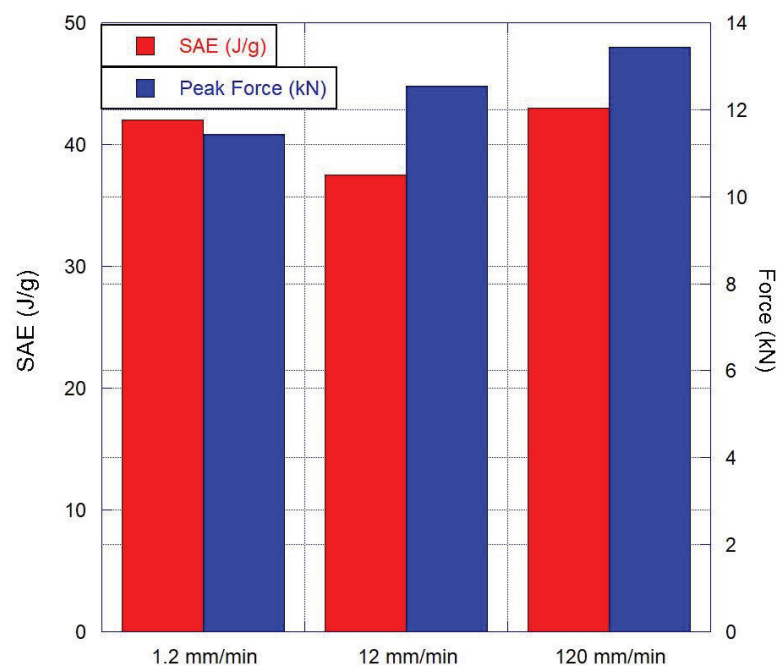


Figure 4.28. Quasi-static experimental SAE & Peak force vs. displacement values of fingerprint core for 1.2, 12 and 120 mm/min crosshead speeds.

The experimental deformation history for 1.2 mm/min cross head speed at various displacements is given in Figure 4.29. This crosshead speed corresponds to minimum quasi-static strain rate value and gives the basic idea of crushing behavior of the fingerprint core. When the deformation history and the top view of the fully deformed geometry are examined, it is seen that the cracks initiate and propagates between the layers due to additive manufacturing. These cracks also affect the folding behavior of the structure.

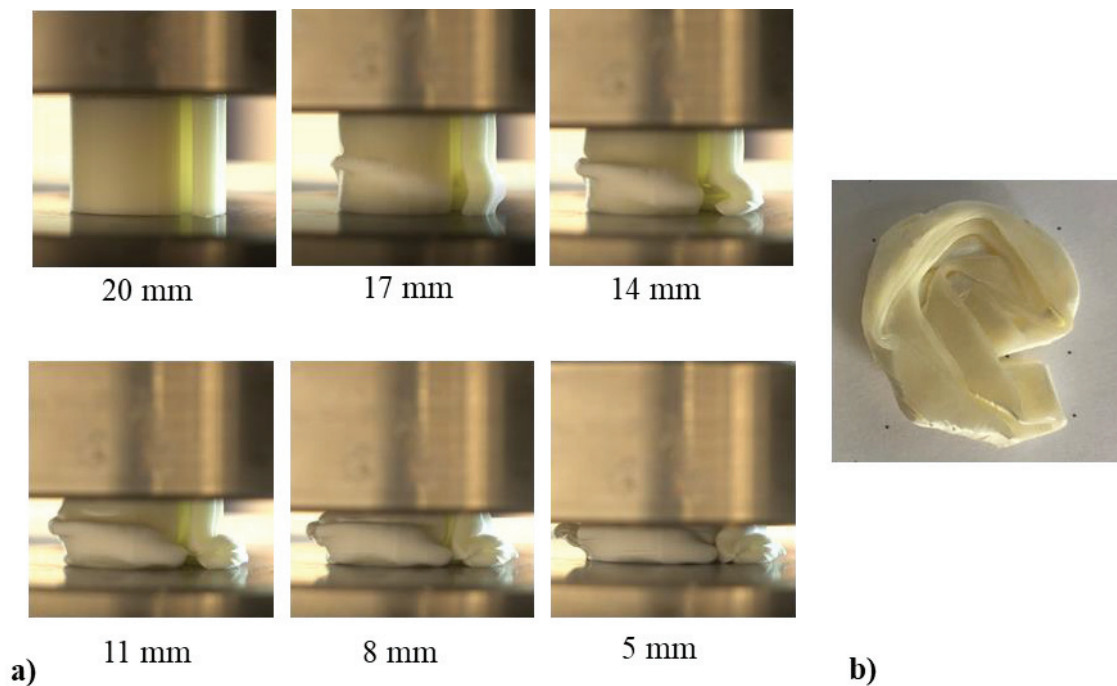


Figure 4.29. a) Deformation history of fingerprint core at 1.2 mm/min cross head speed, b) Final shape of fully crushed fingerprint geometry.

After examining the crushing behavior and evaluating the crushing parameters under quasi-static axial compression test, the crashworthiness characteristics at low to medium strain rates were examined using the drop-weight test set-up.

In the first drop weight test, the striker speed was measured as 2 m/s with 58 J kinetic energy, it was observed that the impact energy was not enough to crush at least 75% of the fingerprint core geometry. The structure was not completely crushed and hence, densification was not observed as shown in Figure 4.30. However, crack propagation and slippage of layers and separation of some of them was observed due to high deformation rate. For the impact velocity of 2m/s, the peak crushing force value was

calculated as 17.5 kN and the SAE value was 9.3 J/g. The deformation behavior will be explained in the following section with the numerical results.

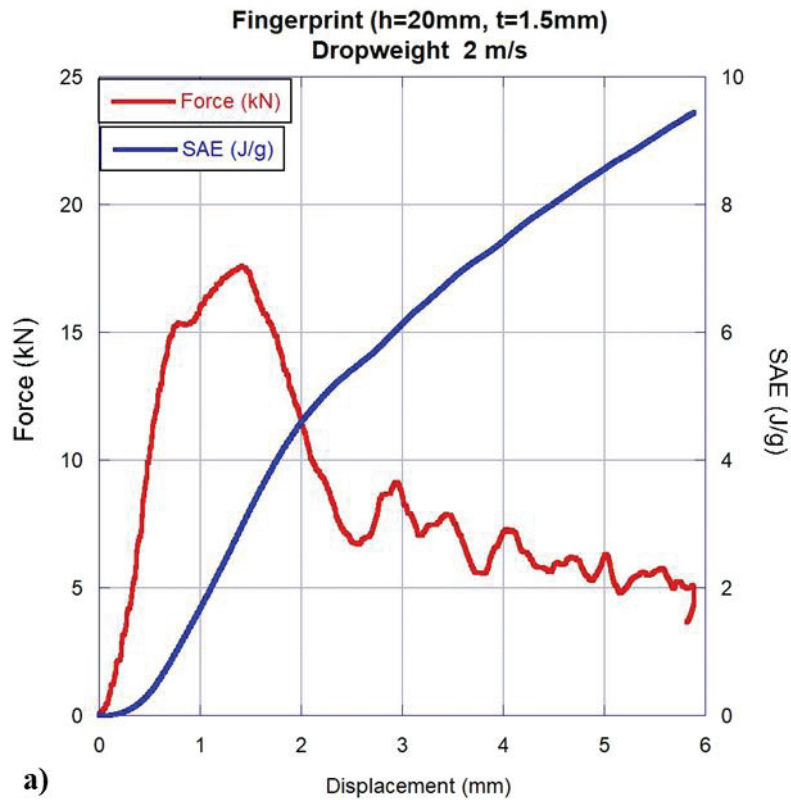
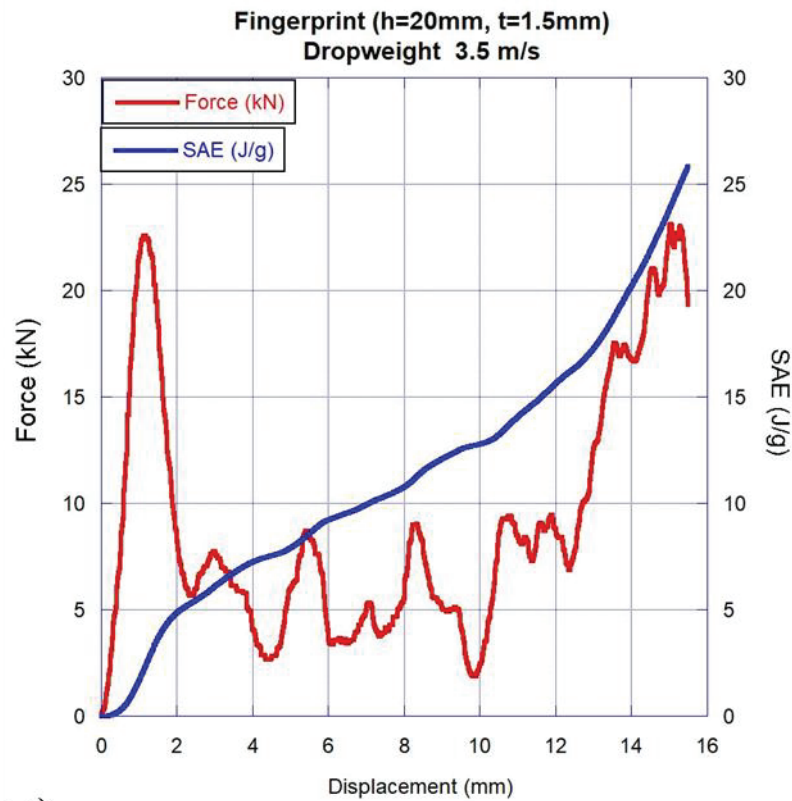


Figure 4.30. a) Dynamic experimental force & SAE vs. displacement curves of fingerprint core at 2 m/s impact velocity, b) Final shape of fully crushed fingerprint core.

For the other dynamic test, the striker speed was increased to 3.5 m/s with an 180J impact energy. At this speed the sample was crushed more than 80% of its height, as shown in Figure 4.31. For the impact velocity of 3.5 m/s, the peak crushing force value was calculated as 22.58 kN and the SAE value was 25.5 J/g. The history of crushing and damage will be explained in the following section with the results of numerical analysis.



a)



b)

Figure 4.31. a) Dynamic experimental force & SAE vs. displacement curves of fingerprint core at 3.5 m/s impact velocity, b) Final shape of fully crushed fingerprint core.

Figure 4.32 shows the energy absorption characteristics of core structure with height of 20 mm and thickness of 1.5 mm in terms of force-displacement curves at quasi-static and dynamic speeds. As can be seen from the figure, the initial peak force value is directly related with the deformation (strain) rate and increases as the strain rate increases. As the impact velocity increases (from 1.2 mm/min to 3.5 m/s), the peak force value becomes almost double, and the structure is immediately damaged in the first moments of impact and the energy absorption capability in the subsequent stages also reduces. When the dynamic force-displacement curve is examined, it is seen that the average of

the local maximum and minimum forces occurring after the peak force value is below the static curves. This is caused by the high deformation and damage upon dynamic loading.

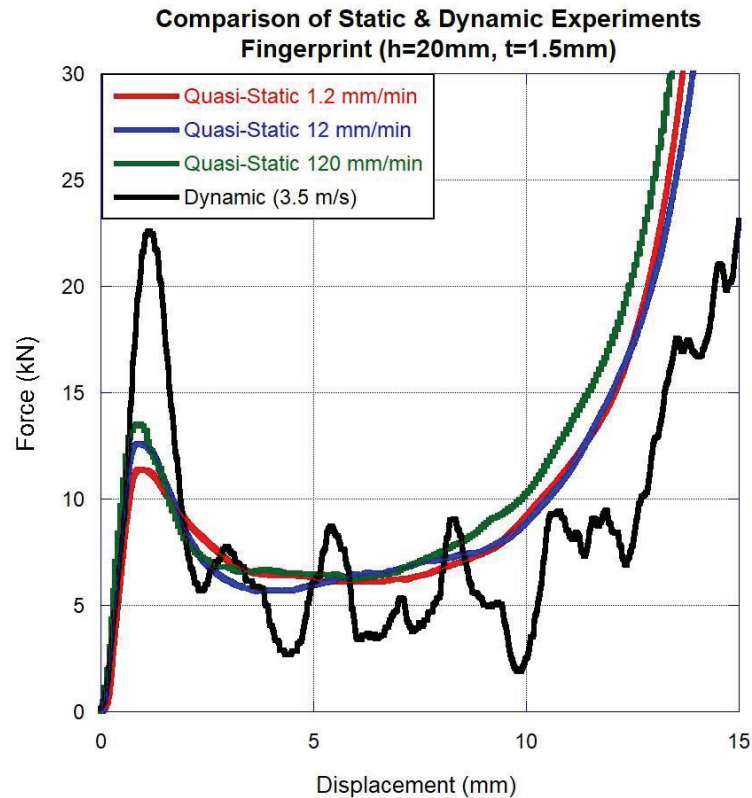


Figure 4.32. Force vs. displacement curves of fingerprint core under quasi-static and dynamic axial loads.

If the initial parts of the force-displacement curves were investigated (Figure 4.32) for the lower displacement levels where the initial peak force is seen (approximately 3mm), it can be clearly seen that the amount of absorbed energy increases with the strain rate. Therefore, the calculated SAE value at 3 mm for dynamic test is greater than that of quasi-static test values (Figure 4.33). The initial peak force increases with the deformation rate.

Figure 4.34 shows the energy absorption characteristics of core structure with height of 20 mm and thickness of 1.5 mm in terms of SAE (at densification) and peak crushing force values at quasi-static and dynamic speeds. Distinct deformation behavior of the fingerprint core under dynamic loading is observed as compared to quasi-static crushing. Under static loading, the crushing occurred in the form of separation of the additive manufactured layers and the folding of these layers on each other. However, the

structure behaved in a brittle manner under dynamic loads. In other words, ductile-to-brittle transition occurred in failure at elevated strain rates due to the manufacturing principle of FDM. Similar features was observed by the other investigators (Rahim et al., 2017). Therefore, samples were axially split from bottom to top parallel to the direction of loading. Since the force-displacement relationship depends not only on the material properties of the structure itself, but also on the new contact surfaces formed upon the crushing of the structure, it is reported that a different deformation behavior (axial split) may prevent formation of new contact surfaces and may affect the crushing behavior adversely (Cetin and Baykasoğlu, 2019).

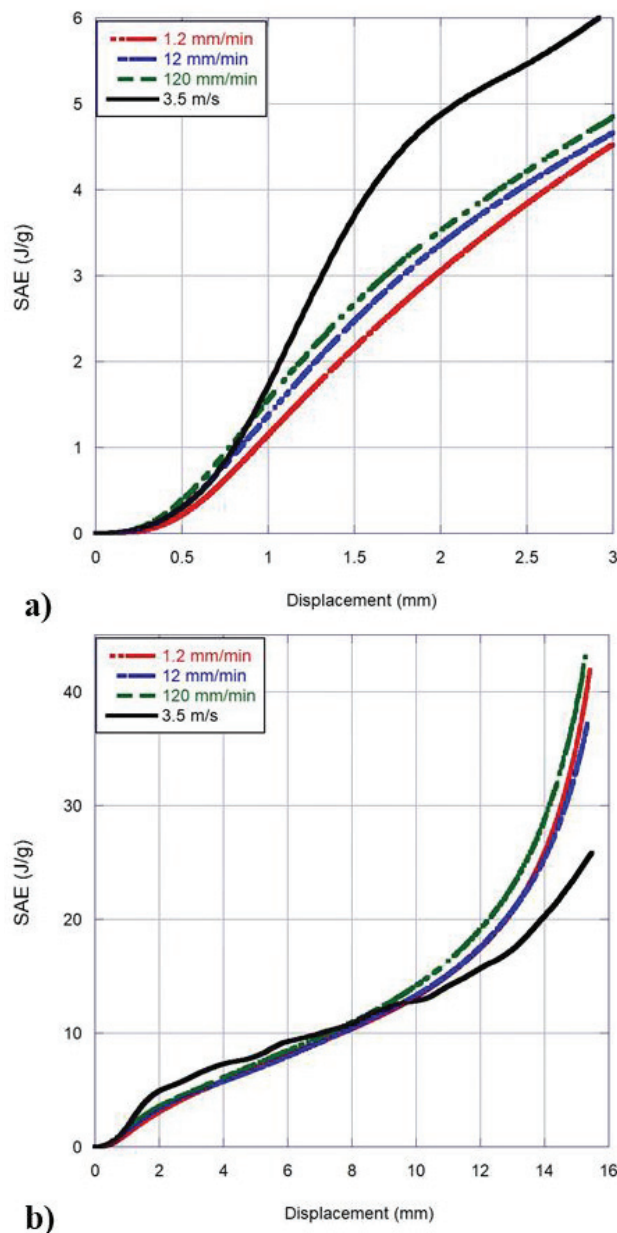


Figure 4.33. SAE vs. displacement curves of fingerprint at quasi-static and dynamic loads a) at 3mm, b) at densification region

As expected from the thermoplastic behavior, the peak force value was increased upon increasing the strain rate. For the SAE value, in contrast, this case was not valid at dynamic loads. As mentioned before, since the higher initial peak force value adversely affects the energy absorption performance, it is an undesirable feature in energy-absorbing structures.

Another reason for this weakening in energy absorption performance may be the rapid increase in structure's temperature due to highly effective plastic deformation. Therefore, the mechanical properties of 3-D printed structure made of a thermoplastic material can be affected adversely. The effect of thermal softening is seen as a weakening of the stiffness of molecular chains due to sudden heat increase (Hopmann et al., 2016). In summary, for 3.5 m/s dynamic test, the region between the initial peak force (at 2-3 mm) and plateau (~6mm) is expected to be affected by thermal softening as well as brittle failure due to tensile stress waves occurred under high strain rates.

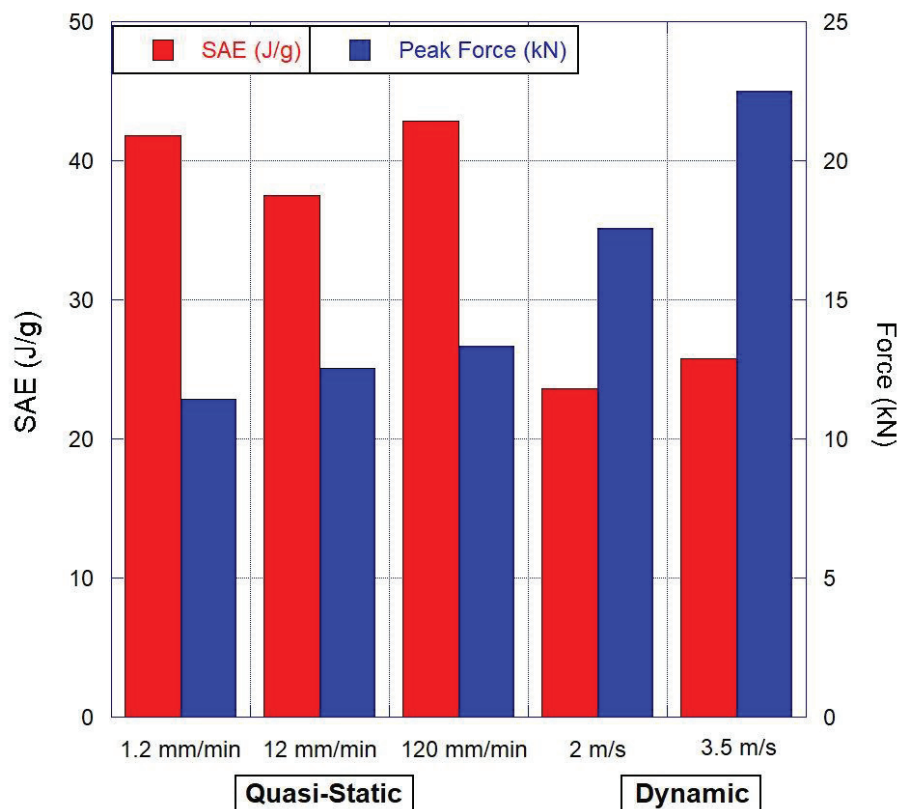


Figure 4.34. Quasi-static and dynamic experimental SAE & Peak force vs. displacement values of fingerprint core.

4.3. Fingerprint Core Numerical Model Validations

Under quasi-static loads, the force-displacement curves of the both experimental and numerical fingerprint core structure is plotted in Figure 4.35 for height of 20 mm and thickness of 1.5 mm. The deformation histories of the marked points in this curve are also shown in the figure. The experimental crushing test at 120 mm/min crosshead speed was modeled numerically by implicit solver. The images taken from numerical analysis corresponding to the same moment with the experiment are also shown in the Figure 4.36.

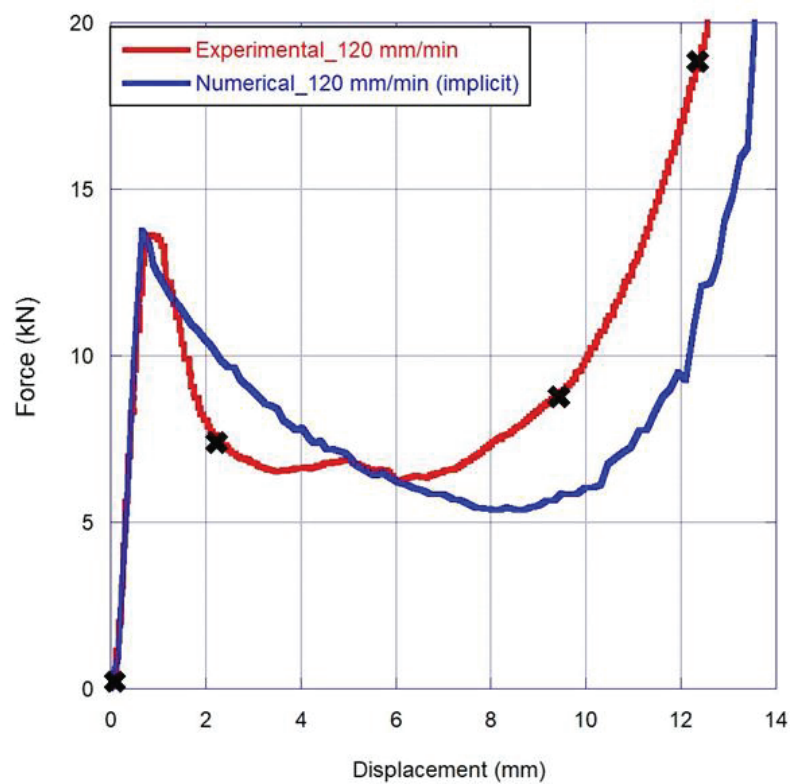


Figure 4.35. Comparison of force vs. displacement curves of experimental and numerical quasi-static compression of fingerprint core at 120 mm/min crosshead speed.

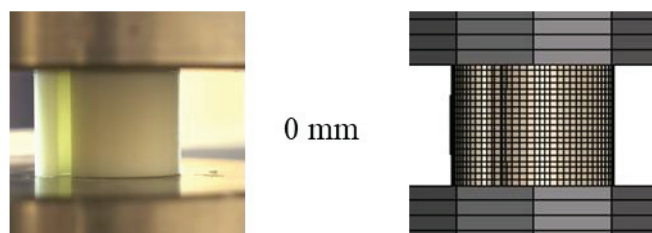


Figure 4.36. (cont.)

(cont. on next page)

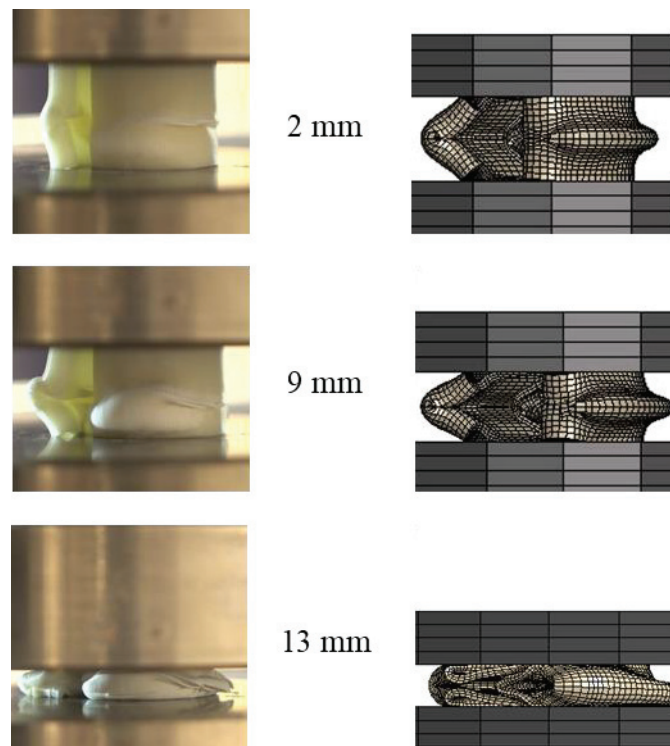


Figure 4.36. Comparison of the deformation histories of experimental and numerical quasi-static compression of fingerprint core.

In the experiment, the folds formed in the middle by the sliding (shearing) between the layers of the 3-D printed specimen. The crushing of the upper part onto the lower part could not be captured in numerical analysis. This is because the structure is not modeled as layered like composites and the fact that the anisotropy, due to the manufacturing technique, is not taken into account. In the experiment global bending, occurring around the bottom side of the structure during the experiment, was observed in the middle side of the numerical model. Crushing behavior on the left side of the structure is similar for both experiment and model. There are differences in force displacement curve due to minor differences in crushing behavior. Although the first peak force value is the same, the deformation behavior observed in numerical model is like the offset form of that of experiment. On the other hand, with the help of the solid model of the core structure, the peak force and densification regions are compatible with the experiment.

Under dynamic loads, the force-displacement curves of the both experimental and numerical fingerprint core structure are plotted in Figure 4.37, for height of 20 mm and thickness of 1.5 mm. The deformation histories of the marked points in this curve are also

shown in Figure 4.38. First, the fingerprint structure was crushed with the striker mass of 20 kg and the impact velocity of 2 m/s with 58 J total energy. In the drop-weight studies, there is a well-agreement in force-displacement curves as seen in Figure 4.37. The experimental peak force was measured as 17.5 kN, on the other hand, the numerical peak force was found as 18.5 kN. That is a 5.7% deviation was found between the peak force value obtained from the numerical analysis and the value measured from the experiment. This difference compensated in the later stage of crushing (from 3mm), and the amounts of energy absorbed were well similar.

As discussed earlier, the structure was not completely crushed and hence, densification was not observed. However, crack propagation and slippage of layers and separation of some of them was observed due to high deformation rate. The structure became more brittle when compared to static cases. Axial splitting (crack) initiated from the bottom side of the structure and propagated axially which is parallel to the loading direction. In both cases, the crushing started in the middle part of the structure. The splitting (crack) observed in the experiment was also observed in the simulation in a similar way.

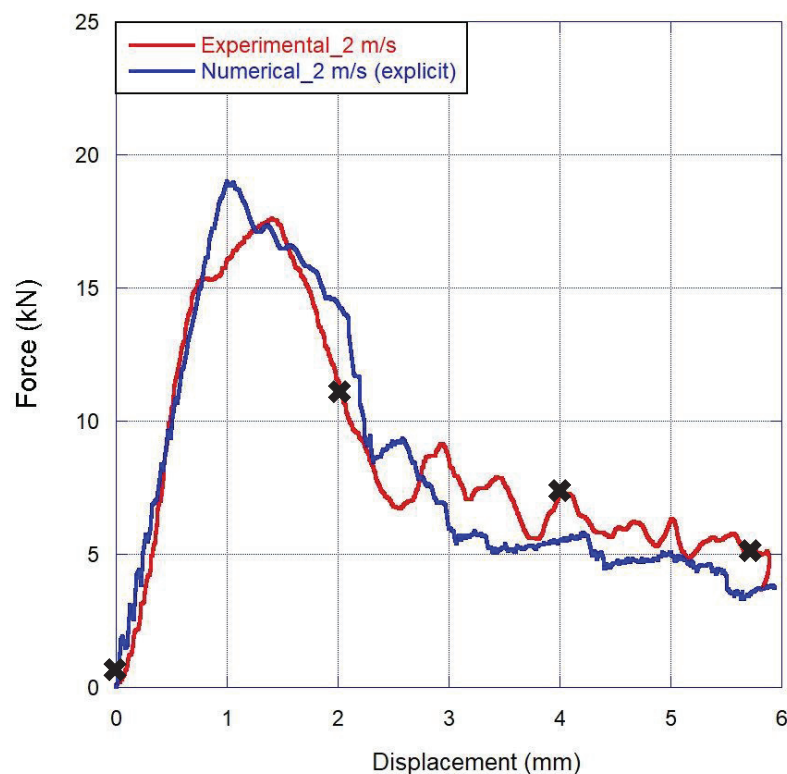


Figure 4.37. Comparison of force vs. displacement curves of experimental and numerical dynamic compression of fingerprint core at 2 m/s impact velocity.

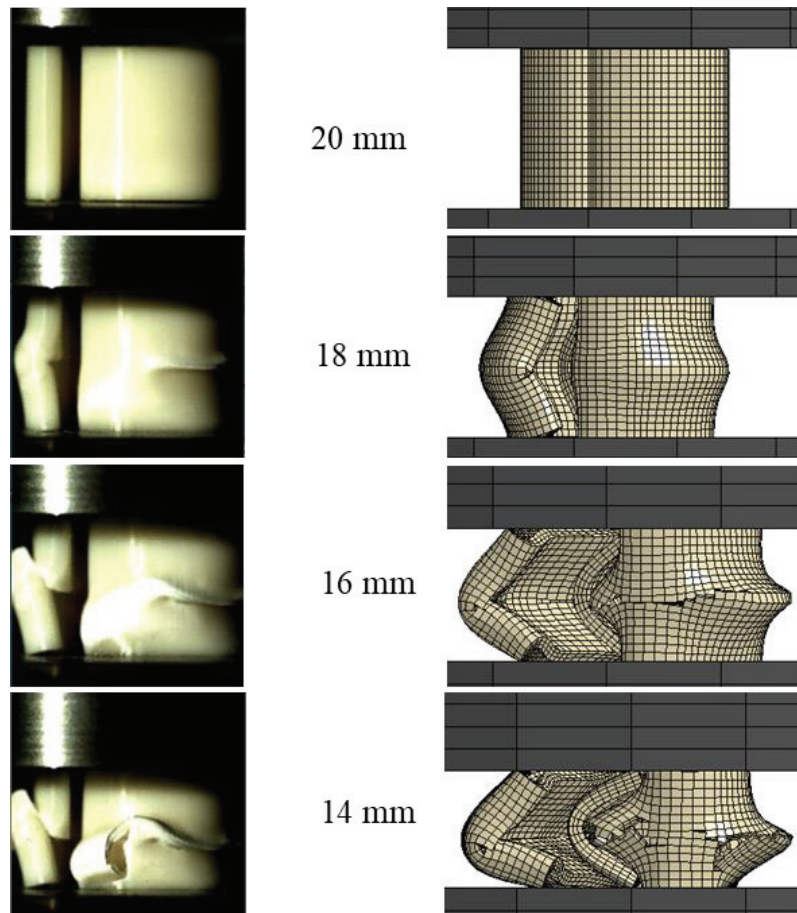
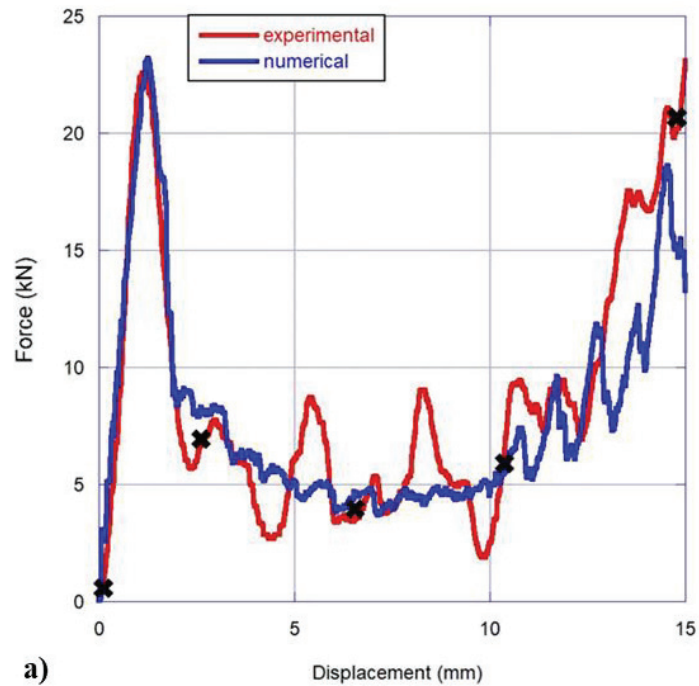


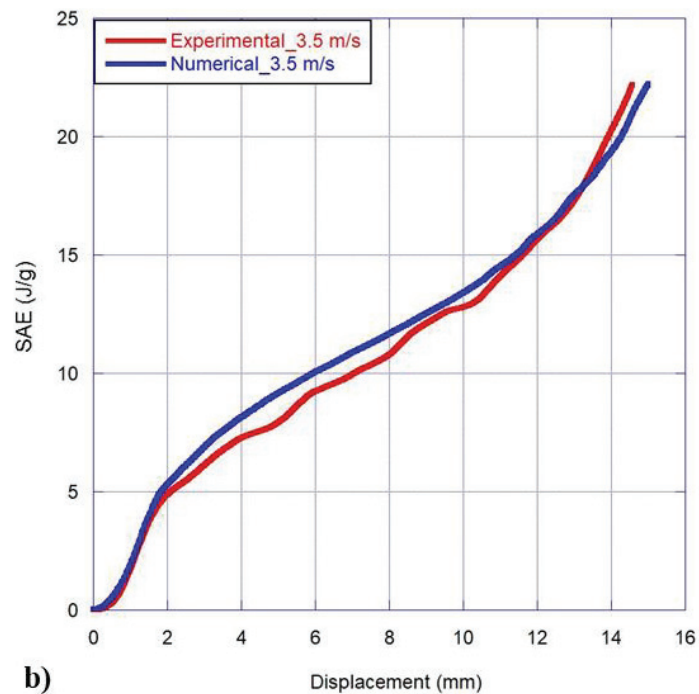
Figure 4.38. Comparison of the deformation histories of experimental and numerical dynamic compression of fingerprint core at 2 m/s impact velocity.

For dynamic loads having 3.5 m/s impact velocity, the force-displacement curves of the both experimental and numerical fingerprint core structure are plotted in Figure 4.39 (a), for height of 20 mm and thickness of 1.5 mm. The deformation histories of the marked points in this curve are also shown in Figure 4.40. First, the fingerprint structure was crushed with the striker mass of 20 kg and the impact velocity of 3.5 m/s with 180 J total energy. In the drop-weight studies, there is a well-agreement in force-displacement and SAE-displacement curves as seen in Figure 4.39 (a) and (b). The experimental peak force was measured as 22.58 kN, on the other hand, the numerical peak force was found as 23.5 kN. The deviation was found to be lower than 4% in terms of initial peak force. After 2.5 mm deformation, the force value obtained from the numerical study is close enough to the average of the force values measured from the experiment, which indicates that the FE results of the core structure are in a similar trend with the experimental results. When the drop-weight test and simulation for 3.5 m/s are compared, it is seen that the SAE values are the same at the densification region (~14mm) as shown in Figure 4.39

(b). Since the average value of local increases and decreases observed after the maximum peak value of the experiment was successfully captured with the average force value in the simulation, the energy absorption capacities exhibit similar behavior.



a)



b)

Figure 4.39. Comparison of a) force vs. displacement, b) SAE vs. displacement curves of experimental and numerical dynamic compression of fingerprint core at 3.5 m/s impact velocity.

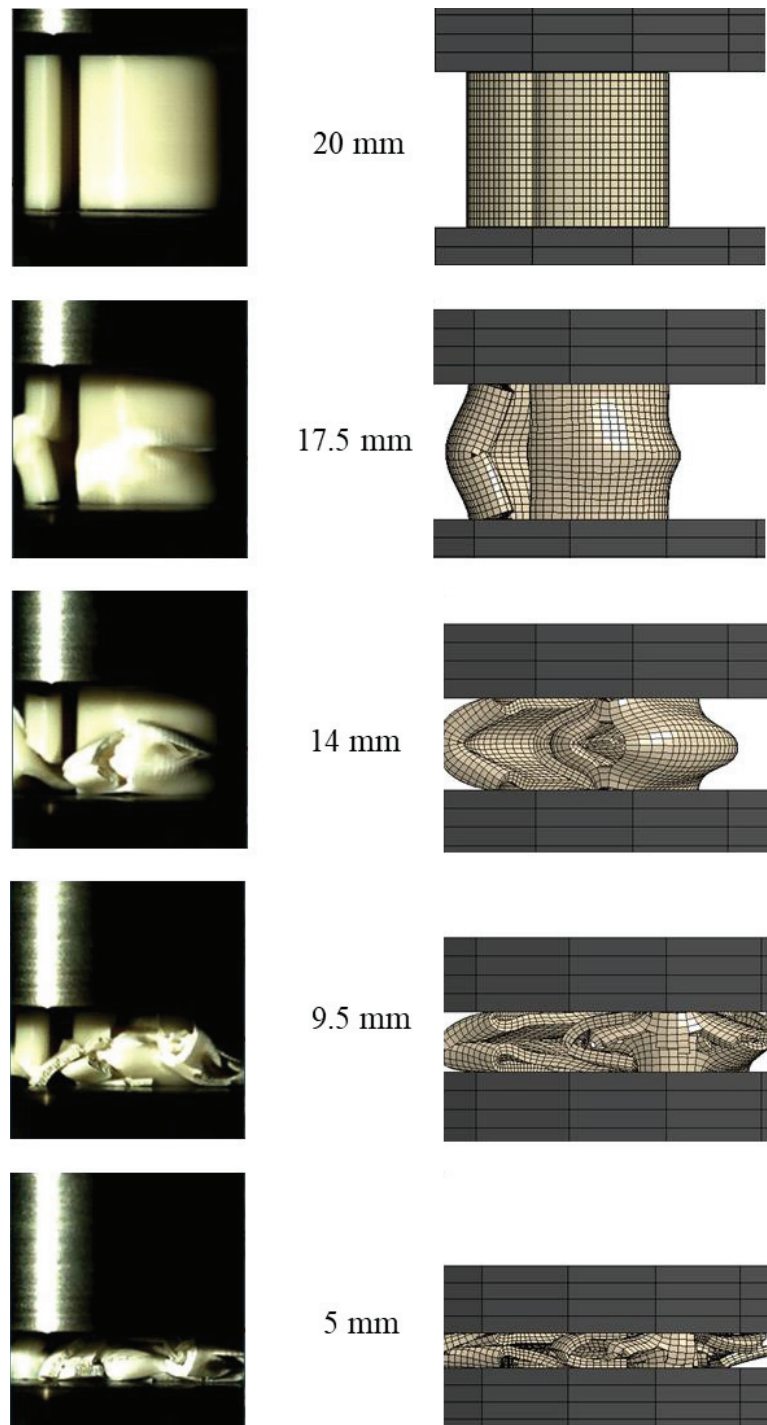


Figure 4.40. Comparison of the deformation histories of experimental and numerical dynamic compression of fingerprint core at 3.5 m/s impact velocity.

As it can be seen from the force-displacement graph (Figure 4.39 (a)), with the help of the solid model of the core structure, the peak force and densification regions are compatible with the experiment. However, when deformation histories examined (Figure 4.40), some differences were observed. In numerical analysis, much more outward

bending occurred compared to experiment. Nevertheless, splitting (crack) behavior was achieved with the given erosion parameters. The buckling location shifted up to middle of the structure instead of around the bottom of the structure.

As it was stated earlier, the reason of decrease in energy absorption capacity in dynamic tests may also be thermal softening. However, in the numerical study, a material model taking account the thermal softening behavior was not used because according to the numerical studies in the literature, thermal softening behavior is only effective in between the maximum force and plateau values. A force difference of 10% was found between the analysis with and without taking the thermal softening effect into account and no additional difference was observed in material behavior except this difference (Hopmann et al., 2016). As a result, the analysis was continued with a material model that did not take thermal softening into account for simplicity and minimizing computational cost. In summary, it was found that the developed finite element model gives a better understanding and estimation in terms of energy absorption performance of the 3D printed fingerprint structure.

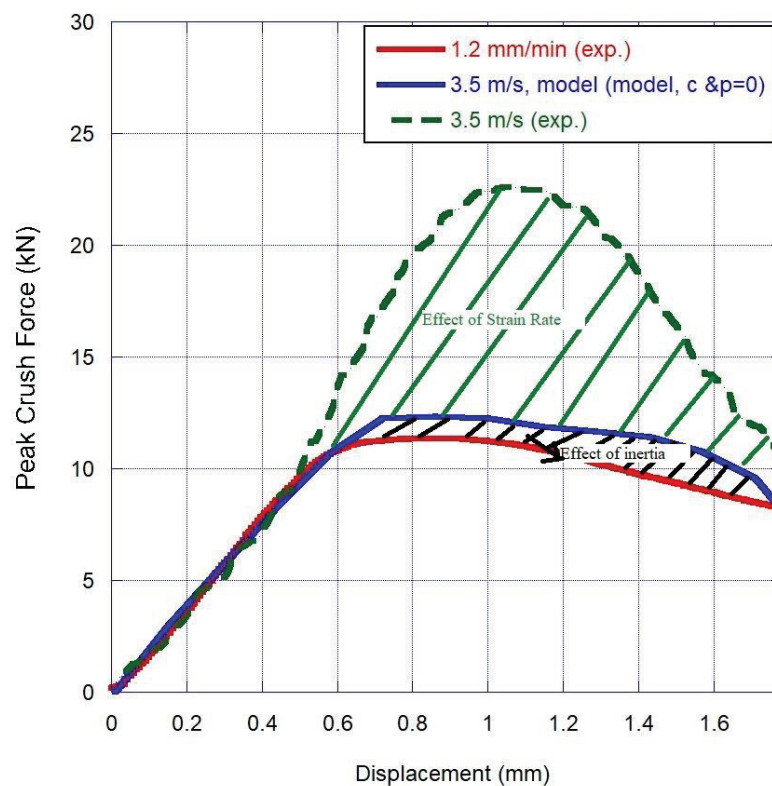


Figure 4.41. Investigation of inertia effect with rate sensitive experiment and rate insensitive numerical model.

In dynamic cases, not only strain rate has effect on mechanical behaviour of the structure but also inertia effects can directly be related with the energy absorption characteristics of the structures. Dynamic loads cause the structure to accelerate and they change the deformation mechanism by generating shear forces and/or bending moments. Therefore, they have an influence on energy absorption of the system (Lu and Yu, 2003). In order to investigate the inertia effect individually, the strain rate scaling factors were closed and the other parameters (boundary conditions, material constant) kept constant in numerical model. At higher strain rates, the specimen exhibits brittle fracture due to its manufacturing method (FDM) hence, its inertia effect cannot be observed properly. Instead of this, peak force portion of force-displacement curve was investigated. The initial part of the force-displacement curves of quasi-static, drop-weight and strain rate insensitive model (between 0-2 mm) were compared as shown in Figure 4.41. As it can be seen in the figure, the peak force value was found to be more rate sensitive rather than inertia.

4.4. Sandwich Structure Crushing Behavior Results

A sandwich structure that consist of aluminum face sheets having 2 mm thickness and 4 fingerprints, was modeled and drop-weight simulations were performed for two different impact velocities (2 and 3.5 m/s).

As can be seen in the force displacement graph (Figure 4.42) for 2m/s, the peak force value increased from 68 kN to 88.3 kN, although the impact velocity was the same. Confinement effect was observed because fingerprint structures came into contact with each other during crushing and core structures started to break at a later value. Therefore, since the average force value increased, the sandwich structure absorbed 18% more energy than 4 single structures could absorbed as shown in Figure 4.42 (b).

Then, a sandwich structure numerically crushed at 3.5 m/s impact velocity. As can be seen in the force displacement graph (Figure 4.43), the peak force values were measured as 90 kN and 93 kN for the experimental drop-weight test with multiplied by 4 and numerical sandwich structure, respectively. When the force-displacement curve of sandwich structure crushed at 3.5 m/s is investigated, it is seen that the force value after the first (maximum) peak does not decrease as much as the individual curve which is

multiplied by 4. Sandwich structure prevents the early failure of each individual fingerprints, since they support each other by wall to wall contact. This feature enables it to absorb more energy than the individual crushing scenario. As it can be seen from Figure 4.43 (b), the sandwich structure absorbs 13% more impact energy from the first peak to densification region.

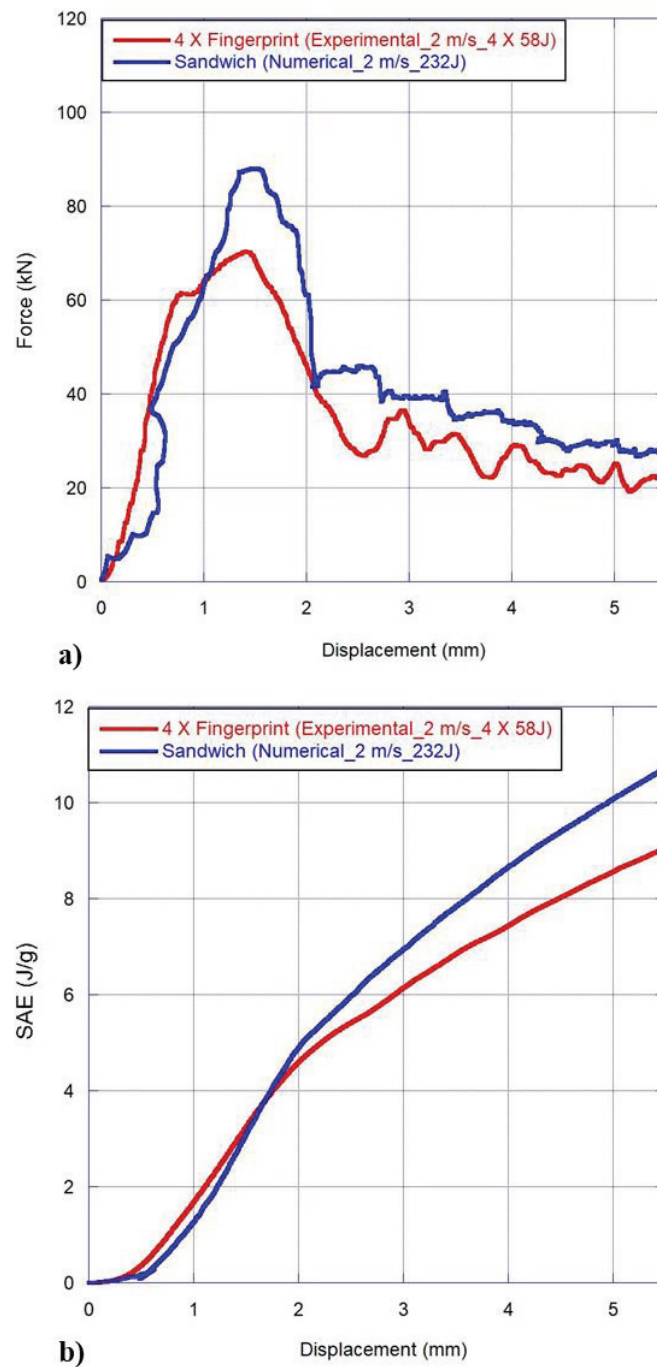


Figure 4.42. Comparison of a) force vs. displacement, b) SAE vs. displacement curves of numerical bio-inspired sandwich structure and experiment for individual core multiplied by 4 at 2 m/s impact velocity.

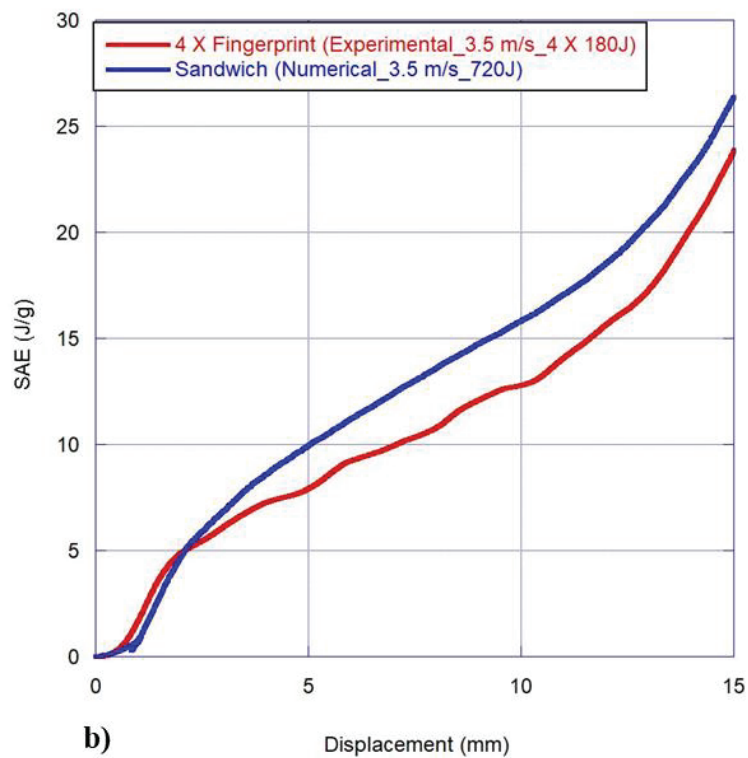
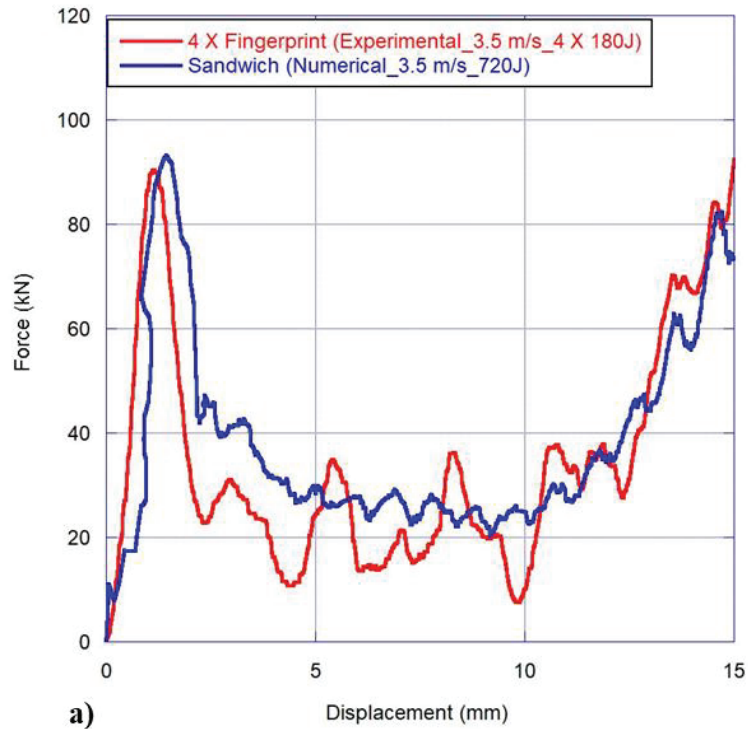


Figure 4.43. Comparison of a) force vs. displacement, b) SAE vs. displacement curves of numerical bio-inspired sandwich structure and experiment for individual core multiplied by 4 at 3.5 m/s impact velocity.

The deformation history of bio-inspired sandwich structure is shown in Figure 4.44. As it can be seen clearly, the deformation behavior of the sandwich structure was

similar to fingerprint core which was crushed individually. The structures began to break in the middle as in the single crush test. When deformation histories, force displacement and SAE values are compared, it is seen that the developed numerical model is successful in examining the behavior of structures produced by additive production method. This model can be applied for simulation of different test devices at different loading conditions.

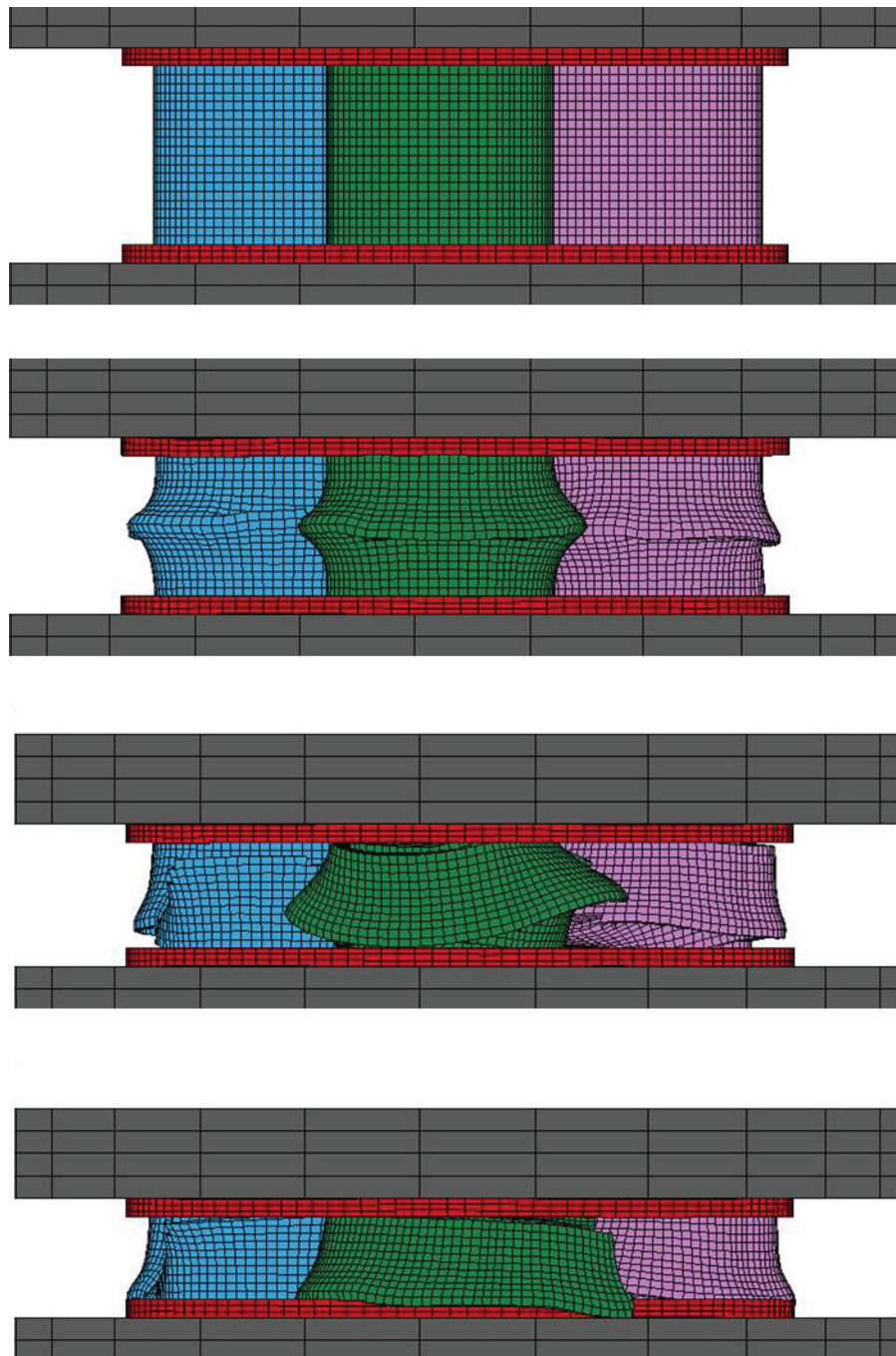


Figure 4.44. Deformation history of sandwich structure consisting of aluminum faces and 4 fingerprint core.

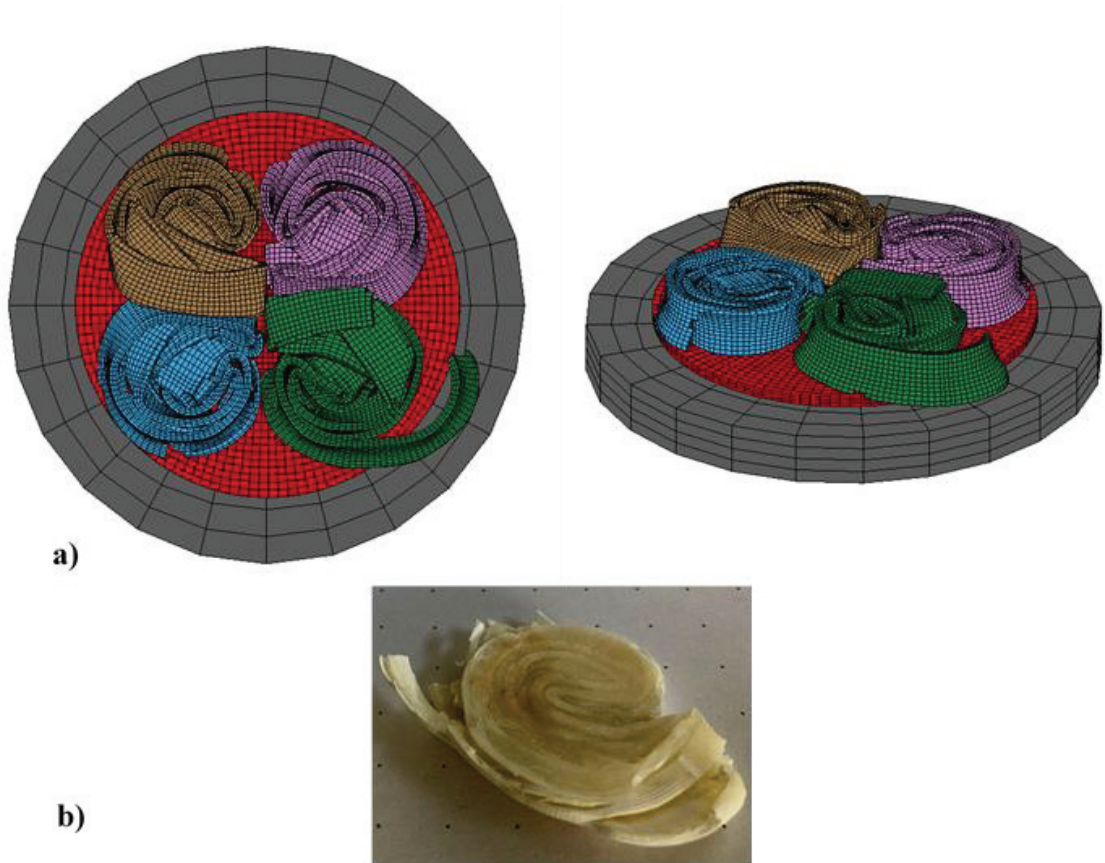


Figure 4.45. a) The deformed view of numerically crushed sandwich structure consisting of 4 fingerprint b) The deformed view of experimentally crushed fingerprint core.

CHAPTER 5

CONCLUSION

The main objective of this study was to develop a core geometry providing higher mechanical properties and higher energy absorption capability against the impacts. The energy absorbers must have maximum impact energy absorption capacity with minimum density. For this purpose, bio-inspired geometric pattern was used to obtain the further improvement in energy absorption capability at relatively low weights.

For the material used and test methods applied the following conclusions can be made:

Due to the complex structure of the designed core geometry, namely fingerprint, Fused Deposition Modeling (FDM) which is one of the additive manufacturing methods known as 3D printing was selected, since it enabled to produce complex geometries and shapes with the help of its manufacturing technique that is based on layer by layer production.

Since the dynamic characterization is extremely important for polymeric materials due to their known strain rate sensitivity and there are no established test standards for 3D printed objects, suitable testing samples and methodologies were developed to characterize the 3D printed ABS samples. The mechanical characterization tests were performed under both static and dynamic loads and stress-strain relations and strain rate effects on yield stress were determined. Since the characterization specimens were manufactured by FDM, the obtained material curves and constants take the anisotropy into account due to production technique.

In the quasi-static tensile test characterizations, it was observed that the material failed before the expected strain values. The reason is that the weak bonding existing between the layers of the structure produced with an FDM technique is a major reason to failure due to solidification of viscous hot layer onto the respectively cold solid layer. Therefore, strength of the structure is less than the bulk material because of reduced integrity of the structure.

It was concluded that by changing the operation parameters of 3-D printer in terms of raster angle, feed rate, temperature difference between the platform and nozzle and infill density, the gaps between the layers can be minimized thereby the mechanical performance (yield strength and failure strain) of additive manufactured structure can be enhanced.

Although process parameters in FDM technique have a direct effect on the mechanical performance of the structure, in this study, rather than the production parameters, only the fingerprint itself as a core geometry and its geometrical effects on the energy absorption capacity was investigated.

When the dynamic compression tests were examined, it was observed that the chosen manufacturing method (FDM) had a positive effect on the energy absorption behavior of the material between low-to-medium strain rates. Since the 3-D printer first creates the outer frame of the structure and then fills it with +45/-45 raster angle, the outer frame (line) adds a partial confinement effect to the structure and hence the mesh like filling shows better crushing behavior.

In numerical analysis, it was observed that the effect of 3-D printing on mechanical properties and strain rate sensitive behavior of thermoplastic material were well close to that of experiments with the help of developed material model that uses static and dynamic characterization curves as an input

The effect of design parameters (thickness and height) of fingerprint core structure on crashworthiness characteristics was examined. The final optimized design was selected as having 20mm height and 1.5mm thickness in the light of the experimental and numerical analysis.

Comparison of the novel core geometry with other conventional geometries (cylinder, square and honeycomb) in terms of specific energy absorption capacity was performed and concluded that the fingerprint absorbs 43% more energy than its closest competitor, namely cylinder when compared for same real density.

The energy absorption characteristics of the core structure were examined both experimentally and numerically under the static and dynamic loads. The energy absorbing behaviors and deformation histories were compared to realize the model accuracy.

In the light of the experiments, it was found that the load carrying capacity of the fingerprint core is increased as the strain rate increases at quasi-static strain rates. In

dynamic cases, on the other, the SAE value at densification points decreased due to brittle failure. However, the peak crushing force value doubled to 22.58 kN when strain rate increased.

It was found that the structure exhibited brittle behavior under dynamic loads which was due to the additive manufacturing method and the behavior of the thermoplastic material. At the same time, under dynamic loads, the ABS material experienced a sudden increase in temperature. It affected the mechanical properties adversely. Therefore, the crashworthiness performance was affected adversely as well.

The inertia effect could not be investigated exactly since the structure behaved more brittle under dynamic loads. For this reason, peak force values were compared, and it was observed that the behavior of the structure in the peak force portion of force-displacement curve was more strain rate sensitive than inertia. When the crushing characteristics of structure were investigated, it was observed that having dramatic decrease after high peak force is more sensitive to strain rate. A more ductile material should be used to observe the effect of inertia from the local contacts of the geometry that are crushed.

It was observed that the bio-inspired sandwich structure consisting of 4 fingerprint core could absorb 10% more impact energy than fourfold individual 3-D printed core geometry. It indicates the promising potential of the novel sandwich structure for crashworthiness applications.

Future work recommendations:

The effect of process parameters on the mechanical performance of the structures produced by AM method can be investigated and it is possible to determine which parameters will be changed instead of using default settings in order to have superior mechanical properties.

REFERENCES

- Aftab, S. M. A, N. A. Razak, A. S. Mohd Rafie, and K A Ahmad. 2016. "Mimicking the Humpback Whale: An Aerodynamic Perspective." *Progress in Aerospace Sciences* 84 (2016): 48–69.
- Aizenberg, Joanna, James C. Weaver, Monica S. Thanawala, Vikram C. Sundar, Daniel E. Morse, and Peter Fratzl. "Skeleton of Euplectella Sp.: Structural Hierarchy from the Nanoscale to the Macroscale." *Science* 309, no. 5732 (August 2005): 275–78.
- Ali, M., A. Qamhiyah, D. Flugrad, and M. Shakoor. "Compact Energy Absorbing Structure:A Finite Element Study." *Proceedings of the IEEE 32nd Annual Northeast Bioengineering Conference*, 2006, 9–10.
- Appelsved, Peter. "Investigation of Mechanical Properties of Thermoplastics with Implementations of LS-DYNA Material Models," 2012.
- Autumn, Kellar, Yiching A. Liang, S. Tonia Hsieh, Wolfgang Zesch, Wai Pang Chan, Thomas W. Kenny, Ronald Fearing, and Robert J. Full. "Adhesive Force of a Single Gecko Foot-Hair." *Nature* 405, no. 6787 (2000): 681–85.
- Autumn, K., M. Sitti, Y. A. Liang, A. M. Peattie, W. R. Hansen, S. Sponberg, T. W. Kenny, R. Fearing, J. N. Israelachvili, and R. J. Full. "Evidence for Van Der Waals Adhesion in Gecko Setae." *Proceedings of the National Academy of Sciences* 99, no. 19 (2002): 12252–56.
- Aziz, Moheb Sabry, and Amr Y. El Sherif. "Biomimicry as an Approach for Bio-Inspired Structure with the Aid of Computation." *Alexandria Engineering Journal* 55, no. 1 (2015): 707–14.
- Baroutaji, Ahmad, Mustafa Sajjia, and Abdul-Ghani Olabi. "On the Crashworthiness Performance of Thin-Walled Energy Absorbers: Recent Advances and Future Developments." *Thin-Walled Structures* 118 (May 2017): 137–63.
- Benyus, Janine M. "Innovation Inspired by Nature," 1997.

- Bitzer, Tom. *Honeycomb Technology: Materials, Design, Manufacturing, Applications And Testing*. (London: Chapman & Hall: Springer, 1997)
- Bodaghi, M., A. Serjouei, A. Zolfagharian, M. Fotouhi, H. Rahman, and D. Durand. “Reversible Energy Absorbing Meta-Sandwiches by FDM 4D Printing.” *International Journal of Mechanical Sciences* 173 (September 2019): 105451.
- Chacón, J. M., M. A. Caminero, E. García-Plaza, and P. J. Núñez. “Additive Manufacturing of PLA Structures Using Fused Deposition Modelling: Effect of Process Parameters on Mechanical Properties and Their Optimal Selection.” *Materials & Design* 124 (2017): 143–57.
- Cetin, Erhan, and Cengiz Baykasoğlu. “Energy Absorption of Thin-Walled Tubes Enhanced by Lattice Structures.” *International Journal of Mechanical Sciences* 157-158 (December 2019): 471–84.
- Champod, Christophe, Chris Lennard, Pierre Margot, and Milutin Stoilovic. “Fingerprint Detection Techniques.” *Fingerprints and Other Ridge Skin Impressions International Forensic Science and Investigation*, 2004.
- Davis, Andrew, 8 Most Common Fingerprint Patterns, 2017, <https://www.touchngoid.com/8-common-fingerprint-patterns/>
- Dikshit, Vishwesh, Arun Nagalingam, Yee Yap, Swee Sing, Wai Yeong, and Jun Wei. “Investigation of Quasi-Static Indentation Response of Inkjet Printed Sandwich Structures under Various Indenter Geometries.” *Materials* 10, no. 3 (2017): 290.
- Fasanella, Edwin L., and Karen E. Jackson. “Best Practices for Crash Modeling and Simulation,” October 2002, 4–14.
- Fayemi, Pierre Emmanuel, N. Maranzana, A. Aoussat, and G. Bersano. “Bio-Inspired Design Characterisation and Its Links with Problem Solving Tools.” *International Design Conference-Design 2014*, May 2014.
- Fish, Franke E., and Juliann M. Battle. “Hydrodynamic Design of the Humpback Whale

- Flipper.” *Journal of Morphology* 225, no. 1 (1995): 51–60.
- Gautam, Rinoj, Sridhar Idapalapati, and Stefanie Feih. “Printing and Characterisation of Kagome Lattice Structures by Fused Deposition Modelling.” *Materials & Design* 137 (2018): 266–75.
- Geim, A. K., S. V. Dubonos, I. V. Grigorieva, K. S. Novoselov, A. A. Zhukov, and S. Yu. Shapoval. “Microfabricated Adhesive Mimicking Gecko Foot-Hair.” *Nature Materials* 2, no. 7 (January 2003): 461–63. <https://doi.org/10.1038/nmat917>.
- Goh, G.d., V. Dikshit, A.p. Nagalingam, G.l. Goh, S. Agarwala, S.l. Sing, J. Wei, and W.y. Yeong. “Characterization of Mechanical Properties and Fracture Mode of Additively Manufactured Carbon Fiber and Glass Fiber Reinforced Thermoplastics.” *Materials & Design* 137 (2018): 79–89.
- Haldar, A.K., J. Zhou, and Z. Guan. “Energy Absorbing Characteristics of the Composite Contoured-Core Sandwich Panels.” *Materials Today Communications* 8 (2016): 156–64.
- Haldar, Sandip, and Hugh A. Bruck. “Mechanics of Composite Sandwich Structures with Bioinspired Core.” *Composites Science and Technology* 95 (2014): 67–74.
- Heimbs, Sebastian. “Energy Absorption in Aircraft Structures.” In *International Workshop on Hydraulic Equipment and Support Systems for Mining*, 2012, 1–10.
- Hoover, J. Edgar, “Fingerprint” Encyclopædia Britannica, 2016.
- Hopmann, Christian, Jan Klein, and Maximilian Schöngart. “Determination of the Strain Rate Dependent Thermal Softening Behavior of Thermoplastic Materials for Crash Simulations.” *AIP Conference Proceedings* 1713 (2016): 1–5.
- Hyun, S., A.m. Karlsson, S. Torquato, and A.g. Evans. “Simulated Properties of Kagomé and Tetragonal Truss Core Panels.” *International Journal of Solids and Structures* 40, no. 25 (2003): 6989–98.
- Johnson, W., and A.G Mamalis. *Crashworthiness of Vehicles*. (1978).

- Johnson, W., and S. R. Reid. "Metallic Energy Dissipating Systems." *Applied Mechanics Reviews* 31 (1977): 277–88.
- Johnson, W. "The Elements of Crashworthiness : Scope and Actuality." *Proceedings of the Institution of Mechanical Engineers, Part D: Journal of Automobile Engineering* 204, no.4 (1990): 255–73.
- Kanu, Rex, Caleb Hale, and Patrick Piper. "The Use of 3D Printing to Introduce Students to ASTM Standards for Testing Tensile Properties of Acrylonitrile-Butadiene-Styrene (ABS) Plastic Material." *2016 ASEE Annual Conference & Exposition Proceedings*, 2016.
- Kerekcs, Tomas Webbe, Hyoungjun Lim, Woong Yeol Joe, and Gun Jin Yun. "Characterization of Process–Deformation/Damage Property Relationship of Fused Deposition Modeling (FDM) 3D-Printed Specimens." *Additive Manufacturing* 25 (2019): 532–44.
- Lee, Byung-Kon, and Ki-Ju Kang. "A Parametric Study on Compressive Characteristics of Wire-Woven Bulk Kagome Truss Cores." *Composite Structures* 92, no. 2 (2010): 445–53.
- Li, Yuqin, Chaoying Xu, Chang Shu, Xiandeng Hou, and Peng Wu. "Simultaneous Extraction of Level 2 and Level 3 Characteristics from Latent Fingerprints Imaged with Quantum Dots for Improved Fingerprint Analysis." *Chinese Chemical Letters* 28, no. 10 (2017): 1961–64.
- LSTC, Livermore Software Technology Corporation. *Ls-Dyna Theory Manual*. (2016).
- Lobo, Hubert. "FE Update: Simulating Plastics in Drop and Crash Tests." 2008. <https://www.machinedesign.com/news/article/21817852/fe-update-simulating-plastics-in-drop-and-crash-tests>.
- LSTC, Livermore Software Technology Corporation. *LS-DYNA Keyword User's Manual Volume II Material Models*. Vol. II. (2016).
- Lu, Guoxing, and Tongxi Yu. "Energy Absorption of Structures and Materials," 2003.

- Maso, Alberto Dal, and Francesca Cosmi. "Mechanical Characterization of 3D-Printed Objects." *Materials Today: Proceedings* 5, no. 13 (2018): 26739–46.
- ASTM. "Test Method for Tensile Properties of Plastics." *ASTM D-638-2a*, 2003.
- Menig, R., M.H. Meyers, M. A. Meyers, and K. S. Vecchio. "Quasi-Static and Dynamic Mechanical Response of *Haliotis Rufescens* (Abalone) Shells." *Acta Materialia* 48, no. 9 (2000): 2383–98.
- Meyers, M A., Po-yu Chen, Albert Yu-min Lin, and Yasuaki Seki. "Biological Materials : Structure and Mechanical Properties." *Materials Science* 53 (2008): 1–206.
- Mulliken, A.D., and M.C. Boyce. "Mechanics of the Rate-Dependent Elastic–Plastic Deformation of Glassy Polymers from Low to High Strain Rates." *International Journal of Solids and Structures* 43, no. 5 (2006): 1331–56.
- Nia, A. Alavi, and S. Chahardoli. "Mechanical Behavior of Nested Multi-Tubular Structures under Quasi-Static Axial Load." *Thin-Walled Structures* 106 (2016): 376–89.
- Owolabi, Gbadebo, Alex Peterson, Ed Habtour, Jaret Riddick, Michael Coatney, Adewale Olasumboye, and Denzell Bolling. "Dynamic Response of Acrylonitrile Butadiene Styrene under Impact Loading." *International Journal of Mechanical and Materials Engineering* 11, no. 1 (2016).
- Parker, Andrew R., and Chris R. Lawrence. "Water Capture by a Desert Beetle." *Nature* 414, no. 6859 (2001): 33–34.
- Rahim, T. N. A. T., A. M. Abdullah, H. Akil, D. Mohamad, and Z. A. Rajion. "The Improvement of Mechanical and Thermal Properties of Polyamide 12 3D Printed Parts by Fused Deposition Modelling." *Express Polymer Letters* 11, no. 12 (2017): 963–82.
- Ryan, John C. Dizon, Alejandro H. Espera, Qiyi Chen, and Rigoberto C. Advincula. "Mechanical Characterization of 3D-Printed Polymers." *Additive Manufacturing* 20 (2018): 44–67.

- Sabah, S. H. Abo, A.B.H. Kueh, and M.Y. Al-Fasih. “Comparative Low-Velocity Impact Behavior of Bio-Inspired and Conventional Sandwich Composite Beams.” *Composites Science and Technology* 149 (2017): 64–74.
- Sarikaya, M., K. E. Gunnison, M. Yasrebi, and I. A. Aksay. “Mechanical Property-Microstructural Relationships in Abalone Shell.” *MRS Proceedings* 174 (1989).
- Seki, Yasuaki, Sara G. Bodde, and Marc A. Meyers. “Toucan and Hornbill Beaks: A Comparative Study.” *Acta Biomaterialia* 6, no. 2 (2010): 331–43.
- Seki, Yasuaki, Bimal Kad, D. Benson, and Marc A. Meyers. “The Toucan Beak: Structure and Mechanical Response.” *Materials Science and Engineering: C* 26, no. 8 (2006): 1412–20.
- Seki, Yasuaki, M. Schneider, and M. Meyers. “Structure and Mechanical Behavior of a Toucan Beak.” *Acta Materialia* 53, no. 20 (2005): 5281–96.
- Sitti, Metin, and Ronald S. Fearing. “Synthetic Gecko Foot-Hair Micro/Nano-Structures as Dry Adhesives.” *Journal of Adhesion Science and Technology* 17, no. 8 (2003): 1055–73.
- Siviour, Clive R., S. M. Walley, W. G. Proud, and J. E. Field. “Mechanical Behaviour of Polymers at High Rates of Strain.” *Journal of Physique IV* 134 (2006): 949–955.
- Smardzewski, Jerzy. “Wooden Sandwich Panels with Prismatic Core – Energy Absorbing Capabilities.” *Composite Structures* 230 (2019): 111535.
- Smith, Alice E., and S Jeffrey, “Introduction to Additive Manufacturing,” NASA Academy of Aerospace Quality, 2016, <https://aaq.auburn.edu/node/9907/>.
- Su, X Y, and R. Reid. “Inertia-Sensitive Impact Energy-Absorbing Structures Part 1: Effects of Inertia and Elasticity.” *International Journal of Impact Engineering* 16, no. 4 (1995): 651–72.
- Tasdemirci, Alper, Emine Fulya Akbulut, Erkan Guzel, Firat Tuzgel, Atacan Yucesoy, Selim Sahin, and Mustafa Guden. “Crushing Behavior and Energy Absorption Performance of a Bio-Inspired Metallic Structure: Experimental and Numerical

- Study.” *Thin-Walled Structures* 131 (2018): 547–55.
- Tyler, Hamilton, “Whale Inspired Wind Turbines,” MIT Technology Review, 2008, <https://www.technologyreview.com/s/409710/whale-inspired-wind-turbines/>.
- Ullah, I., J. Elambasseril, M. Brandt, and S. Feih. “Performance of Bio-Inspired Kagome Truss Core Structures under Compression and Shear Loading.” *Composite Structures* 118 (2014): 294–302.
- Usta, Fatih, and Halit S. Türkmen. “Experimental and Numerical Investigation of Impact Behavior of Nested Tubes with and without Honeycomb Filler.” *Thin-Walled Structures* 143 (2019): 106256.
- Vincent, Michel, T. Giroud, A. Clarke, and C. Eberhardt. “Description and Modeling of Fiber Orientation in Injection Molding of Fiber Reinforced Thermoplastics.” *Polymer* 46, no. 17 (2005): 6719–25.
- Wadley, H, Norman Fleck, and Anthony G. Evans. “Fabrication and Structural Performance of Periodic Cellular Metal Sandwich Structures.” *Composites Science and Technology* 63, no. 16 (2003): 2331–43.
- Watts, P. ve Fish, F.E. “The influence of passive, leading edge tubercles on wing performance”. *Proc. Twelfth Intl. Symp. Unmanned Untethered Submers. Technol., (2001)*, 2–9.
- Wegst, U G K, and M F Ashby. “The Mechanical Efficiency of Natural Materials.” *Philosophical Magazine* 84, no.21 (2004): 2167–86.
- Wu, Yinghan, Qiang Liu, Jie Fu, Qing Li, and David Hui. “Dynamic Crash Responses of Bio-Inspired Aluminum Honeycomb Sandwich Structures with CFRP Panels.” *Composites Part B: Engineering* 121 (2017): 122–33.
- Wu, Yuan-Qi, Ce Guo, Long-Hai Li, and Zhen-Dong Dai. “Design of Bio-Inspired Lightweight Sandwich Structure and Its Mechanical Performance.” *Mechanics and Materials Science*, September 2017.

- Xu, Linru, Congzhe Zhang, Yayun He, and Bin Su. “Advances in the Development and Component Recognition of Latent Fingerprints.” *Science China Chemistry* 58, no. 7 (March 2015): 1090–96.
- Yang, Wen, Neima Kashani, Xiao-Wu Li, Guang-Ping Zhang, and Marc André Meyers. “Structural Characterization and Mechanical Behavior of a Bivalve Shell (Saxidomus Purpuratus).” *Materials Science and Engineering: C* 31, no. 4 (2011): 724–29.
- Yang, Xianfeng, Jingxuan Ma, Yingli Shi, Yuxin Sun, and Jialing Yang. “Crashworthiness Investigation of the Bio-Inspired Bi-Directionally Corrugated Core Sandwich Panel under Quasi-Static Crushing Load.” *Materials & Design* 135 (2017): 275–90.
- Yoo, S.H., S.H. Chang, and M.P.F. Sutcliffe. “Compressive Characteristics of Foam-Filled Composite Egg-Box Sandwich Panels as Energy Absorbing Structures.” *Composites Part A: Applied Science and Manufacturing* 41, no. 3 (2010): 427–34.
- Young, Kevin. “Development of a Tensile Split Hopkinson Pressure Bar Testing Facility.” (2015).
- Yu, Z.I., P. Xue, and Z. Chen. “Reprint of: Nested Tube System Applicable to Protective Structures against Blast Shock.” *International Journal of Impact Engineering* 105 (2017): 13–23.
- Zhang, Qiang, Yingfei Lin, Haitao Chi, Jing Chang, and Gaohui Wu. “Quasi-Static and Dynamic Compression Behavior of Glass Cenospheres/5A03 Syntactic Foam and Its Sandwich Structure.” *Composite Structures* 183 (2018): 499–509.